

Modelling of long-term trends in the middle and upper atmosphere

Thesis submitted for the degree of
Doctor of Philosophy
at the University of Leicester

Ingrid Crossen
Department of Physics and Astronomy
University of Leicester

December 2008

Abstract

Modelling of long-term trends in the middle and upper atmosphere

Ingrid Cnossen

From the 1950s/1960s to the present, long-term trends in temperature, density and winds in the middle and upper atmosphere, and in the height of the peak of the ionospheric F2 layer (hmF2) and its critical frequency (foF2) have been observed. These trends are usually attributed to increases in CO₂ concentration that have occurred over the same time span, which cause a cooling and contraction of the middle and upper atmosphere.

However, modelling studies generally predict smaller trends in temperature, larger trends in density, and more globally uniform trends in hmF2 and foF2 due to changes in CO₂ concentration than have been observed. When additional changes in ozone concentration are accounted for, modelling results are in better agreement with observations, but so far this had only been studied up to ~150-200 km.

Here we used the Coupled Middle Atmosphere and Thermosphere model version 2 to study the combined effects of changes in CO₂ and ozone concentration on the middle and upper atmosphere, including the ionosphere, from ~15-300 km. It was confirmed that changes in ozone concentration affect trends in temperature and density substantially until 200 km, and also effects above 200 km and on hmF2 were found. The results depended on the gravity wave parameterization used by the model, showing that dynamical factors can influence long-term trends. The Thermosphere-Ionosphere-Electrodynamics General Circulation Model was used to model the effects of changes in the Earth's magnetic field on hmF2 and foF2. Substantial trends were found over South America and the Atlantic Ocean, while other parts of the world were little affected. Sensitivity analyses showed that the responses obtained with both models depend on geophysical conditions such as season and solar and geomagnetic activity.

In general it can be concluded that long-term trends are probably caused by multiple coupled radiative and dynamical processes.

Acknowledgments

I am grateful for financial support for my PhD through the SPARTAN programme (Centre of Excellence for Space, Planetary and Astrophysics Research Training and Networking, European Commission, Marie Curie Actions, contract number MEST-CT-2004-007512), and for the opportunity this gave me to spend two periods of three months abroad.

Scientific support of my work was provided by many people. First of all, I must thank my supervisor, Neil Arnold, for his time and enthusiasm, and for sharing his ideas with me, while letting me free at the same time to explore ideas of my own. Second, a big thank you must go to Matt Harris, not only for allowing me to use his model, CMAT2, but also for spending a lot of time and effort helping me to use it, and at a later stage for helpful discussions and critical feedback on paper and thesis chapter drafts.

Next, I would like to thank my foreign collaborators, Thomas Ulich from the Sodankylä Geophysical Observatory (SGO, Finland) and Art Richmond from the National Center for Atmospheric Research (NCAR, US). They both taught me about their own fields of expertise and were supportive of my work in general during my visits and afterwards. Esa Turunen and Michael Mendillo played crucial roles in getting me to Sodankylä and Boulder, respectively, for which I am also grateful. Astrid Maute and Ben Foster helped me with running TIE-GCM and extracting and processing the data.

Further, I have benefited from helpful discussions with Alan Aylward, Erdal Yiğit, Mark Clilverd, Ray Roble, Stan Solomon, Lying Qian and George Millward. I am also thankful to Erdal for his implementation of the gravity wave schemes in CMAT2 and to Mark for proofreading one of my paper drafts.

On a more personal note, I would like to thank several people who have made a positive influence on my life over the past three years. Esa and Tero came up with lots of fun entertainment while I was in Sodankylä, and Colleen, Art and Maria, and Daniel invited me to join them for hiking or other activities while I was in Boulder. Back at home, in Leicester, I have thoroughly enjoyed working in the Radio and Space Plasma Physics (RSPP) group. I have many fond memories of my time here, and would like to thank Anna, for taking care of all SPARTAN matters and her love of tea and football, Tommi, for joining me to the swimming pool and doing a fantastic steak, Harmony, for being such a good friend, Atousa, for teaching me Persian (well, a little...) and always dragging everyone onto the dance floor, Rob, for teaching me what to actually do on that dance floor, Ranvir, for keeping me up to date with football scores while I was away, Ade (and others) for being pedantic, Jonny, for funny stories and experiments, Steve, for his love of

red wine (especially when followed by dad-dancing), Sarah, Suzie, Steph and later also Hannah, for baking (and sharing!) lots of lovely cakes, Niklas, for some great hikes in Poland, Carlos, for bringing the crossword and making good use of my pens, Tony, for providing me with some boxes, Gabby, for a friendly welcome into the office every morning, Pete, for some amazing dinners, and Colin, for the best version of Love Shack ever. I would also like to thank my housemates for two years, Nick and Gauthier, for being good company, organizing lots of parties, and letting me watch girly stuff on tv. I will miss all of you!

Contents

1. Introduction	1
2. Background theory	5
2.1 The Earth's atmosphere.....	5
2.1.1 Temperature structure.....	5
2.1.2 Pressure and density structure.....	6
2.1.3 Lapse rate and stability of the atmosphere.....	7
2.1.4 Radiative processes.....	8
2.1.5 Ionospheric structure.....	9
2.1.6 Global mean circulation.....	10
2.1.7 Waves.....	11
2.1.8 Atmospheric modelling and parameterizations.....	12
2.2 Sun-Earth connections.....	13
2.2.1 The solar cycle and solar emissions.....	13
2.2.2. Solar wind-magnetosphere interaction.....	14
2.2.3 Geomagnetic activity.....	15
2.3 The Earth's magnetic field.....	16
2.3.1 General characteristics.....	16
2.3.2 Variability.....	16
2.3.3 International Geomagnetic Reference Field.....	17
3. Introduction to long-term trends	19
3.1 Long-term trend analysis.....	19
3.2 Observed trends.....	20
3.2.1 Temperature.....	21
3.2.2 Density.....	22
3.2.3 Wind.....	22
3.2.4 Ionospheric parameters.....	23
3.3 Possible causes of observed trends.....	25
3.3.1 Changes in CO ₂ concentration.....	25
3.3.2 Changes in the concentration of other atmospheric constituents.....	26
3.3.3 Changes in solar and geomagnetic activity.....	26
3.3.4 Changes in the Earth's magnetic field.....	27
3.4 Modelled long-term trends.....	27
3.4.1 Temperature.....	27
3.4.2 Density.....	30
3.4.3 Winds.....	30
3.4.4 Ionospheric parameters hmF2 and foF2.....	31
3.5 Discussion and conclusions.....	31

4. Model descriptions	33
4.1 CMAT2 model description and settings	33
4.2 Gravity wave parameterizations in CMAT2	35
4.2.1 Rayleigh friction	35
4.2.2 Hybrid Lindzen Matsuno scheme (HLM) scheme	35
4.2.3 Medvedev-Klaassen (MK95) scheme	36
4.3 CMAT2 model validation.....	37
4.3.1 Temperature	37
4.3.2 Density	39
4.3.3 Winds.....	40
4.3.4 Ionospheric parameters	44
4.4 TIE-GCM.....	45
4.5 Model data processing	48
4.6 Conclusions.....	48
5. Modelled effects of changes in CO₂ and ozone concentration	49
5.1 Introduction.....	49
5.2 CMAT2 model settings	49
5.3 Differences 1995-1965 due to CO ₂ and ozone concentration changes	50
5.3.1 Temperature	50
5.3.2 Mesopause	53
5.3.3 Density	54
5.3.4 Wind	55
5.3.5 Ionospheric parameters	57
5.4 Physical discussion of the obtained responses	58
5.4.1 Constant pressure versus constant height reference frame	58
5.4.2 Shape of temperature response.....	59
5.4.3 Shape of density response.....	62
5.4.4 Seasonal differences	62
5.4.5 Additional effects of changes in ozone concentration.....	64
5.5 Comparison with other modelling studies and observations	65
5.5.1 Temperature	65
5.5.2 Mesopause	66
5.5.3 Density	66
5.5.4 Wind	67
5.5.5 Ionospheric parameters	68
5.6 General discussion, conclusions and further work	69
6. Sensitivity analyses of modelled, CO₂-induced trends	71
6.1 Introduction.....	71
6.2 CMAT2 model settings	72

6.3 Results.....	72
6.3.1 Temperature	72
6.3.2 Mesopause	74
6.3.3 Density	77
6.3.4 Wind strength.....	79
6.3.5 Ionospheric parameters	83
6.4 Improved trend estimates	85
6.4.1 Temperature	86
6.4.2 Mesopause	87
6.4.3 Density	88
6.4.4 Winds.....	89
6.4.5 Ionospheric parameters	90
6.5 Concluding remarks	91
7. Modelled effects of geomagnetic field changes on hmF2 and foF2	93
7.1 Introduction.....	93
7.2 Methods	96
7.3 Results.....	97
7.3.1 Global change in hmF2 and foF2.....	97
7.3.2 Seasonal and diurnal variation	99
7.4 Discussion	100
7.4.1 Cause of modelled changes in hmF2 and foF2.....	100
7.4.2 Implications for and comparison with other long-term trend studies .	105
7.5 Summary and conclusions.....	109
8. Solar and geomagnetic activity effects in long-term trend modelling	110
8.1 Introduction.....	110
8.2 CMAT2 and TIE-GCM model settings	110
8.3 Changes in CO ₂ and ozone concentration.....	111
8.3.1 Temperature	111
8.3.2 Density	113
8.3.3 Ionospheric parameters	115
8.4 Changes in the Earth's magnetic field	117
8.4.1 Global maps of hmF2 and foF2	117
8.4.2 Seasonal and diurnal variation	118
8.5 Physical discussion of the obtained responses	119
8.5.1 Changes in CO ₂ and ozone concentration	119
8.5.2 Changes in the Earth's magnetic field	121
8.6 Comparison with observations	123
8.6.1 Thermospheric density	123
8.6.2 Ionospheric parameters	124

8.7 Conclusions.....	124
9. Summary, conclusions and further work	126
9.1 Summary	126
9.2 General conclusions and further work	129
References	131

1. Introduction

Over the past century, long-term changes have occurred in the Earth's atmosphere. Many people will be familiar with the concept that changes in greenhouse gas concentrations, mainly CO₂ (see figure 1.1), are thought to have caused a global warming of the troposphere, by trapping infrared radiation emitted by the Earth's surface (see e.g. the report of the Intergovernmental Panel on Climate Change (IPCC), Solomon et al., 2007). Above the troposphere, in the middle and upper atmosphere, consisting of the stratosphere, mesosphere and thermosphere (see chapter 2 for further definitions), increasing the CO₂ concentration has a cooling effect, and any cooling in the middle and upper atmosphere should have a much larger magnitude than the warming in the troposphere (e.g. Andrews, 2000). Therefore, studying long-term change and trends in the middle and upper atmosphere can contribute to a better understanding of the effects of changing greenhouse gas concentrations.

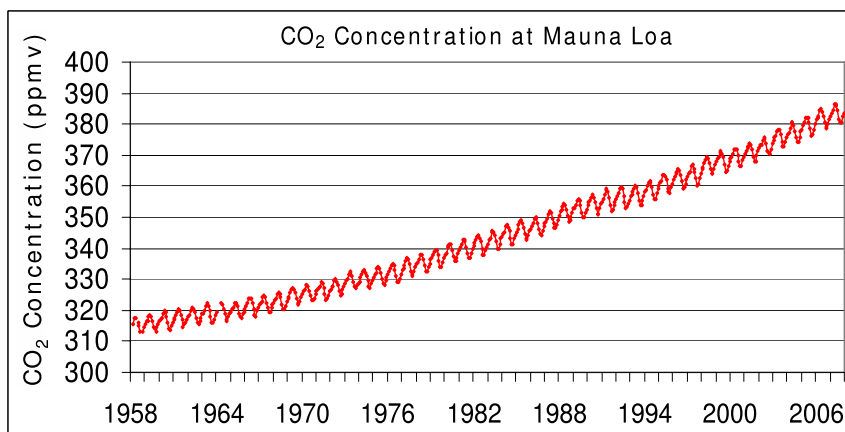


Figure 1.1. Change in CO₂ concentration (ppmv) from 1958 to 2006 at Mauna Loa, Hawaii. From Keeling et al. (2008).

Long-term changes in the middle and upper atmosphere may also have an influence on the climate in the troposphere through various coupling mechanisms between the troposphere and stratosphere (e.g. Baldwin and Dunkerton, 1999; Thompson et al., 2002). Further, satellites operating in the upper atmosphere will be affected by long-term changes in atmospheric density (as atmospheric drag affects their trajectories), and space-based navigational systems that rely on the propagation of radio waves through the ionosphere (the ionized part of the

atmosphere, existing from 50-60 km up to 1000 km altitude, see chapter 2) will be affected by long-term changes in this part of the atmosphere (e.g. Hargreaves, 1992).

Since the start of the space age, long-term changes in the middle and upper atmosphere have indeed been detected, as schematically illustrated in figure 1.2 (see chapter 3 for a more detailed overview). In general, the temperature and density have decreased, causing the middle and upper atmosphere to contract. The contraction of the atmosphere has been theoretically predicted to cause a lowering of the ionosphere (Rishbeth, 1990), and this is indeed observed in the lower part of the ionosphere (the D and E regions, see figure 1.2).

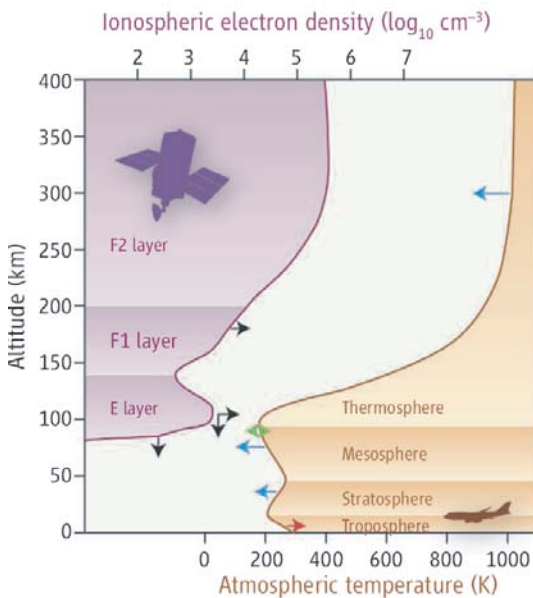


Figure 1.2. Illustration of the overall long-term trends as observed. Atmospheric layers (orange, right) are defined by the temperature profile. Ionospheric layers (purple, left) are defined by the electron density profile (shown here at midnight at the equator). Arrows denote the direction of observed changes in the past three to four decades: Red, warming; blue, cooling; green, no temperature change; black, changes in maximum electron density (horizontal) and the height of ionospheric layers (vertical). Most spacecraft fly at altitudes above 300 km. The aircraft and satellite shown are not to scale. From Laštovička et al. (2006).

However, higher up in the ionosphere, in the F region, long-term measurement records show large differences in ionospheric trends depending on location, season and local time. Also, the magnitudes of temperature trends in the

middle atmosphere are much larger than predicted by model simulations, while observed density trends in the thermosphere appear to be smaller than model predictions. These discrepancies suggest that other processes may also have played a role in causing the trends that are observed.

Recently, a few modelling studies have therefore focused on assessing the effects of changes in the ozone and water vapour concentrations in addition to changes in CO₂ concentration (Bremer and Berger, 2002; Akmaev et al., 2006). These studies found that changes in ozone concentration also contributed substantially to cooling and contraction of the middle and upper atmosphere, while changes in water vapour concentration had a smaller effect. However, the models used for these studies extended only up to 150-200 km, so that for instance effects on the F region of the ionosphere could not be assessed.

In this thesis, the Coupled Middle Atmosphere and Thermosphere model version 2 (CMAT2, described in chapter 4) was used, which covers an altitude range of 15 to 300-600 km (depending on geophysical conditions), to study the effects of changes in CO₂ concentration only and the combined effects of changes in CO₂ and ozone concentration on a range of atmospheric parameters (chapter 5). The actual levels of 1965 and 1995 are used to facilitate comparisons with data, as well as other modelling studies.

In the approach of chapter 5, which is the usual approach for studies of long-term trends or CO₂ doubling scenarios, two model simulations are compared in each case. It is assumed that these are representative of the actual behaviour of the atmosphere under the prescribed CO₂ (or CO₂ and ozone) levels, and that the difference between them reflects the response of the atmosphere to the change in CO₂ (or CO₂ and ozone) concentration. However, models can suffer from model noise (e.g. caused by numerical instabilities) and their results also depend on the approximations made, parameterizations used, and the choice of geophysical conditions. There are therefore some limitations to this approach, which will be further explored in chapters 6 and 8.

Chapter 6 focuses on the role of model noise and the gravity wave parameterization used in the model (see also Cnossen et al., 2008). Gravity waves affect the circulation in the middle atmosphere as they break and deposit their momentum, which in turn influences the temperature structure (see chapter 2 for background information). Gravity waves can not be resolved by global models, so that their effects need to be parameterized, and the type of parameterization that is used may influence the response to a change in CO₂ concentration that is obtained by the model. To test this, all simulations performed in chapter 6 were carried out with three different gravity wave parameterizations. Further, simulations with a wide range of CO₂ concentrations were used, so that noise

could be filtered out and the overall evolution of the studied parameters with increasing CO₂ concentration could be shown, leading to more robust trend estimates than can be obtained from two simulations only.

Chapter 8 focuses on the choice of solar and geomagnetic activity level as prescribed in the model. Both solar and geomagnetic activity vary over the solar cycle (see section 2.2), and the atmosphere, in particular the upper atmosphere, is strongly influenced by changes in these activity levels. Any perturbations, such as changes in CO₂ and ozone concentration, may therefore be expected to cause a different response, depending on the solar and geomagnetic activity level. To test how this might affect the results obtained in chapter 5, simulations with the CO₂ and ozone levels of 1965 and 1995 were carried out here for a range of combinations of solar and geomagnetic activity level.

In chapter 7 an alternative, or complementary, hypothesis for the cause of long-term trends in the ionosphere is examined, namely changes in the Earth's magnetic field (see also Cnossen and Richmond, 2008). The Earth's magnetic field varies slowly in strength and orientation with time (see section 2.3 for more information), and because the motions of charged particles in the ionosphere are influenced by the magnetic field, such variations could lead to a change in their distribution. To quantify the effects of changes in the Earth's magnetic field, simulations with the Thermosphere-Ionosphere-Electrodynamics general circulation model (TIE-GCM, described in chapter 4) with the magnetic fields of 1957 and 1997 were used. In chapter 8, the dependency of the results obtained with this model on the choice of solar activity level is also briefly studied.

In chapter 9 a summary of the main findings and conclusions of the previous chapters is given, as well as some suggestions for further work to be done in the field of long-term trends.

2. Background theory

This chapter will give an overview of the basic concepts that will be needed throughout the rest of this thesis. This consists of some background theory of the Earth's atmosphere (section 2.1), the connections between the Sun and Earth (section 2.2), and the Earth's magnetic field (section 2.3).

2.1 The Earth's atmosphere

2.1.1 Temperature structure

The temperature of the atmosphere varies most in the vertical direction due to absorption of solar radiation of different wavelengths at different heights. On the basis of the vertical temperature profile, the Earth's atmosphere can be divided into a set of layers ("spheres"), where boundaries between them are defined at inversions of the temperature gradient. Boundaries may occur at somewhat different heights and temperatures, depending on the local conditions, so they are not rigid, static features. A typical profile was given in figure 1.2.

The troposphere, also called the lower atmosphere, is the layer closest to the surface, and this is where most weather occurs. Depending on the latitude, it contains ~85-88% of the total mass of the atmosphere, and consists of ~78% of N₂, 21% of O₂ by volume, and smaller amounts of other gases.

Above the tropopause, the upper boundary of the troposphere, the stratosphere starts, with the ozone layer as an important feature. Absorption of solar UV radiation by ozone in the Hartley (200-300 nm) and Huggins (300-335 nm) bands is mainly responsible for heating in the stratosphere, causing an inversion of the temperature gradient, and therefore the existence of the stratosphere and the layer above, the mesosphere. The combination of stratosphere and mesosphere together is referred to as the middle atmosphere.

The region above the middle atmosphere is called the thermosphere, or sometimes upper atmosphere. Here the temperature starts to increase again with height due to absorption by O₂ in the Schumann-Runge bands (175-200 nm) and the Schumann-Runge continuum (100-180 nm). Above 150 km, heating due to EUV ionization of O, O₂ and N₂ becomes dominant. The maximum temperature that is reached in the thermosphere depends strongly on the solar activity level (see section 2.2.1), from ~700 K during solar minimum up to ~1300 K during solar maximum.

2.1.2 Pressure and density structure

Atmospheric pressure and density both decrease exponentially with height. This is due to the atmosphere being approximately in hydrostatic equilibrium, meaning that the gravitational force is balanced by the forces due to the vertical pressure gradient:

$$\frac{dp}{dz} = -M\rho_n\mathbf{g} = -\mathbf{g}\rho_m, \quad (2.1)$$

where p = pressure (Pa),
 z = height (m),
 M = mean molecular mass (kg),
 ρ_n = number density (m^{-3}),
 \mathbf{g} = gravitational acceleration (ms^{-2}),
 ρ_m = mass density ($\text{kg}\cdot\text{m}^{-3}$).

Pressure and density are related by an equation of state, which for an ideal gas is given by the ideal gas law, which can be written as:

$$p = \rho_n kT \quad \text{or} \quad p = \frac{kT\rho_m}{M}, \quad (2.2)$$

where T = temperature (K),
 k = Boltzmann's constant ($1.38\cdot 10^{-23} \text{ JK}^{-1}$).

The atmosphere of the Earth behaves approximately as an ideal gas, so (2.2) can be used to substitute $\rho_m = pM/kT$ in (2.1). Integrating that equation gives:

$$p = p_0 \exp\left(-g \frac{M}{k} \int_{z_0}^z \frac{dz'}{T(z')}\right). \quad (2.3)$$

In case of an isothermal temperature profile, i.e. $T = T_0 = \text{constant}$, this gives:

$$p = p_0 \exp\left(-\frac{gM(z - z_0)}{kT_0}\right) = p_0 e^{-(z-z_0)/H} \quad \text{with} \quad H = \frac{kT_0}{gM}, \quad (2.4)$$

where p_0 = pressure at z_0 (reference level),

H = scale height (m).

A similar equation can be derived for the mass density as a function of altitude:

$$\rho_m = \rho_{m,0} e^{-(z-z_0)/H}. \quad (2.5)$$

The scale height H is the height over which the pressure or density decreases by a factor of e . From its definition it follows that it varies with temperature, and is inversely proportional to the mean molecular mass. This means that heavier molecules have smaller scale heights, and therefore their density decreases more rapidly with height. This effect can be ignored as long as the atmosphere is well-mixed, as is the case for the so-called homosphere, which is the region below ~ 110 km. Around that altitude the turbopause is reached, which separates the homosphere from the heterosphere above. In the heterosphere molecular mixing can no longer compensate for the gravitational separation of lighter and heavier species by molecular diffusion, causing compositional changes with altitude.

2.1.3 Lapse rate and stability of the atmosphere

The lapse rate Γ gives the rate of decrease of temperature with height:

$$\Gamma(z) = -\frac{dT}{dz}. \quad (2.6)$$

The (dry) adiabatic lapse rate Γ_{ad} is the rate of decrease of temperature that an adiabatically rising parcel of air will experience, and is given by:

$$\Gamma_{ad} = -\frac{g}{C_p}, \quad (2.7)$$

where C_p = specific heat at constant pressure.

When the temperature in the atmosphere decreases less rapidly than the adiabatic lapse rate ($\Gamma < \Gamma_{ad}$), a parcel of air that rises adiabatically (for instance due to a small perturbation) will become colder than its surroundings, and therefore heavier, so that it will be forced back to its equilibrium position by

gravity. It may overshoot though, and oscillate around this position, which it will do at a characteristic frequency called the Brunt-Väisälä frequency, given by:

$$N = \sqrt{\frac{gd\theta}{\theta dz}}, \quad (2.8)$$

where θ = potential temperature.

The potential temperature of an air parcel is the temperature it would acquire if it were compressed adiabatically to a standard reference pressure (often chosen to be 1 bar), and is mathematically defined as:

$$\theta = T \left(\frac{p_0}{p} \right)^{(\gamma-1)/\gamma} \quad \text{with} \quad \gamma = \frac{C_p}{C_v}, \quad (2.9)$$

where C_v = specific heat at constant volume.

When $\Gamma > \Gamma_{ad}$, an adiabatically rising parcel of air will become warmer, and hence lighter than its surroundings, so that it will continue to rise. In this case the atmosphere is vertically unstable.

2.1.4 Radiative processes

The overall temperature structure of the Earth's atmosphere is determined by the absorption and emission of radiation. When electromagnetic radiation is absorbed, the energy of the photon is transferred to the absorber, which is used for transitions in its internal energy state, or for photo-ionization or photo-dissociation when the energies involved are high enough. For atoms, different internal energy states are defined by particular arrangements of their electrons in atomic orbitals, while molecular energy states are also determined by their modes of vibration and rotation. At sufficiently high pressures, when collisions between molecules are frequent, internal energy will be transferred to kinetic energy, which is shared with surrounding molecules, resulting in local heating. Section 2.1.1 already discussed which species are mainly responsible for heating different parts of the middle and upper atmosphere.

The Earth's atmosphere also emits radiation. Energy is then drawn from molecular kinetic energy, leading to local cooling of the atmosphere. Radiative

cooling in the middle atmosphere is dominated by emission by CO₂ in the 15 μm band, with a smaller contribution from 9.6 μm emission by O₃. Between 120 and 200 km 5.3 μm emission of NO is the major radiative cooling mechanism.

As long as the atmosphere is in local thermodynamic equilibrium (LTE), emitted radiation will resemble a Planck black body function. This is the case until ~70-80 km. Above that altitude collisions become too infrequent to maintain LTE conditions, and the atmosphere is said to be in non-local thermodynamic equilibrium (non-LTE). CO₂ cooling has local maxima both near the stratopause temperature maximum, where LTE applies, and near 100 km, within the non-LTE region. NO cooling is also within the non-LTE region.

Rather than being absorbed, radiation may also be scattered. In that case internal excitation energy is re-emitted before it is transferred to kinetic energy. No energy is lost in this process, unless a lower energy photon is re-emitted, but radiation may be scattered in any direction, and therefore it influences the radiation distribution, which affects subsequent absorption.

2.1.5 Ionospheric structure

Absorption of short-wavelength solar radiation (X-ray to far UV) in the upper mesosphere and thermosphere can cause ions to form through photo-ionization. Ions may also form due to impacting energetic particles, coming for instance from the solar wind (see section 2.2.1). This process is called impact ionization. Because the density of the atmosphere is very small in the upper atmosphere, ions do not easily encounter electrons to form neutral molecules (i.e. their mean free path is large), and are therefore relatively long-lived. The ionized part of the atmosphere is called the ionosphere, and starts already in the mesosphere, from 50-60 km, and continues throughout most of the thermosphere.

Within the ionosphere, several layers can be distinguished based on the vertical profile of the concentration of charged particles, arising from variations in ion production rates. These are known as the D, E, and F layers, and during the day, the F layer can be subdivided into an F1 and F2 layer. In the D and E layers mostly N₂ and O₂ are ionized, while in the F region it is mostly O.

The positions of the layers are approximately shown in figure 2.1, but vary with day and night, solar activity level, latitude, season, etc., since absorption of solar radiation is for a large part responsible for the production of ions. Impact ionization is less dependent on the Sun, because only a fraction of the particles comes from the solar wind, and additional particles are supplied by galactic cosmic

rays, or by other regions in the ionosphere. Impact ionization is therefore the dominant process during the night and at high latitudes, where relatively little solar radiation is available.

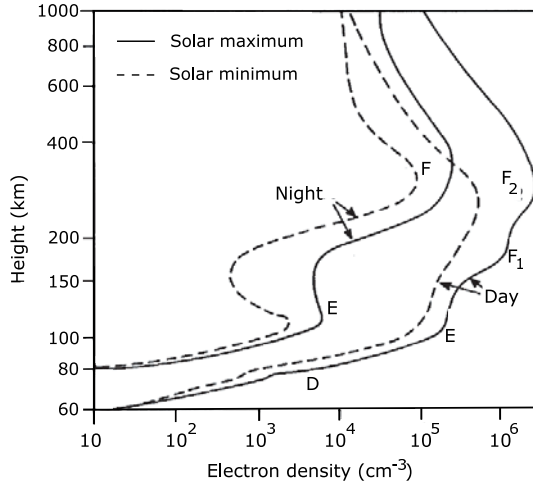


Figure 2.1. Schematic ionospheric profiles for solar minimum (dashed) and solar maximum (solid) at night and day. After Hargreaves (1992).

In the following chapters, the height of the peak of the F2 layer, h_mF2 , and the so-called critical frequency of the F2 layer, f_oF2 , are studied. The critical frequency is the highest frequency at which reflection of a radio pulse that is transmitted vertically upwards (usually by an ionosonde, a type of radar used to probe the ionosphere) still occurs. The critical frequency f_oF2 is related to the maximum electron density of the F2 layer, denoted N_mF2 , through the following empirical relationship:

$$N_mF2 = 1.24 \cdot 10^{10} (f_oF2)^2, \quad (2.10)$$

where N_mF2 is in m^{-3} and f_oF2 in MHz.

2.1.6 Global mean circulation

In the stratosphere, atmospheric convection is described to first order by the Brewer-Dobson circulation (figure 2.2). In the Brewer-Dobson circulation, air enters the stratosphere through upward motion in the tropics, moves poleward at 30-50 km (depending on season and dynamical factors), and descends at middle

and polar latitudes. The middle latitude descending air is transported back into the troposphere, while the polar latitude descending air is transported into the polar lower stratosphere. Higher up, in the mesosphere, there is a large scale north-south residual circulation of air from the summer pole toward the winter pole.

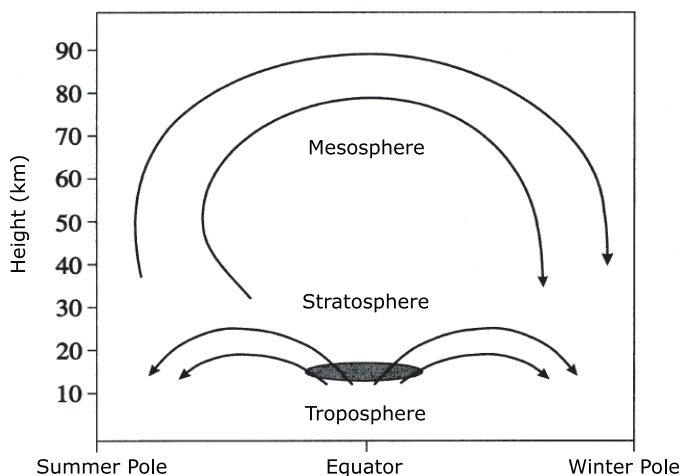


Figure 2.2. Schematic plot of the Brewer-Dobson circulation in the stratosphere and the residual circulation in the mesosphere at solstice. After Andrews (2000).

The circulation in the middle atmosphere is to some extent driven by temperature gradients and tropospheric circulation, but most importantly by the dissipation of gravity waves and Rossby waves, also called planetary waves (e.g. Holton, 1982, 1983; Garcia and Solomon, 1985), which are discussed in the following section (2.1.7). This causes the middle atmosphere to be out of radiative equilibrium. For instance, the summer mesopause is colder than the winter mesopause, because air rises at the summer pole, so that it cools adiabatically, while it descends and heats at the winter pole.

2.1.7 Waves

Gravity waves form when an air parcel is displaced from its hydrostatic equilibrium position, for instance by air flow over a mountain, and gravity acts as a restoring force. This causes the air parcel to oscillate about its equilibrium position and generates a wave. Gravity waves typically have a horizontal scale of several tens to hundreds of km, with periods of minutes to hours. Their amplitude is small in the troposphere, but as they propagate upward, the density of the

atmosphere decreases, causing their amplitude to increase. This causes the waves eventually to break in the mesosphere and lower thermosphere, where they deposit their momentum and energy, changing the direction and/or strength of existing winds, and thereby affecting the large scale circulation, as mentioned in the previous section. Since the upward propagation of gravity waves also depends on the background winds, their effect on these winds is dependent on the initial wind field itself.

The mechanism(s) by which gravity waves are dissipated are still not fully understood. Lindzen (1981) proposed that gravity waves start to break (saturate) when the temperature perturbation induced by the wave starts to result in a lapse rate larger than the adiabatic lapse rate, causing local instability of the atmosphere (see section 2.1.3). He further suggested that from this point onward, just enough turbulence is created to prevent the waves from further growth. Weinstock (1982) on the other hand proposed that a gravity wave of a certain wavelength is dissipated due to off-resonant interaction with waves of smaller vertical scales, a theory often referred to as "dissipation by nonlinear diffusion". Several others have offered variations on or refinements of the above two theories (see e.g. the reviews by Fritts (1984) and Fritts and Alexander (2003)).

Rossby waves, also called planetary waves, can also form by the interaction of winds with large scale topography, but have the variation in Coriolis force with latitude as a restoring force. They can have a horizontal extent of thousands of kilometres, with long periods of a few days up to 30 days. Rossby waves can only propagate vertically when the background flow is westward, and not too strong (Charney and Drazin, 1961). If they do propagate upwards, the increase in amplitude with height due to the decreasing density of the atmosphere causes the waves to break, as with gravity waves. Rossby waves coming from the troposphere generally break in the stratosphere, but they may form at higher altitudes as well, since their effects have also been observed in the upper atmosphere (e.g. Forbes, 1996; Meyer, 1999).

2.1.8 Atmospheric modelling and parameterizations

Atmospheric general circulation models (GCMs) attempt to simulate the behaviour of the atmosphere, or certain aspects of this behaviour, by solving a complex set of equations describing dynamical, radiative and/or chemical processes. These equations need to be solved numerically, which can be done by dividing the atmosphere in a number of discrete cells, as is done in the models used in this thesis. More cells result in greater accuracy, but also require more

computing power/time. Any processes that take place on length scales smaller than the cell size can not be resolved directly and need to be parameterized. In the case of a three-dimensional global model, with a typical cell size of the order of 10^2 - 10^3 km, this includes the effects of gravity waves. Also, parameterizations may be used as a simplification, when calculations would otherwise become very complex and take up too much computing power/time. This may be done for instance for the calculation of non-LTE CO₂ cooling.

2.2 Sun-Earth connections

Since the Earth's atmosphere, and especially the thermosphere-ionosphere system, depends strongly on radiation and energetic particles from the Sun, this section will discuss the emissions from the Sun and its influences on the Earth in some more detail.

2.2.1 The solar cycle and solar emissions

The activity of the Sun varies over an approximately 11 year cycle, called the solar cycle. When the Sun is active, it is brighter and emits more radiation. The variation in irradiance over the solar cycle is of order 0.1% near the peak of the spectrum (in the visible domain), but can exceed 100% in the UV and EUV.

There are various indices for solar activity, but throughout the rest of this thesis the F10.7 index will be used. F10.7 refers to the flux of radio emission from the Sun at a wavelength of 10.7 cm (2.8 GHz frequency), which has been observed to follow the changes in the solar UV radiation over the solar cycle. F10.7 is measured in solar flux units (sfu, equal to 10^{-22} Wm⁻²Hz⁻¹), and varies from ~ 70 sfu at solar minimum to ~ 230 sfu at solar maximum.

In addition to electromagnetic radiation, the Sun also continuously emits charged particles (plasma) from its corona, which is called the solar wind. Two types of solar wind can be distinguished: a fast uniform wind moving at an average speed of ~ 750 kms⁻¹ and a variable slow wind moving at ~ 400 kms⁻¹. There are also discrete emissions in the form of coronal mass ejections (CMEs) and solar flares (sudden brightenings), which both release large amounts of highly energetic particles into space. These occur more frequently when the Sun is active.

As the solar wind moves out into space, it carries with it the magnetic field of the Sun, forming the interplanetary magnetic field (IMF). The Sun's magnetic

field is primarily directed inward on one of its hemispheres and outward on the other, reversing every ~ 11 years just before solar maximum.

2.2.2. Solar wind-magnetosphere interaction

As the solar wind moves towards the Earth, it encounters the Earth's magnetosphere (see figure 2.3), the zone around the Earth where the Earth's magnetic field is dominant. Shaped by the solar wind, the magnetosphere is compressed on the dayside, while it extends much further out into space on the night side. This part is called the (magneto)tail. In the northern half of the tail, the magnetic field points roughly towards the Earth, and in the southern half it points roughly away. At the centre of the tail opposite magnetic orientations lie next to each other, and currents can flow.

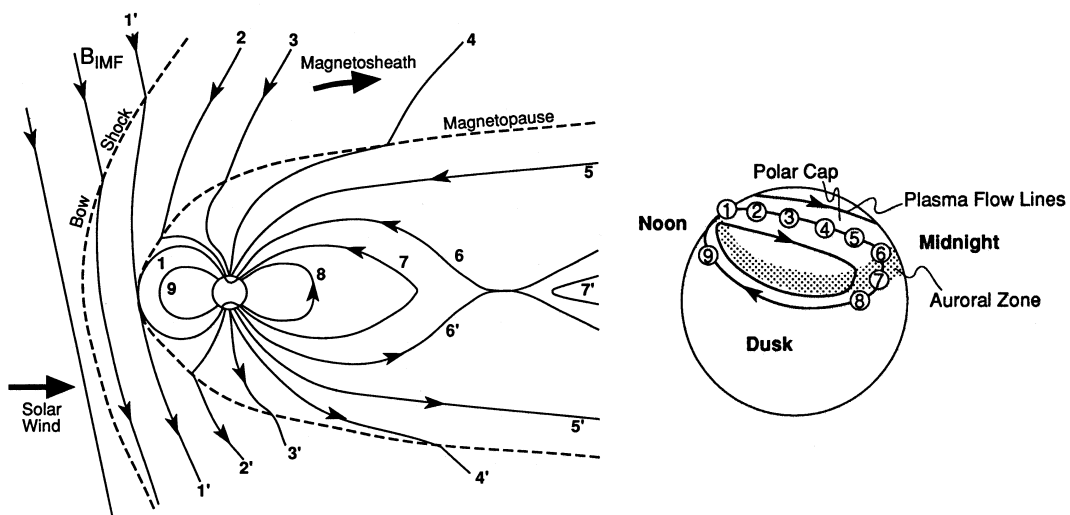


Figure 2.3. Left: Illustration of the magnetosphere and magnetospheric convection as driven by magnetic reconnection. Numbered field lines show the succession of configurations a geomagnetic field line assumes after reconnection with an IMF field line at the front of the magnetosphere. Right: Illustration of the positions of the feet of the numbered field lines in the northern high-latitude ionosphere and the corresponding ionospheric plasma flows. After Kivelson and Russell (1995).

The Earth's magnetic field and the solar wind start to interact with each other at the bow shock, usually ~ 12 Earth radii out into space. The bow shock is a shock wave that is produced as the solar wind is slowed by the Earth's magnetic field, causing compression of the solar wind and the release of heat. Following the

bow shock, there is a turbulent transition zone called the magnetosheath. The boundary between the magnetosheath and the magnetosphere is referred to as the magnetopause.

Field lines of the IMF can connect to field lines of the Earth's magnetic field on the sunward side of the magnetosphere, as first proposed by Dungey (1961). This process is called magnetic reconnection. Because of the flow of the solar wind, linked field lines are dragged along towards the tail, where they eventually come close enough to reconnect again, forming a new closed geomagnetic field line and a new interplanetary field line (see figure 2.3).

When magnetic reconnection occurs, magnetic energy is released, which is partly transformed to kinetic energy of any particles that were on the field lines, and partly to heat. Some of the particles are ejected away from the Earth, while others are fired off toward the Earth, following the Earth's magnetic field lines. As field lines are pushed by the solar wind from the day-side to the night-side, any particles on those field lines are driven in that direction. This causes an anti-sunward flow of plasma in the ionosphere over the polar cap, while a return flow occurs at lower latitudes (see figure 2.3).

Energetic particles entering the Earth's atmosphere from the magnetosphere, a process often referred to as particle precipitation, transfer their kinetic energy to atmospheric molecules through collision, and can be an important heat source at high latitudes. Also Joule heating by ionospheric electric currents associated with the ionospheric convection sketched in figure 2.3 can be important at high latitudes.

2.2.3 Geomagnetic activity

Interaction of energetic particles with the atmosphere and the flow of currents arising from plasma convection in the ionosphere can cause perturbations in the magnetic field measured close to the surface. The level of disturbance of the magnetic field is dependent on irregularities in the solar wind, but is referred to as the geomagnetic activity level.

The geomagnetic activity level can be expressed using various indices, including the Ap, aa and Kp indices, which can all be derived from the K index. The K index is related to the maximum fluctuations of the horizontal components of the observed geomagnetic field, relative to a quiet day (a day with few disturbances due to the solar wind), during a three-hour interval. The Kp index is the mean standardized K index from 13 geomagnetic observatories at intermediate latitudes. This is the index that will be used throughout this thesis.

The Kp index ranges from 0 to 9, and when the index is larger than 5, we speak of a magnetic storm. This is most common when the solar wind is particularly strong, or when a shock wave forms, for instance after a CME or flare on the Sun. When geomagnetic activity is high, particle precipitation and Joule heating become more important heat sources at high latitudes.

2.3 The Earth's magnetic field

2.3.1 General characteristics

The magnetic field of the Earth is generated in the Earth's liquid outer core, and propagates outwards to the Earth's surface and beyond, decaying in strength as $1/r^3$, r being the distance to the centre of the Earth. At the Earth's surface the field strength varies from $\sim 30,000$ nT at the equator to $\sim 60,000$ nT at the poles.

The magnetic field at and close to the Earth's surface resembles the field caused by a dipole that is somewhat misaligned with the Earth's rotational axis. The magnetic poles, the positions where the magnetic field direction is perpendicular to the Earth's surface, are therefore close to the geographical poles, but do not exactly coincide. This is also due to higher order pole contributions to the field.

The angle between the horizontal component of the Earth's magnetic field and the geographic north is called the declination D . The angle between the field and the Earth's surface is called the inclination I .

2.3.2 Variability

The Earth's internal magnetic field is not stationary, but varies over time in both strength and direction. Also, the relative contributions of the dipole component of the field (the main component) and higher order poles change over time. Timescales of changes in the magnetic field vary from decades to millions, or even tens of millions of years.

Complete reversals of the magnetic field occur on average every few hundred thousand years, but periods an order of magnitude smaller or larger are not uncommon. The transition from one polarity to another takes place over a few thousand years, which is short compared to the periods of stable polarity in between.

On timescales of a few thousand years, the direction of the field can change considerably as well, and sometimes even a short period of the opposed polarity occurs then. However, because of the short time-scale, such an event is classified as a magnetic excursion rather than as an actual reversal. During a magnetic excursion, the field does not necessarily reverse completely; a change in position of one of the poles of 45° or more is enough to qualify as an excursion. Examples of recent excursions are the Laschamp event (~41,000 years ago) and the Blake event (~120,000 years ago).

Smaller scale variability, occurring over decades to centuries, is called secular variation. Rapid changes in secular variation, taking place over 1 or 2 years, are sometimes referred to as geomagnetic jerks. Secular variation involves both changes in direction, and therefore in the position of the magnetic poles, and changes in field strength. Since the 19th century, the magnetic field has globally weakened by ~10%.

2.3.3 International Geomagnetic Reference Field

A standard mathematical description of the Earth's main magnetic field, called the International Geomagnetic Reference Field (IGRF) is released every 5 years by a team of geophysicists (for the most recent update see Maus et al., 2005). The IGRF is given in the form of a set of coefficients of a truncated spherical harmonics series, which represents the scalar potential of the Earth's magnetic field V . This is related to the magnetic field \mathbf{B} by:

$$\mathbf{B} = -\mu\nabla V, \quad (2.11)$$

where $\mu =$ magnetic permeability of free space ($4\pi \cdot 10^{-7} \text{ NA}^{-2}$).

The spherical harmonics expansion of V is given by:

$$V(r, \lambda_c, \varphi, t) = R \sum_{n=1}^{n_{\max}} \left(\frac{R}{r}\right)^{n+1} \sum_{m=0}^n \left[g_n^m(t) \cos m\varphi + h_n^m(t) \sin m\varphi \right] P_n^m(\lambda_c), \quad (2.12)$$

where $r =$ distance from the centre of the Earth,
 $\lambda_c =$ colatitude,
 $\varphi =$ longitude,
 $R =$ magnetic reference radius (6371.2 km),

$g_n^m(t)$ and $h_n^m(t)$ = coefficients at time t ,

$P_n^m(\lambda_c)$ = Schmidt semi-normalized associated Legendre functions of degree n and order m .

The functions $P_n^m(\lambda_c)$ are related to the associated Legendre polynomials $P_{n,m}$ by:

$$P_n^m = P_{n,m} \quad \text{for } m = 0, \quad (2.13a)$$

$$P_n^m = \left[\frac{2(l-m)!}{(l+m)!} \right]^{\frac{1}{2}} P_{n,m} \quad \text{for } m > 0. \quad (2.13b)$$

The associated Legendre polynomials $P_{n,m}(\lambda_c)$ have $(n-m)$ zeros for $0 \leq \theta \leq 180$, dividing a meridian (i.e. a longitudinal line) into $(n-m+1)$ zones of alternating sign. Similarly, $\sin(m\varphi)$ and $\cos(m\varphi)$ have $2m$ zeros, dividing a line of latitude into $2m$ meridional sectors of alternating sign.

The $n = 1$ term in the series represents a magnetic dipole field, the $n = 2$ term a quadrupole field, and so on. The Earth's magnetic field is dominated by the dipole term, but there are also contributions from higher order terms. By truncating the series at a value n_{max} only those terms that are dominated by contributions from internal sources are included in the description. This way, the IGRF is an approximation of the Earth's magnetic field for that part of the field that has its origin inside the Earth.

For epochs between 1900 and 2000 the truncation is at $n_{max} = 10$, resulting in 120 coefficients, while from 2000 it was decided that the truncation should be at $n_{max} = 13$, resulting in 195 coefficients. In between modelling epochs, it is assumed that coefficients can be linearly interpolated. For the 5 years after the most recent epoch also a linear secular variation model is provided, allowing forward extrapolation. This model is truncated at $n = 8$ and has 80 coefficients.

3. Introduction to long-term trends

Throughout this thesis the phrase “long-term trend” will be used. It is worth defining this more precisely: by “long-term” is meant “over several decades”, say 30-40 years, and a “trend” is defined as a (nearly) linear change per unit time, for instance a change in temperature in $\text{K}\cdot\text{decade}^{-1}$, that stays approximately constant over the long-term period considered. When the change is non-linear over the time window considered the term “long-term change” is more appropriate (Laštovička et al., 2008).

We will concentrate here on the time window from the mid-1950s or mid-1960s to the mid-1990s, since most long-term trends that have been observed and discussed in the literature are based on measurements from this period. However, we note that any trends within this time window do not necessarily remain in place for longer or other time frames, and certainly do not continue indefinitely. Rather, the atmosphere goes through various long-term cycles, and any trend found over a few decades is likely to be part of a longer timescale variation. The trends found and discussed in the following do therefore depend to some extent on the choice of time window for study.

3.1 Long-term trend analysis

To obtain a long-term trend, first of all a consistent data set over the entire time window of interest is needed. Since instruments and measurement techniques usually change over the course of a few decades, the data must be carefully checked for inconsistencies arising from technical changes. Also, a long-term data set usually contains gaps, which must be treated with care in subsequent analysis.

Further, any effects of cyclical behaviour on shorter timescales than the period that is studied must be accounted for. This includes seasonal and diurnal cycles, the solar cycle, and some data may also need to be corrected for fluctuations in geomagnetic activity. There are various ways of achieving this.

First of all, data may be binned according to season and/or local time to obtain a trend valid for the season and/or local time in question. Data may also be binned according to solar activity level, and even to geomagnetic activity level, but usually there is not sufficient data available to bin according to all these categories at the same time.

In addition to binning, or as an alternative, the data X_{obs} may be fitted to a theoretical data set X_{th} , following an equation of the form:

$$X_{th} = A + B \cdot S + C \cdot Kp, \quad (3.1)$$

where S is a solar activity proxy (e.g. sunspot number or F10.7 solar flux), Kp the Kp index (or another geomagnetic activity indicator), and A , B , and C are the coefficients that give the best fit. Either the absolute or relative difference ΔX between X_{th} and X_{obs} is then used to obtain a linear trend according to:

$$\Delta X = a + b \cdot \text{year} . \quad (3.2)$$

It is also possible to filter out seasonal influences by adding an annual and semi-annual sine and cosine to equation 3.1.

Though many studies have used the above regression technique, variations occur due to the use of different solar and geomagnetic activity proxies, the use of a relative or absolute ΔX , or by using a quadratic dependency on solar activity level instead of the linear one as in equation 3.1. Laštovička et al. (2006) investigated how differences in analysis technique affect the obtained result and found that most methods give similar trends, but in a few cases the differences are substantial.

A third technique, which has been used by only a few investigators (Poole and Poole, 2002; Yue et al., 2006), involves the use of artificial neural networks. A neural network is a system of interconnected computational elements similar to biological neural networks. Based on a set of input parameters and a validation data set it can be trained to find the dependency of the desired output on the input parameters in an iterative process in which the difference between calculated and observed values is minimized. When applying this to long-term trend analysis, input parameters would be the day number, local time, solar activity level, geomagnetic activity level, and possibly the chronological position of each data point to represent the long-term trend in the data. The neural network is then trained to find the output parameter, for instance foF2, for any combination of the input parameters, using the data that is available.

3.2 Observed trends

Long-term trends in many parameters have been observed throughout the middle and upper atmosphere, including the ionosphere. Here we give an overview of trends found in temperature, density, wind, and the ionospheric F2 layer parameters hmF2 and foF2.

3.2.1 Temperature

Long-term observations of the temperature in the stratosphere and mesosphere over the past decades were summarized by Ramaswamy et al. (2001) and Beig et al. (2003), respectively, combining trends obtained from measurements by radiosondes, rocketsondes, lidar, and satellite instruments. In the thermosphere only a few long-term data sets are available, mostly based on indirect measurements, such as a trend in the height of the red-line emission layer of atomic oxygen at 630 nm near 270 km (Semenov, 1996). Table 3.1 gives an overview of trends reported in the literature.

Semenov (1996) inferred a temperature decrease of 30 K-decade⁻¹ based on a downward movement of the atomic oxygen layer at a rate of 10 km-decade⁻¹, which seems a rather large trend compared to typical trends in ionospheric layer heights (section 3.2.4). Still, Holt and Zhang (2008) also found a very large trend of -50 K-decade⁻¹ at 350-400 km at Millstone Hill (46.2°N, 288.5°E), based on incoherent scatter data.

ΔT (K-decade ⁻¹)	Altitude (km)	Location	Period	Reference
-0.6	16-21	global mean	1979-1994	Ramaswamy et al. (2001)
-4 to -3	16-21	poles	1979-1994	Ramaswamy et al. (2001)
-0.75	20-35	45°N	1979-1994	Ramaswamy et al. (2001)
-2.5	50	45°N	1979-1994	Ramaswamy et al. (2001)
-2	50-70	mid-latitudes	variable, within 1965-1995	Beig et al. (2003)
-7 to 0	70-79	variable	variable, within 1965-1995	Beig et al. (2003)
-2 to +2	80-100	variable	variable, within 1965-1995	Beig et al. (2003)
+8	110	unknown	1955-1995	Lysenko et al. (1999)
-30	270	unknown	1975-1995	Semenov (1996)
-50	350-400	Millstone Hill (46.2,-71.5)	1978-2007	Holt and Zhang (2008)

Table 3.1. Observed trends in temperature throughout the middle and upper atmosphere, sorted by altitude region. Also the period and location of observations that the trends are based on are given. Latitudes are positive north; negative south, and longitudes positive east; negative west.

3.2.2 Density

On the basis of satellite drag data, Keating et al. (2000), Emmert et al. (2004, 2008) and Marcos et al. (2005) found globally averaged decreasing trends in density between altitudes of 200 and 700 km (table 3.2). Emmert et al. (2004, 2008) also studied the dependency of trends on various parameters, such as solar and geomagnetic activity, by calculating trends separately for binned data (as described in section 2.1). Emmert et al. (2004) found that trends were highest for low solar activity ($F_{10.7} < 90$), and possibly also slightly dependent on geomagnetic activity, with somewhat stronger trends for disturbed conditions. This may explain why Keating et al. (2000), who used data from solar minimum years only, found relatively large trends. Trends were largely independent of local time, season and latitude. However, in a more recent study, Emmert et al. (2008) reported that there is a dependency on the season, with trends being strongest in October and weakest in January and February.

$\Delta\rho$ (%·decade ⁻¹)	Altitude (km)	Location	Period	Reference
-2	200	global mean	1966-2001	Emmert et al. (2004)
-4.9	350	global mean	1976, 1986, 1996	Keating et al. (2000)
-1.7	400	global mean	1970-2000	Marcos et al. (2005)
-2.7	400	global mean	1967-2007	Emmert et al. (2008)
-3	450	global mean	1966-2001	Emmert et al. (2004)
-4	700	global mean	1966-2001	Emmert et al. (2004)

Table 3.2. Observed trends in density in the thermosphere, sorted by altitude region. Also the period and location of observations that the trends are based on are given.

3.2.3 Wind

Long-term trends in meridional and zonal wind have been derived from observations mainly at a height of 90-100 km, made using radar techniques, and only in the northern hemisphere. Due to the high variability of winds it is difficult to establish a statistically significant trend, and in many cases a significant trend can in fact not be obtained, in particular when it concerns the meridional wind. Further, trends depend on the season, and may also show large local differences. Jacobi et al. (2005) showed for instance that trends for two relatively close

stations, Collm and Obninsk, were rather different from each other, and even had opposite signs for some seasons. Table 3.3 gives an overview of annual mean trends in meridional (v_m) and zonal (v_z) wind as reported in the literature, sorted by latitude.

Δv_m (ms^{-1} $decade^{-1}$)	Δv_z (ms^{-1} $decade^{-1}$)	Altitude (km)	Station	Lat.	Lon.	Period	Ref.
1.13	-0.97	90-100	Heiss Islands	80.6	58.0	1965-1985	1
0.64	-7.00 (>99%)	90-100	Molodezhnaya	68	45	1967-1986	1
3.22	-4.46 (>95%)	90-100	Obninsk	55	38	1964-1981	1
0.16	-2.02	90-100	Kühlungsborn	54	12	1976-1994	1
1.81 (>99%)	-1.37 (>95%)	90-100	Collm; Kühlungsborn	51; 54	13; 12	1964-1994	1
0.20	0.92	90-100	Saskatoon	52	-107	1979-1988	1
1.6±1.0 (85%)	3.7±1.3 (98%)	90-100	UK	52	-1	1988-2000	2
1.6 (>95%)	2.5 to 4.0 (95%)	90-100	Collm	51	13	1979-2004	3
-1.47	-28.94 (>99%)	90-100	Atlanta	34	84	1975-1986	1
-6.6		86	Tirunelveli	8.7	77.8	1993-2006	4

Table 3.3. Observed trends in meridional and zonal wind at ~90-100 km at a number of stations, sorted by latitude. For some trends an error estimate and/or confidence level (in brackets) is provided. All other trends are not statistically significant, except the trend in meridional wind at Tirunelveli, for which no information on statistical significance or confidence level was provided. Latitudes are positive north; negative south, and longitudes positive east; negative west. References are: 1 – Bremer et al. (1997), 2 – Middleton et al. (2002), 3 – Jacobi and Kürschner (2006), 4 – Sridharan et al. (2007).

3.2.4 Ionospheric parameters

When considering long-term changes in the ionosphere, we concentrate on the ionospheric parameters hmF2 and foF2. Long-term trends in hmF2 and foF2 (and sometimes foE, the critical frequency of the E layer) have been observed at many ionospheric stations, as summarized in table 3.4. Typical trends in hmF2 range from decreases of a few km-decade⁻¹ up to increases of the same order of magnitude, and trends in foF2 range from about -0.4 to +0.1 MHz-decade⁻¹.

Trends in both parameters vary considerably depending on season, local time, and location.

Some regional patterns have been found: Bremer (1998) reported that west of 30°E trends in both parameters are mostly negative and east of 30°E mostly positive, and Danilov and Mikhailov (1999) found that the magnitude of trends in foF2 increases with geomagnetic latitude. Still, others found no consistent dependency on (geomagnetic) latitude or longitude (Upadhyay and Mahajan, 1998), and even stations that are rather close to each other may exhibit very different trends (Bremer, 2001).

$\Delta hmF2$ (km·decade ⁻¹)	$\Delta foF2$ (MHz·decade ⁻¹)	Station	Lat.	Lon.	Period	Ref.
+1.9	+0.00	Churchill	58.8	-94.2	~1957-1991	1
+2.1	+0.01	Ottawa	45.4	-75.9	~1957-1991	1
-3.5	+0.17	Huancayo	-12.0	-75.3	~1957-1991	1
-5 to +15	-0.5 to +0.1	Concepción	-36.8	-73.0	1958-1994	2
-10 to +1.3	-0.04	Port Stanley	-51.7	-57.8	1957-1995, ~1957-1991	3,1
-6.3 to +2.5	-0.9 to +0.9	Arg. Islands	-65.2	-64.3	1957-1995, 1957-1998	3,4
-8.8 to -1.3	-0.17	Sodankylä	67.4	26.7	1957-1995, ~1957-1991	5,1
+1.6	-0.07	Lycksele	64.6	18.8	~1957-1991	1
-1.7	-0.16	Yakutsk	62.0	129.6	~1957-1991	1
+0.3	-0.02	Leningrad	60.0	30.7	~1957-1991	1
-5.8	-0.43 to +0.08	Uppsala	59.8	17.6	~1957-1991, 1957-1998	1,4
+0.2	-0.08 to 0.00	Tomsk	56.5	84.9	~1957-1991, unknown	1,6
+2.9	-0.08 to -0.05	Sverdlovsk	56.4	58.6	~1957-1991, unknown	1,6
+0.6	0.00	Gorky	56.2	44.3	~1957-1991	1
+2.4	-0.05 to -0.03	Moscow	55.5	37.3	~1957-1991, unknown	1,6
-4.5 to -1.3	-0.2 to +0.01	Juliusruh	54.6	13.4	~1957-1991, 1976-1996	7,1,8
-0.2	-0.06	Irkutsk	52.5	104.0	~1957-1991	1
	-0.25 to +0.05	Slough	51.5	-0.6	1957-1998, ~1957-1991	4,7,1
	+0.09	Dourbes	50.1	4.6	~1957-1991	1
-5.0	0.00	Poitiers	46.6	0.3	1957-1990	7
-1.3	+0.03	Wakkanai	45.4	141.7	~1957-1991	1
+4.0	-0.03 to +0.05	Alma-Ata	43.3	76.9	unknown, ~1957-1991	6,1
-2.2	-0.05	Boulder	40.0	-105.3	~1957-1991	1
-1.5	-0.01	Akita	39.7	140.1	~1957-1991	1
+8.5	+0.03	Ashkhabad	37.9	58.3	~1957-1991	1
-5.1 to -1.3	-0.06 to -0.02	Kokubunji	35.7	139.5	1958-2003, ~1957-1991	9,1
-1.5	+0.04	Yamagawa	31.2	130.6	~1957-1991	1
+0.6	+0.15	Okinawa	26.3	127.8	~1957-1991	1

$\Delta hmF2$ ($km \cdot decade^{-1}$)	$\Delta foF2$ ($MHz \cdot decade^{-1}$)	Station	Lat.	Lon.	Period	Ref.
	-0.6 to -0.1	Ahmedabad	23.0	72.6	1955-1996	10
-1.2	0.00	Maui	20.8	-156.5	~1957-1991	1
	+0.04	Townsville	-19.6	146.9	~1957-1991	1
-5.8	-0.20	Johannesburg	-26.1	28.1	~1957-1991	1
+1.1	+0.13	Mundaring	-32.0	116.2	~1957-1991	1
	-0.46 to +0.03	Grahamstown	-33.3	26.5	1973-2000	11
	+0.01	Canberra	-35.3	149.0	~1957-1991	1
	-0.03	Hobart	-42.9	147.3	~1957-1991	1

Table 3.4. Observed trends in hmF2 and foF2 from 1957 to 1997 at a number of stations. All stations are ordered by geographic latitude, but the first six stations, in the American-Atlantic sector (-100 to -10 longitude), are separately ordered, which will prove helpful in chapter 7. Latitudes are positive north; negative south, and longitudes positive east; negative west. References are: 1 – Upadhyay and Mahajan (1998), 2 – Foppiano et al. (1999), 3 – Jarvis et al. (1998), 4 – Elias and De Adler (2006), 5 – Ulich and Turunen (1997), 6 – Givishvili et al. (1995), 7 – Bremer (1992), 8 – Laštovička et al. (2006), 9 – Xu et al. (2004), 10 – Sharma et al. (1999), 11 – Poole and Poole (2002).

3.3 Possible causes of observed trends

3.3.1 Changes in CO₂ concentration

Several hypotheses on the causes of long-term trends have been formulated, the most common being an increase in greenhouse gas concentrations, most importantly CO₂. The CO₂ concentration in the Earth's atmosphere has increased since the industrial revolution from ~280 to 377 ppm in 2004 as measured at ground level in Mauna Loa, Hawaii (Prentice et al., 2001; Keeling and Whorf, 2005). Although in the troposphere an increase in the CO₂ concentration has a warming effect, in the middle and upper atmosphere CO₂ is an important coolant, and therefore the observed increase in its concentration should result in cooling.

CO₂ cools the upper atmosphere by emitting 15 μm radiation mostly to space, when relaxing from its vibrational v₂ state, after being excited to this state by collisions with N₂, O₂, and, most importantly, atomic O. This way kinetic energy is removed from the ambient atmosphere, which results in cooling, overcoming the extra heating related to extra absorption of radiation coming from a warmer troposphere. The efficiency of the process depends mainly on the atomic oxygen

concentration and the CO₂-O excitation rate, though by convention the de-excitation rate coefficient is normally quoted (which is related to the excitation rate coefficient; see e.g. Sharma and Roble, 2002), often simply referred to as the CO₂-O rate coefficient.

Increased cooling due to increased CO₂ concentrations can cause not only long-term trends in temperature, but also causes a contraction of the atmosphere, which leads to a decrease of the density in the thermosphere at fixed heights and the lowering of ionospheric layers (see Rishbeth, 1990; Rishbeth and Roble, 1992). Possibly, these changes could also lead to long-term changes in global circulation (Roble and Dickinson, 1989). Little change in maximum electron density and critical frequency is expected as a result of atmospheric contraction (Rishbeth, 1990).

3.3.2 Changes in the concentration of other atmospheric constituents

The ozone concentration in the stratosphere has decreased markedly since ~1980 (Solomon, 1999, and references therein). Since ozone absorbs solar UV radiation, contributing significantly to the total heating in the stratosphere, a decrease in its concentration will cause cooling.

The concentration of water vapour in the stratosphere has increased from the mid-1950s to 2000 (Rosenlof et al., 2001), and since water vapour is again a radiative cooler, as CO₂, this should also lead to cooling. Changes in ozone and water vapour concentration may thus have added to any cooling effects that are usually attributed to changes in CO₂ concentration.

3.3.3 Changes in solar and geomagnetic activity

Since the atmosphere, and especially the ionosphere-thermosphere system, responds strongly to changes in geomagnetic and solar activity, any long-term changes in these could cause a long-term trend in atmospheric parameters. Clilverd et al. (1998) reported that the geomagnetic storm activity has increased over the past century, and some studies have argued that this can explain the observed long-term changes in foF₂, though not those in hmF₂ or other parameters (Mikhailov, 2006).

Laštovička (2005) summarized possible effects of long-term variations in both solar and geomagnetic activity on long-term trends in general. His main conclusions were that the influence of solar and geomagnetic activity on observed

long-term trends decreases with decreasing altitude, and that this also decreased from the beginning of the 20th century towards its end.

3.3.4 Changes in the Earth's magnetic field

Since the ionosphere consists of charged particles, it may be expected to respond to changes in the Earth's magnetic field. This could be caused by changes in the position of the magnetic poles, affecting high latitude convection patterns within the ionosphere and preferred particle precipitation zones, or by a change in the interaction between neutral winds, which drag ions and electrons along, and the magnetic field, which also influences the motions of charged particles. This possibility has received relatively little attention, but will be further investigated in chapter 7.

3.4 Modelled long-term trends

Once hypotheses for the causes of long-term trends have been formulated, these can be tested by means of model simulations. In particular the effect of increased greenhouse gas concentrations on the middle and upper atmosphere (mainly on the temperature) has been modelled many times, and more recently also changes in other atmospheric constituents have received some attention. An overview of modelled trends due to these mechanisms is given below.

3.4.1 Temperature

The quantitative effect of changes in the CO₂ concentration – typically a doubling – on the temperature has been studied with various middle and upper atmospheric models by e.g. Fels et al. (1980), Roble and Dickinson (1989), Berger and Dameris (1993), Portmann et al. (1995), Akmaev and Fomichev (1998), and Jonsson et al. (2004). An overview of a few relevant characteristics and settings of the models used in the studies cited above is presented in table 3.5, and table 3.6 presents the main findings sorted by altitude region.

Models agree quite well in the stratosphere, where they predict a global cooling of 4-8 K, maximizing at the stratopause (~50 km) at 10 to 15 K. In the mesosphere there is a wider range from 8 to 18 K cooling, and in the thermosphere models show even less agreement, with for instance cooling at 150

km estimated at 12 K by Roble and Dickinson (1989) and 30 K by Akmaev and Fomichev (1998).

<i>Reference</i>	<i>CO₂ cooling scheme</i>	<i>CO₂-O rate coeff.</i>	<i>G.W. scheme</i>	<i>Base level</i>
Fels et al. (1980)	No non-LTE	-	-	330
Roble and Dickinson (1989)	Dickinson (1984)	$1 \cdot 10^{-12}$	-	330
Berger and Dameris (1993)	Berger and Dameris (1993) + Fomichev et al. (1993)	$2 \cdot 10^{-13}$	-	330
Portmann et al. (1995)	Portmann (1994)	unknown	Lindzen (1981)	330?
Akmaev and Fomichev (1998)	Fomichev et al. (1998)	$3 \cdot 10^{-12}$	Gavrilov (1990)	360
Jonsson et al. (2004)	Fomichev and Blanchet (1995)	unknown	Hines (1997)	360
CMAT2	Fomichev et al. (1998)	$3.5 \cdot 10^{-12}$	optional	optional

Table 3.5. Overview of model characteristics and settings used in previous studies, and those of CMAT2 as used in this study. The CO₂-O relaxation rate coefficient is given in cm⁻³·s⁻¹ and the base level (of the CO₂ concentration) in ppm.

<i>ΔT (K)</i>	<i>Altitude (km)</i>	<i>Reference</i>
-2	20	Fels et al. (1980)
-2 to -4	20	Berger and Dameris (1993)
-4	25	Portmann et al. (1995), Jonsson et al. (2004)
-7	30	Akmaev and Fomichev (1998)
-8	35	Fels et al. (1980)
-8	40	Portmann et al. (1995)
-10	50	Fels et al. (1980)
-10 to -12	50	Jonsson et al. (2004)
-10 to -15	50	Berger and Dameris (1993)
-14	50	Akmaev and Fomichev (1998)
-8	60	Jonsson et al. (2004)
-18	60	Akmaev and Fomichev (1998)
-8	70	Fels et al. (1980)
-5 to -10	80	Berger and Dameris (1993)
-8	80	Portmann et al. (1995)
-14	80	Akmaev and Fomichev (1998)
0	100	Akmaev and Fomichev (1998)
-9	100	Roble and Dickinson (1989)
-13	100	Portmann et al. (1995)
+12	110	Akmaev and Fomichev (1998)
-40 to -50	110	Berger and Dameris (1993)
0 to -5	140	Berger and Dameris (1993)
-12	150	Roble and Dickinson (1989)
-30	150	Akmaev and Fomichev (1998)

ΔT (K)	Altitude (km)	Reference
-50	180	Akmaev and Fomichev (1998)
-35	200	Roble and Dickinson (1989)
-51	300	Roble and Dickinson (1989)

Table 3.6. Overview of modelled temperature responses found for a doubling of the CO₂ concentration throughout the middle and upper atmosphere, sorted by altitude region.

All studies mentioned above were assuming a doubling of the CO₂ concentration, while the CO₂ concentration has changed much less than that over the past few decades. Most observed trends discussed in section 3.2 were based on data from ~1965-1995. In this time window the CO₂ concentration increased only from ~320 to ~360 ppm (Keeling and Whorf, 2005). Since it is not clear how the effects of a doubling of the CO₂ concentration relate to the actual change as observed over a few decades, Akmaev and Fomichev (2000) studied the effects of the change in CO₂ concentration from 1955 to 1995. Their results are summarized in table 3.7. Akmaev and Fomichev (2000) note that the vertical structure of their modelled response is roughly in agreement with observations, but that its magnitude is much smaller. The response of a doubling of the CO₂ concentration was in fact much closer to observed temperature trends.

Altitude (km)	ΔT (K·decade ⁻¹)		Total ΔT (K)	
	January	April	January	April
30	-0.3	-0.3	-1.0	-1.0
55-70	-0.8	-0.8	-3.0	-3.0
85	-0.5	-0.5	-1.8	-1.8
95	-0.6	-0.8	-2.2	-3.0
120	0.0	-0.5	0.0	-2.0
180	-3.0	-2.3	-12.1	-9.3

Table 3.7. Temperature trends in K·decade⁻¹ for January and April as modelled by Akmaev and Fomichev (2000) derived from the difference between their simulations with 1955 and 1995 CO₂ levels (total ΔT).

Bremer and Berger (2002) also studied the additional effects of changes in ozone concentration as occurred from 1979 to 1998 and Akmaev et al. (2006) studied the additional effects of both changes in ozone and water vapour content from 1980 to 2000. Both studies found that changes in ozone concentration

caused additional cooling in the middle atmosphere, of comparable magnitude to the CO₂ induced cooling, but Akmaev et al. (2006) found it caused less cooling in the thermosphere. Akmaev et al. (2006) further found that changes in water vapour concentration slightly enhanced these effects.

3.4.2 Density

Roble and Dickinson (1989) were the first to model the effect of changes in greenhouse gas concentration on the density, and found that a doubling of the CO₂ and CH₄ concentration would lead to a decrease of about 40% of the O and 60% of the O₂ and N₂ number densities at 300 km.

Akmaev et al. (2006) modelled the effect of actual changes in CO₂, ozone and water vapour concentration for 1980-2000 on global mean and zonal mean density from 30 to 200 km. They found an increasingly strong decrease in density with height up to 100-110 km, reaching a maximum of 5-7% per decade. At higher altitudes this stabilized at 3.5-4% per decade. The changes in CO₂ and ozone concentration were responsible for most of the trend, with a smaller contribution from the change in water vapour concentration.

3.4.3 Winds

Rishbeth and Roble (1992) showed that zonal winds at 100-300 km change by at most 6 ms⁻¹ in response to a doubling of the CO₂ and CH₄ concentration, and reported that changes in meridional wind were also rather small. Rind et al. (1990) modelled the response to a doubling of the CO₂ concentration at 0-85 km, and found a 10-20% increase in the residual circulation.

Jacobi et al. (2003) modelled the effects on the neutral wind of a 10% increase in CO₂ concentration and a change in ozone concentration of up to 10% at high latitudes, roughly reflecting changes as occurred from ~1970-2000. They found that the meridional winds at mid-latitudes in the mesopause region decreased by up to 2 ms⁻¹. Other studies that modelled the effects of actual changes in CO₂ concentration and/or other constituents (Akmaev and Fomichev, 2000; Bremer and Berger, 2002; Akmaev et al., 2006) did not show changes in zonal or meridional winds.

3.4.4 Ionospheric parameters hmF2 and foF2

Rishbeth and Roble (1992) found a lowering of hmF2 of on average 10-15 km and a small decrease in foF2 (< 0.5 MHz) in response to a doubling of the CO₂ and CH₄ concentrations. The response was somewhat stronger at solar minimum conditions than at solar maximum conditions. Studies concerned with actual changes in CO₂ concentration and/or other constituents did not study effects on hmF2 and foF2.

3.5 Discussion and conclusions

In general, we find that model simulations of changes in CO₂ concentration predict smaller temperature trends than are observed in the middle atmosphere, but larger density trends than are observed in the thermosphere. When changes in ozone concentration are also taken into account, modelling results are in better agreement with observations. However, they still only explain observed middle atmospheric temperature trends for $\sim 50-70\%$, and give nearly twice as large trends in thermospheric density than are observed (at 200 km). Trends in winds in the mesopause region and trends in hmF2 and foF2 vary with location, but seem generally also larger than predicted by modelling studies of changes in CO₂ concentration or changes in CO₂ and ozone concentration combined.

There are several possible explanations for these discrepancies. First of all, many observations do not have global coverage. Most observational stations are located in the northern hemisphere and on land. Still, observed trends are often considered as representative of a wide latitude band or region, and results of several stations combined are then easily extrapolated to the entire globe. This is not necessarily correct, as some trends may be local or regional features. Also, it must be kept in mind that trends often vary with season and local time, and trends reported in the literature are sometimes derived for a particular season or local time, while others are averaged.

Second, any measurement is subject to inaccuracies, and over periods of decades, measurement techniques and instruments, as well as the subsequent processing of data usually change. Very careful consistency checks must therefore be made to ensure that all data can be combined into one data set to obtain a long-term trend. Further, it has proven difficult to remove in particular solar cycle effects completely (e.g. Clilverd et al., 2003). For all these reasons, observed trends can have relatively large errors associated with them, which are not always calculated and provided correctly along with the obtained trends themselves.

Similar arguments hold for modelling results. Models are by definition a simplification of reality and rely on various assumptions and approximations. Also modelling results have therefore errors associated with them, which are often ignored or only discussed loosely. Part of the disagreement between observations and modelling results may therefore be explained by inaccuracies in both.

However, the differences between modelling results and observations are rather large, and seem to be reproduced with many models. This suggests that other processes than changes in CO₂, ozone and water vapour concentration, which are the only processes investigated by modelling studies so far, may have contributed to long-term trends as well.

4. Model descriptions

In this thesis, the Coupled Middle Atmosphere and Thermosphere model version 2 (CMAT2) is used to study the effects of changes in CO₂ and/or ozone concentration on the middle and upper atmosphere. Most models are limited to either the middle atmosphere or thermosphere only, while there is coupling between these regions in reality. With CMAT2 it is possible to study this coupled system. Since CMAT2 is a new model, we will provide a description and some validation results in the following sections.

The effects of changes in the Earth's magnetic field will also be studied, but the National Center for Atmospheric Research (NCAR) Thermosphere-Ionosphere-Electrodynamics General Circulation Model (TIE-GCM) is used to do this. This model is better suited than CMAT2 to study the combined action of neutral winds and the Earth's magnetic field on the ionosphere, which will prove essential for our purposes. Since TIE-GCM is a well established model it will only be described briefly in this chapter.

4.1 CMAT2 model description and settings

The Coupled Middle Atmosphere and Thermosphere model version 2 (CMAT2) is a substantially updated version of its predecessor CMAT, which is described by Harris (2001), Harris et al. (2002), Dobbin (2005), England et al. (2006) and Dobbin et al. (2006). CMAT is an extension of the Coupled Thermosphere Ionosphere Plasmasphere (CTIP) model (see Fuller-Rowell and Rees, 1980; Millward et al., 1996) to include also the middle atmosphere.

The model solves the primitive non-linear coupled equations of energy, momentum and continuity on a flexible grid, here set at 91 latitude points, 20 longitude points, and 63 pressure levels with a separation of 1/3 scale height for levels 1-59 and a separation of one scale height for levels 60-63. The lower boundary was set to a pressure level of 100 mbar, corresponding to an altitude of ~15 km, and the upper boundary to a level of 7.587 pbar, corresponding to an altitude of ~300-600 km (depending on geophysical conditions). The model thus covers the stratosphere, mesosphere and thermosphere, including the major energetic and dynamical processes within those regions

For the present studies, composition was determined using the following climatologies: (i) The empirical Mass Spectrometer and Incoherent Scatter Extended (MSISE-90) model (Hedin, 1991) for O, O₂, and N₂; (ii) The UK Universities Global Atmospheric Modelling Programme (UGAMP) ozone climatology

(Li and Shine, 1995) for O₃; (iii) The Student Nitric Oxide Explorer satellite Empirical Model (SNOEM; Marsh et al., 2004) for NO. The O, O₂, N₂ and O₃ climatologies are defined in constant pressure; the NO climatology in constant height. The CO₂ concentration was set at a constant mixing ratio below the turbopause, and decayed above in accordance with diffusive equilibrium. The turbopause is defined in CMAT2 as the point where the molecular and turbulent viscosity coefficients become equal. Solar fluxes and absorption cross-sections were taken from the SOLAR 2000 model (Tobiska et al., 2000). Ionospheric electron density was taken from a simple parameterization based on Chiu (1975).

It should be noted that by using a fixed climatological composition, any chemical feedback due to a changed CO₂ and/or ozone concentration is not represented self-consistently. However using a climatological composition does allow for sensitivity tests where individual species are varied whilst holding other species constant. This is useful in studying the relative contribution of observed trends in atmospheric species on global cooling.

Cooling due to CO₂ 15 μm infrared emission is incorporated in CMAT2 on the basis of the parameterization scheme of Fomichev et al. (1998), valid for a concentration range of 150 to 720 ppm. The CO₂-O de-excitation rate coefficient was set at $3.5 \cdot 10^{-12} \text{ cm}^{-3} \text{ s}^{-1}$, following Sharma and Wintersteiner (1990), and slightly different from Shved et al. (1998). The atomic oxygen deactivation rate coefficient for the 9.6 μm NO emission was set at $2.4 \cdot 10^{-11} \text{ cm}^{-3} \text{ s}^{-1}$ (Dodd et al., 1999).

CMAT2 offers three options to include the effects of gravity waves, which are all used in chapter 5. The first is simple Rayleigh friction, the second a hybrid Lindzen-Matsuno (HLM) parameterization scheme (Lindzen, 1981; Matsuno, 1982; Meyer, 1999), and the third a parameterization based on Medvedev and Klaassen (1995, 2003) and Medvedev et al. (1997), hereafter referred to as MK95. Rayleigh friction is often not considered a proper parameterization, but it may be referred to as such in the following for simplicity. The HLM and MK95 parameterizations were both used successfully in a CMAT study by England et al. (2006), who did a full comparison of the results with observations. The main principles behind the parameterizations are discussed further in section 4.2. The effects of planetary waves were not accounted for in the present studies.

For all simulations, the MSISE-90 model was used to provide the model with start-up data. After an initial spin-up time of 7 days, all simulations were run for 50 days to allow the model to reach a steady state, and this was done in perpetual mode (i.e. not advancing the day number), usually for two seasons (day 80 and day 172), and varying solar and geomagnetic activity levels.

4.2 Gravity wave parameterizations in CMAT2

4.2.1 Rayleigh friction

The simplest way to represent, to first order, the effect of gravity waves on the background winds is by Rayleigh friction. This assumes gravity waves cause a drag that is proportional to the background wind speed, so that:

$$\frac{d\mathbf{v}}{dt} = -k(z)\mathbf{v}, \quad (4.1)$$

where $k(z)$ = friction coefficient in s^{-1} (dependent on height). In CMAT2 $k(z)$ is calculated according to:

$$\begin{aligned} k(z) &= 3.0e^{(z-100)/27} && \text{for } 75 \leq z \leq 100, \\ k(z) &= k(z-1)e^{-3} && \text{for } z > 100, \\ k(z) &= k(75)e^{(z-75)/4} && \text{for } z < 75, \end{aligned} \quad (4.2)$$

where z = height in km.

By tuning the friction coefficient appropriately, it is possible to obtain more realistic wind and temperature patterns. However, since a drag always acts to decelerate the mean flow towards zero, it is not possible to reproduce a reversal of the winds in the upper mesosphere, as is observed (e.g. McLandress et al., 1996), and there is no physical concept behind Rayleigh drag. For these reasons it is a very limited and crude parameterization.

4.2.2 Hybrid Lindzen Matsuno scheme (HLM) scheme

The HLM parameterization is based on the work of Lindzen (1981), who described the concept of "linear saturation", and Matsuno (1982), who developed the so-called "wave transmission" concept. Linear saturation was briefly described in section 2.1.7. Matsuno (1982) described the momentum flux of gravity waves in terms of a transmissivity of the atmosphere, with total diffusion (molecular + eddy diffusion) acting as an absorber. The transmissivity goes to zero as the difference between the phase speed of the wave and the wind speed approaches zero or when the total diffusion of the atmosphere increases.

The combination of the linear saturation and wave transmission concepts into one parameterization was described by Meyer (1999), and the HLM scheme used in CMAT2 is based on that. The HLM scheme calculates a wave-induced acceleration acting to decelerate or accelerate the wind speed towards the phase speed of the wave, rather than slowing all winds down to zero, which is an improvement on Rayleigh friction. It also accounts for the turbulent diffusion of momentum and thermal energy by means of the (prescribed) eddy diffusion coefficient.

The eddy diffusion coefficient profile used in CMAT2 is based on the Global Scale Wave Model (Hagan et al., 1995), which was in turn based on Garcia and Solomon (1985). Molecular diffusion coefficients were taken from Colegrove (1966), Fuller et al. (1966), Banks and Kockarts (1973) and Levin et al. (1990).

A set of 19 waves, whose horizontal phase speeds range from -60 to $+60$ ms^{-1} , was used as input for HLM. Their amplitudes follow a Gaussian distribution, the amplitude of the wave with zero phase speed being 20 times larger than the amplitude of the waves with phase speeds of ± 60 ms^{-1} .

4.2.3 Medvedev-Klaassen (MK95) scheme

The MK95 scheme (Medvedev and Klaassen, 1995) assumes that non-linear wave-wave interaction processes cause gravity waves to break, which were ignored in the HLM scheme. Two types of wave-wave interaction, based on the "dissipation by nonlinear diffusion" theory of Weinstock (1982, 1990) and the Doppler spreading theory of Hines (1991), are included. Dissipation by nonlinear diffusion was briefly described in section 2.1.7. Hines (1991) argued that the highest wavenumber waves (say of wavenumber m_c) in a gravity wave spectrum must interact with the root-mean-squared (rms) wave-induced winds when these become comparable to the smallest horizontal phase speed (which will happen as amplitudes increase with height). This would lead to the production of waves with a still higher wavenumber ($> m_c$) and attenuation of the spectral intensity just below m_c .

In the MK95 scheme the Doppler spreading theory was adjusted such that only waves with frequencies lower than that of the wave itself were considered to contribute to the rms wave-induced winds, unlike in other implementations of the Doppler spreading theory (e.g. Hines, 1997). MK95 further differs from HLM and Rayleigh friction by accounting also for heating associated with gravity wave dissipation (Medvedev and Klaassen, 2003).

The input spectrum used in the present studies is an isotropic spectrum of 60 waves, with 15 frequencies in each of the four cardinal directions with vertical wavelengths ranging from 900 m to 19 km. The power spectral density of each source wave $S(m)$ is given by:

$$S(m) = S_0 \frac{(m / m_*)}{1 + (m / m_*)^4}, \quad (4.3)$$

where S_0 = average amplitude of the spectrum,

m = vertical wavenumber of each wave,

m_* = characteristic wavenumber (associated with a “knee” in the generally accepted shape of the spectral gravity wave distribution).

Here, m_* is set to 0.006 m^{-1} and S_0 to $100 \text{ m}^3\text{s}^{-2}$, following Medvedev et al. (1997) and Medvedev and Klaassen (2000). The same eddy diffusion coefficient profile is used as for the other gravity wave schemes.

4.3 CMAT2 model validation

4.3.1 Temperature

Figures 4.1 and 4.2 show the global and zonal mean temperature profiles, respectively, as modelled by CMAT2 with each of the three gravity wave schemes. Also shown in figure 4.1 is the MSISE-90 empirical profile.

The modelled temperature profiles agree well with MSISE-90 in the middle atmosphere, but underestimate the temperature in the thermosphere. This is a known discrepancy, to which many different factors may contribute, such as uncertainties in the EUV flux, absorption cross-sections, neutral heating efficiency, molecular diffusion coefficients, and perhaps most importantly, in the high-latitude electric field strength (Harris, 2001). Also, the fact that MSISE-90 is mostly based on data from the 1970s and 1980s, and even includes some data from the 1950s and 1960s (Hedin, 1991), when the CO_2 concentration was lower than 360 ppm, may contribute to the discrepancy in the thermosphere. Further we note that the modelled mesopause is ~ 10 km higher and ~ 10 K colder than observed (compare e.g. to Xu et al., 2007).

However, for the present studies we are mainly interested in the differences between simulations. In this case, the absolute temperature in the thermosphere and mesopause, as well as the height of the mesopause, will make a difference only if the differences in themselves depend on the state of the atmosphere in the two cases that are being compared. This may be the case, but should be a secondary effect. Further, we will perform simulations with a range of geophysical conditions, which will all lead to different thermospheric temperatures, so that we may assess how sensitive the results obtained are to the conditions that are chosen (and the thermospheric temperatures associated with them).

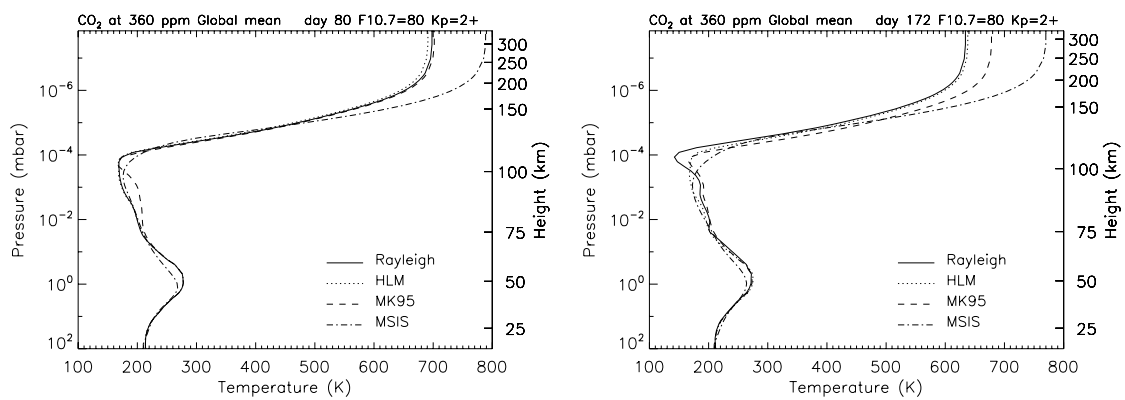


Figure 4.1. Global mean temperature (K) profiles for CMAT2 control runs with each of the three gravity wave schemes and MSISE-90 at day 80 (left) and day 172 (right) with $F_{10.7} = 80$ sfu and $K_p = 2+$.

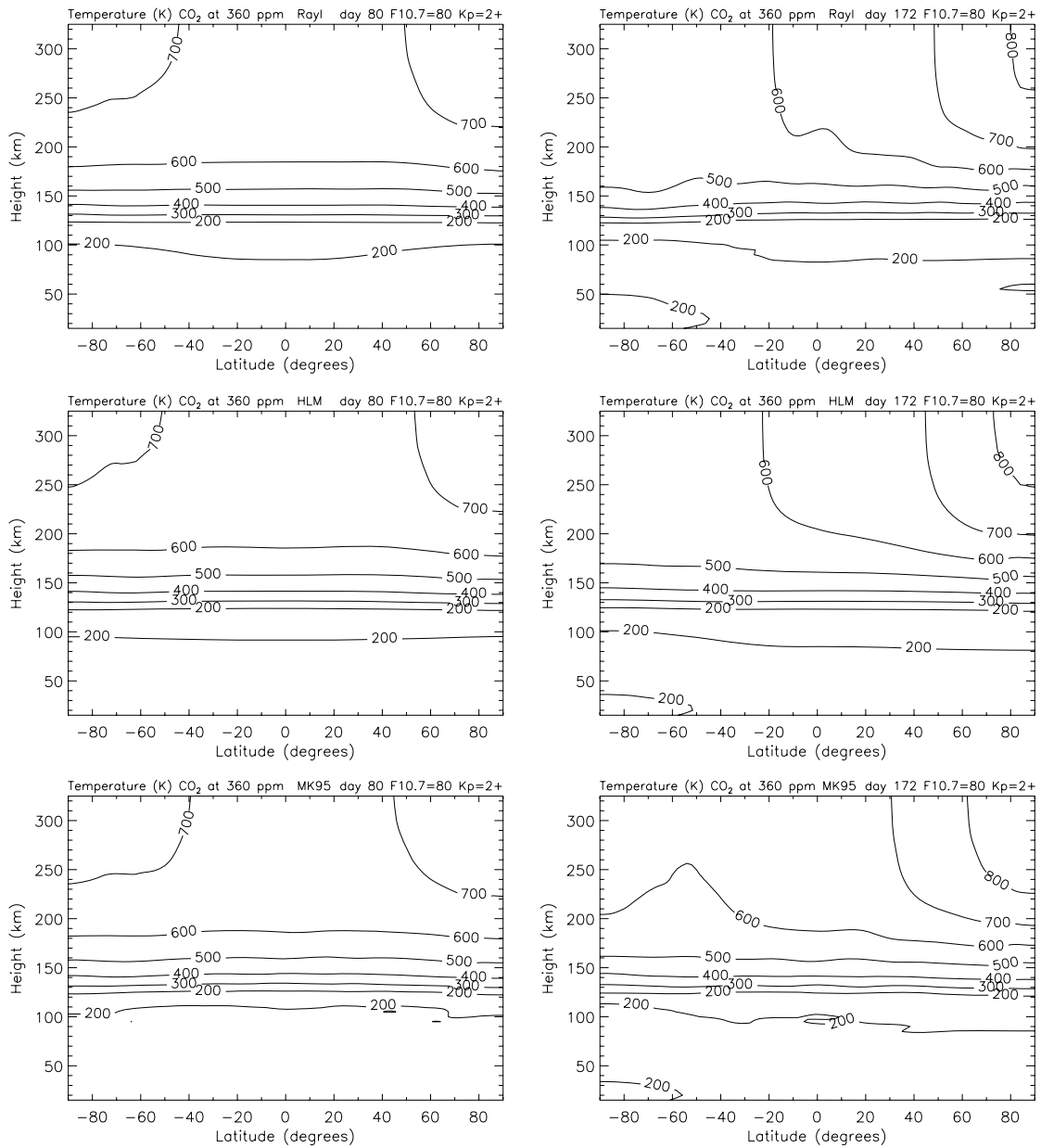


Figure 4.2. Zonal mean temperature (K) profiles for CMAT2 control runs with each of the three gravity wave schemes at day 80 (left) and day 172 (right) with $F_{10.7} = 80$ sfu and $K_p = 2+$.

4.3.2 Density

The global mean density profiles for the three gravity wave schemes and MSISE-90 are shown in figure 4.3. This has been plotted in a constant height reference frame rather than a constant pressure reference frame, because the differences are more easily seen this way.

MSISE-90 has a lower density in the mesosphere and lower thermosphere than any of the model results, but a higher density in the upper thermosphere. MK95 is closest to MSISE-90 in the upper thermosphere, but in the mesosphere and lower thermosphere HLM and Rayleigh friction are closer.

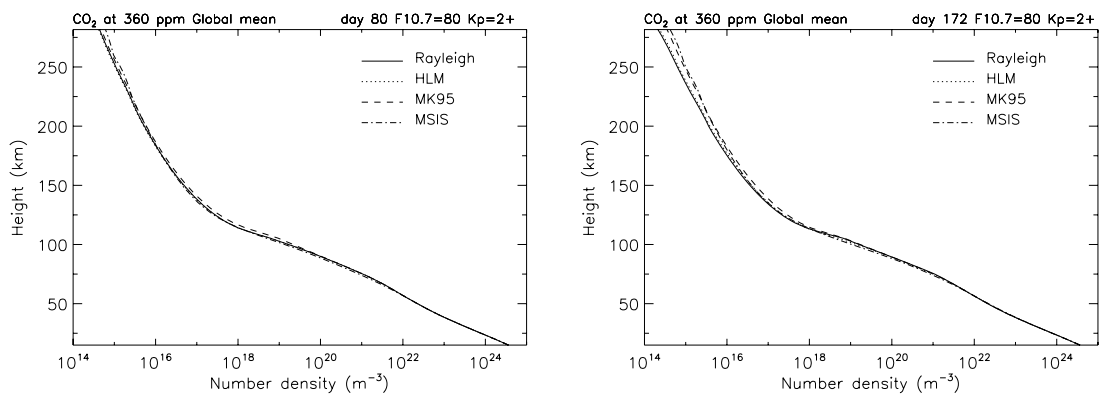


Figure 4.3. Global mean density (m^{-3}) profiles for CMAT2 control runs with each of the three gravity wave schemes and MSISE-90 at day 80 (left) and day 172 (right) with $F_{10.7} = 80$ sfu and $K_p = 2+$.

4.3.3 Winds

Figures 4.4 and 4.5 show the zonal mean meridional and zonal wind, respectively, for the control runs with each of the gravity wave schemes. These are compared with the zonal mean winds from the empirical HWM-93 model (Hedin et al., 1996), shown in figures 4.6 and 4.7.

We assume that our results for day 80 are comparable to mid-April and those for day 172 to mid-July, though there is a difference of ~ 3 weeks in day number. Further, HWM-93 winds are not only longitudinally, but also diurnally averaged, while our results are a longitudinal average only, at 0 UT. We also note that the HWM-93 winds go up to only 120 km altitude and that meridional winds are considered positive northward, while in CMAT2 results positive winds are southward. Zonal winds are in both cases positive eastward.

The modelled meridional winds agree well with HWM until ~ 90 km, as only very weak winds ($< 5 \text{ ms}^{-1}$) are present for both days. At higher altitudes at day 80, the HWM winds are stronger than the modelled winds, except perhaps when MK95 is used, though the wind pattern for MK95 appears very noisy and is for that reason probably not realistic. From 130-150 km the Rayleigh and MK95 schemes

do show a similar wind pattern as seen in HWM at 90-120 km (southward winds in the southern hemisphere and northward winds in the northern hemisphere), so possibly this pattern is appearing too high in the modelling results. It does not appear at all when HLM is used.

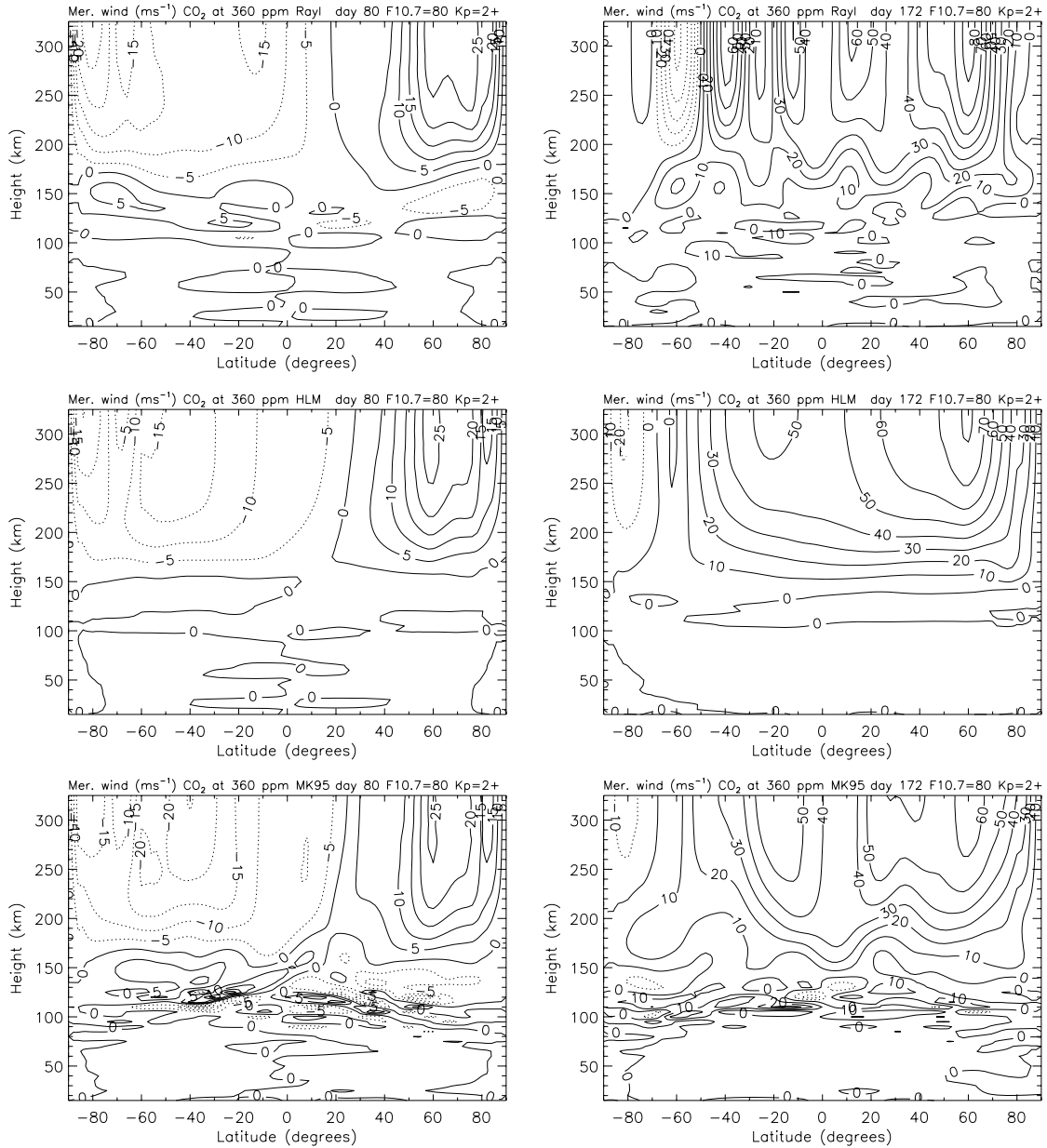


Figure 4.4. Zonal mean meridional wind (ms^{-1}) profiles for CMAT2 control runs with each of the three gravity wave schemes at day 80 (left) and day 172 (right) with $F10.7 = 80$ sfu and $Kp = 2+$. Southward winds are positive (solid); northward winds are negative (dashed).

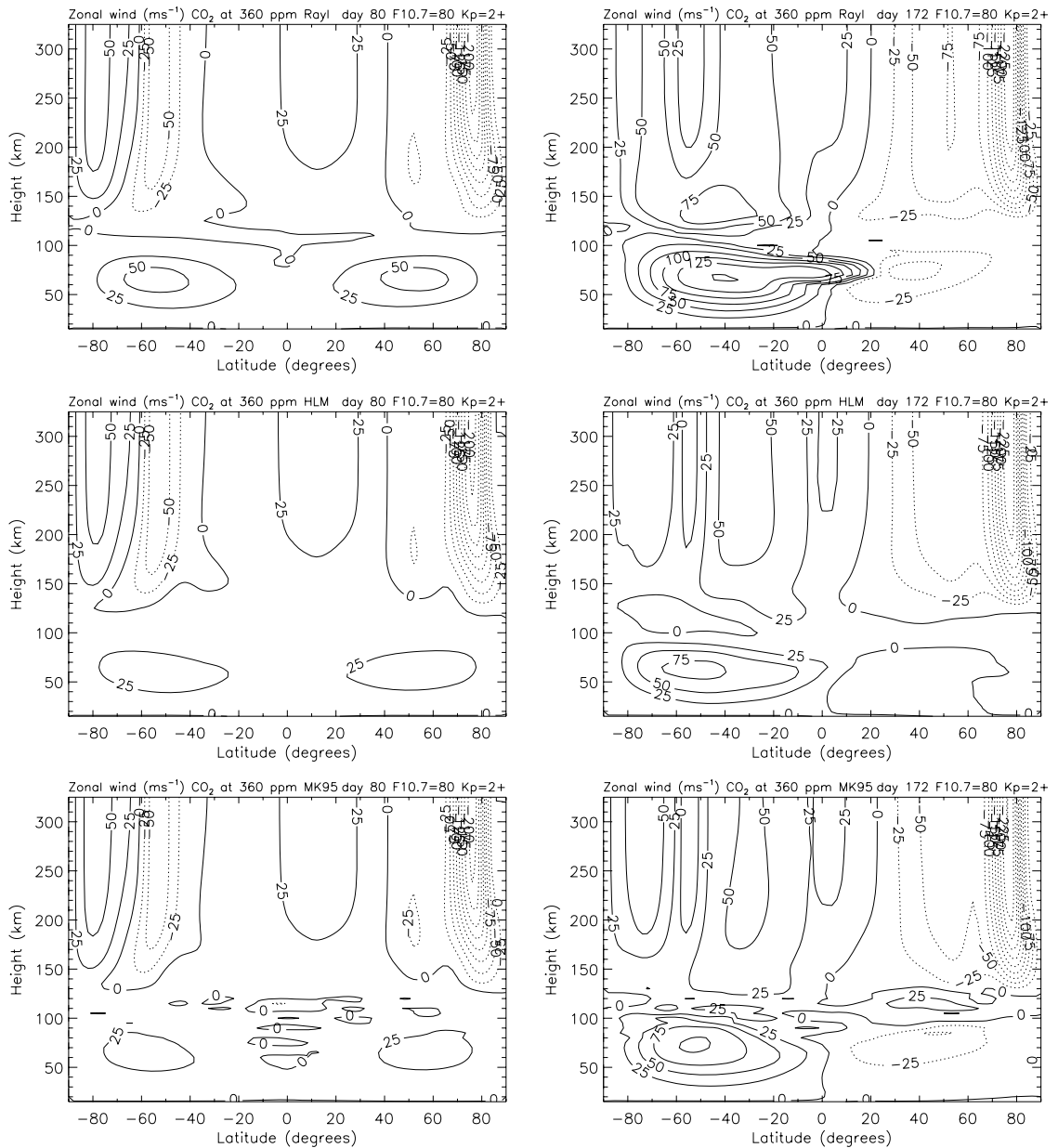


Figure 4.5. Zonal mean zonal wind (ms^{-1}) profile for CMAT2 control runs with each of the three gravity wave schemes at day 80 (left) and day 172 (right) with $F10.7 = 80$ sfu and $Kp = 2+$. Eastward winds are positive (solid); westward winds are negative (dashed).

At day 172, HWM winds are again stronger above 90 km when HLM is used, but comparable in order of magnitude to modelled winds for Rayleigh and MK95. However, the directions of the modelled winds and HWM winds do not match.

At day 80, the modelled zonal winds show two eastward jets in the mesosphere centred around $55\text{-}60^\circ$ latitude, which are weakest for MK95, at $\sim 25 \text{ ms}^{-1}$, slightly stronger for HLM, and strongest for Rayleigh (up to 50 ms^{-1}), and are

of similar size and magnitude in both hemispheres for all gravity wave schemes. HWM also shows these jets, but the winds in the southern hemisphere are much stronger (up to 50 ms^{-1}) than those in the northern hemisphere (up to 10 ms^{-1}). This is probably because the HWM winds are for mid-April, and the modelling results are for day 80 (21 March). HWM also shows eastward winds at 70-80 km near the equator, which are not reproduced by the model.

At day 172, the modelling results show a strong eastward jet in the southern hemisphere (up to 150, 75, and 80 ms^{-1} for Rayleigh, HLM and MK95, respectively), while the westward jet in the northern hemisphere is weaker (up to 50 ms^{-1} for Rayleigh and MK95, non-existent for HLM). In HWM the eastward jet in the southern hemisphere maximizes at 70 ms^{-1} , while the westward jet in the northern hemisphere peaks at 60 ms^{-1} . This is likely to be again due to the mismatch in day number between the modelling results and HWM.

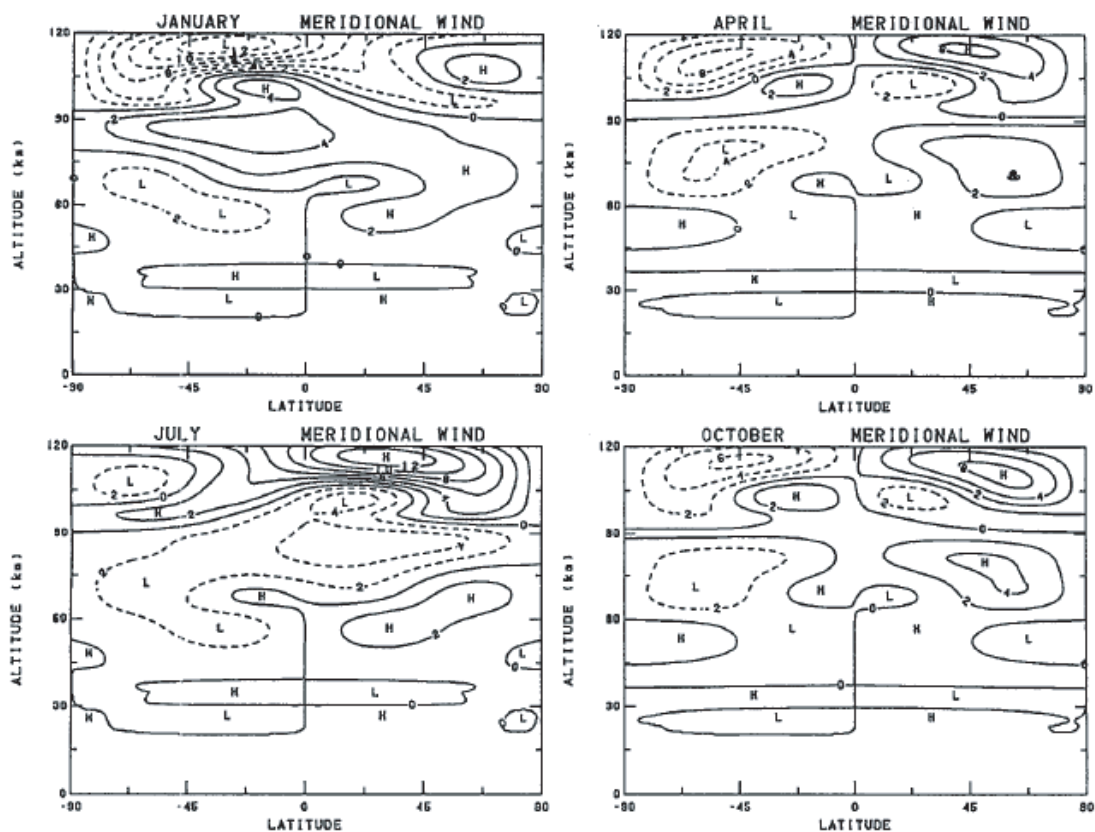


Figure 4.6. Zonal and diurnal mean meridional wind profiles from HWM-93 (Hedin et al., 1996) for four indicated months (mid-month). Northward winds are positive (solid); southward winds are negative (dashed).

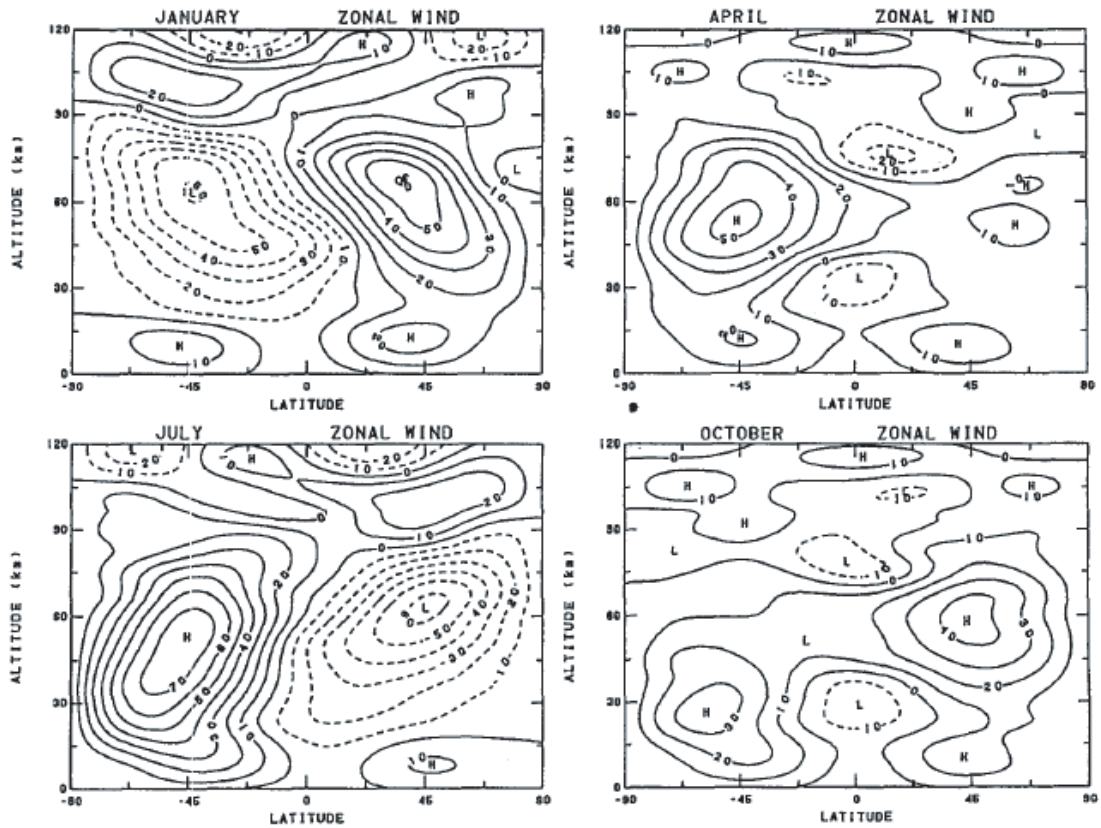


Figure 4.7. Zonal and diurnal mean zonal wind profiles from HWM-93 (Hedin et al., 1996) for four indicated months (mid-month). Eastward winds are positive (solid); westward winds are negative (dashed).

4.3.4 Ionospheric parameters

Table 4.1 gives the global mean hmF2 as calculated by CMAT2 for all three gravity wave schemes, as well as the global mean values from the empirical International Reference Ionosphere 2000 (IRI; Bilitza, 2001), all for low solar activity ($F_{10.7} = 80$ sfu or sunspot number = 22). Unfortunately it is not possible to produce a latitude-longitude map of hmF2 from CMAT2 results, because CMAT2 does not always go up high enough to capture the peak of the F2 layer during night time. A more recent version of CMAT2, which includes the Global Ionosphere-Plasmasphere (GIP) model (G.H. Millward, private communication, 2007), does cover higher altitudes, but is still under development.

For the calculation of the global mean hmF2 presented here, those grid points for which no peak was found below 300 km were excluded. We therefore get a lower average F2 layer peak than given by IRI, which is more representative of the daytime. However, rather than absolute hmF2 values, we will be studying

differences in hmF2 due to changes in CO₂ and/or ozone concentration, which have been shown to be fairly uniform over the globe, without an obvious local time dependence (Rishbeth and Roble, 1992). Therefore it is reasonable to assume that the global mean differences that are calculated in following chapters, based mostly on daytime values, are still representative of the F2 layer as a whole.

The global mean foF2 values as calculated by CMAT2 and foF2 values from IRI are given in table 4.2. All foF2 values are higher than the global mean IRI values. This is both because the Chiu (1975) model is used within our simulations, which gives higher peak electron densities than the IRI model, and because our global means are biased towards the daytime, when foF2 is larger. Again though, this should not be a major problem for the present studies, since we will be studying differences in foF2 only.

<i>hmF2</i>	<i>Rayleigh</i>	<i>HLM</i>	<i>MK95</i>	<i>IRI</i>
day 80	254.172	253.715	254.857	292.1
day 172	237.332	238.426	244.366	279.2

Table 4.1. Global mean hmF2 (km) given by IRI and for CMAT2 control runs with each of the three gravity wave schemes at day 80 and day 172 with F10.7 = 80 sfu and Kp = 2+.

<i>foF2</i>	<i>Rayleigh</i>	<i>HLM</i>	<i>MK95</i>	<i>IRI</i>
day 80	6.63006	6.66227	6.5648	5.69
day 172	5.38153	5.39173	5.31389	4.76

Table 4.2. Global mean foF2 (MHz) given by IRI and for CMAT2 control runs with each of the three gravity wave schemes at day 80 and day 172 with F10.7 = 80 sfu and Kp = 2+.

4.4 TIE-GCM

TIE-GCM was developed by Richmond et al. (1992) as part of a series of thermosphere/ionosphere models that were developed over the years at NCAR (Dickinson et al., 1984; Roble et al., 1988). While its predecessor, the Thermosphere-Ionosphere general circulation model (TIGCM), only described the dynamics, thermodynamics, radiation and photochemistry, TIE-GCM includes in addition a description of the interactions between the dynamics of the

thermosphere and the electric fields and currents of the ionosphere, which are collectively called electrodynamic. This includes for instance the generation of dynamo electric fields, as neutral winds drag charged particles across the geomagnetic field, while at the same time the motion of charged particles and the electrical conductivity are influenced by those fields. Also, the neutral winds are affected by the motions of charged particles, as they exert a drag on the neutral particles.

TIE-GCM solves self-consistently for all electrodynamic interactions for field lines equatorward of $\pm 60^\circ$ geomagnetic latitude. Within the polar caps, defined as $\pm 75^\circ$ - 90° geomagnetic latitude, an electric potential distribution was externally imposed using the Heelis et al. (1982) model, and within the transition zone from $\pm 60^\circ$ - 75° geomagnetic latitude the calculated distribution was constrained to approach the specified distribution. The IGRF is used to define the Earth's magnetic field in the model, and for all studies presented in this thesis, a grid of 72 longitude points, 36 latitude points ($5^\circ \times 5^\circ$ resolution) and 29 pressure levels between 95 and 800 km was used.

TIE-GCM has been used by numerous thermospheric/ionospheric studies, and has been shown to reproduce the overall structure and behaviour of the system (e.g. Richmond et al., 1992). Figures 4.8-4.11, showing maps of both hmF2 and foF2 as calculated by the model and given by IRI, confirm this. Only at high latitudes, the hmF2 plots for TIE-GCM show some noise, probably related to the merging of the prescribed and calculated electric field potentials. Otherwise the patterns and magnitudes of hmF2 and foF2 given by IRI and calculated by TIE-GCM are in good agreement.

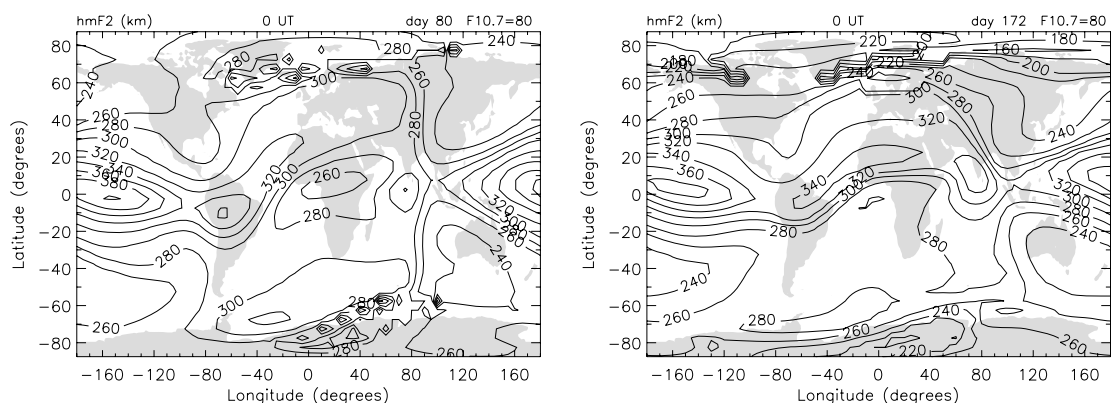


Figure 4.8. HmF2 (km) as modelled by TIE-GCM at day 80 (left) and at day 172 (right) at 0 UT with F10.7 = 80 sfu and quiet geomagnetic conditions.

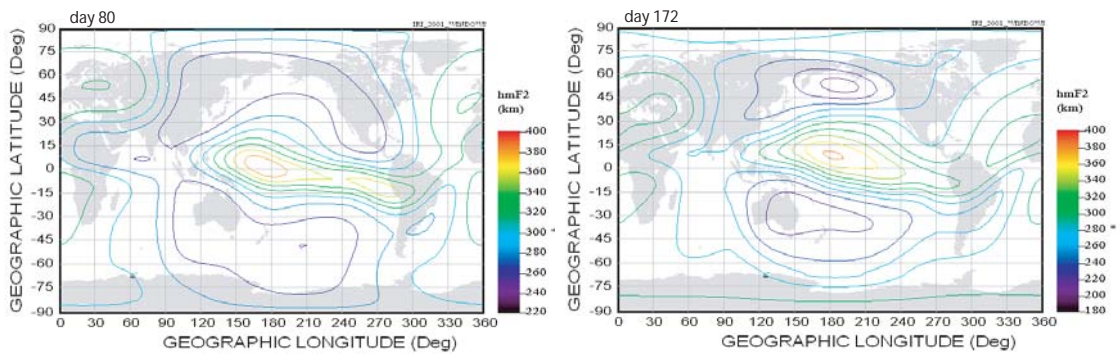


Figure 4.9. IRI map of hmF2 (km) at day 80 (left) and day 172 (right) at 0 UT for low solar activity ($F_{10.7} \approx 80$ sfu). Note that longitudes run from 0 to 360, so that there is a 180 degrees shift with respect to figure 4.8.

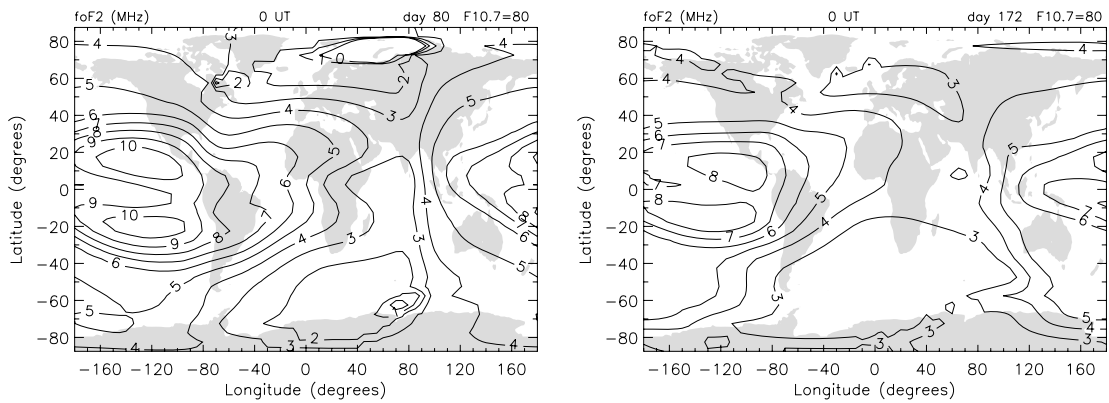


Figure 4.10. FoF2 (MHz) as calculated by TIE-GCM at day 80 (left) and at day 172 (right) at 0 UT with $F_{10.7} = 80$ sfu and quiet geomagnetic conditions.

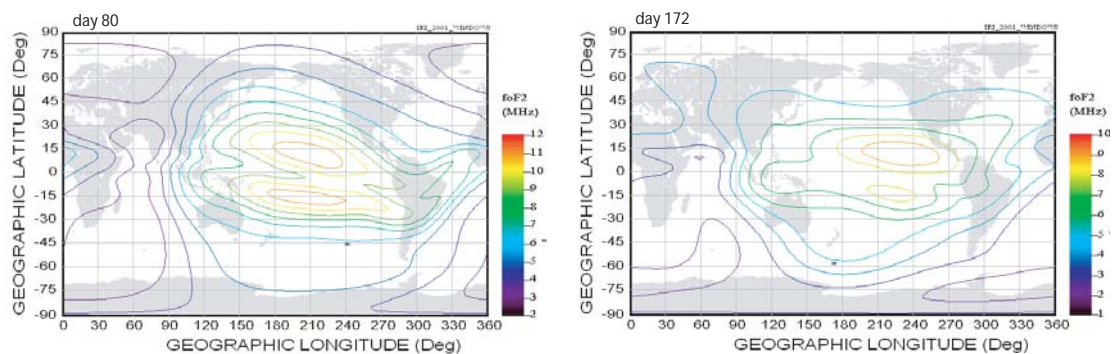


Figure 4.11. IRI map of foF2 (MHz) at day 80 (left) and day 172 (right) at 0 UT for low solar activity ($F_{10.7} \approx 80$ sfu). Note that longitudes run from 0 to 360, so that there is a 180 degrees shift with respect to figure 4.10.

4.5 Model data processing

To analyse the results of the various simulations, we calculate the (differences in) global mean parameter profiles, the parameter being e.g. temperature or density. All global means are calculated as the surface area weighted average of the parameter in question over all grid points at each given pressure level. When calculating the global mean hmF2 or foF2, we exclude data points for which no maximum in electron density can be found below 300 km.

Differences in global mean temperature profiles between simulations are mostly shown in constant pressure coordinates, as the model uses a pressure grid, rather than a height grid. As the atmosphere expands and contracts in response to temperature changes, the height corresponding to a certain pressure level changes, and therefore pressure levels can usually not be linked uniquely to heights when differences between simulations are shown. Any height labels that may be shown on the right vertical axis of a plot are therefore indicative only.

In some cases we choose to show (difference) plots in a constant height frame. This is done by first mapping all data onto a fixed height grid, using the heights corresponding to each pressure level as calculated by CMAT2 for each simulation. After that, differences between model simulations are calculated in the same way as for constant pressure coordinates.

4.6 Conclusions

There are some discrepancies between CMAT2 and empirical models. However, we have argued that these will not pose a major problem for the studies we are carrying out in the following chapters. In chapter 6 we show results obtained with all three gravity wave schemes. In other chapters we have chosen to use only HLM, which was chosen because it has a better physical basis than Rayleigh friction, does not result in a noisy wind pattern in the mesopause region as MK95 does, and is generally in reasonable agreement with observations.

TIE-GCM is able to reproduce global hmF2 and foF2 patterns well, and is better suited than CMAT2 to study the effects of secular variation of the Earth's magnetic field on the ionosphere, because it includes a self-consistent description of electrodynamic coupling mechanisms, while CMAT2 does not.

5. Modelled effects of changes in CO₂ and ozone concentration

5.1 Introduction

The effects of changes in CO₂ concentration have been modelled many times (see section 3.4). However, most studies were concerned with a doubling of the CO₂ concentration, while only a few modelled the actual changes that occurred over the period for which most observed trends have been derived (Akmaev and Fomichev, 2000; Bremer and Berger, 2002; Akmaev et al., 2006). Only Bremer and Berger (2002) and Akmaev et al. (2006) took also the effects of changes in ozone concentration into account. However, their models extended up to only 150 and 200 km, respectively, so that they could not study any effects on the ionospheric F2 layer, or on the neutral atmosphere above 200 km.

In this chapter, we study both the effects of changes in CO₂ concentration only, and the additional effects of changes in the ozone concentration on temperature, density and mean wind strength throughout the atmosphere from ~15 km up to ~300 km, as well as on the position and temperature of the mesopause, and the ionospheric parameters hmF2 and foF2. We will use CMAT2 model simulations for this, and where possible, results are compared against results from other modelling studies and observations. This contributes to the validation process of CMAT2, as well as the verification of results of previous studies, in particular regarding the additional effects of changes in ozone concentration on the middle atmosphere and lower thermosphere. In addition, we present some new results regarding the effects of the actual changes in CO₂ and ozone concentration on the thermosphere between 200 and 300 km and on the ionosphere.

Two different seasons will be studied, so that also broad seasonal dependencies of the responses to changes in CO₂ and ozone concentration can be addressed, which have received little attention in previous modelling studies. Emmert et al. (2008) recently showed that observed long-term trends in thermospheric density do have a marked seasonal dependence, and noted that this requires further study.

5.2 CMAT2 model settings

Model simulations were carried out for day 80 (equinox) and day 172 (solstice), with CO₂ levels of 1965 and of 1995 (four runs in total). Another set of four simulations was carried out with both CO₂ and ozone concentrations adjusted

to the levels of 1965 and 1995. The years 1965 and 1995 were chosen because most observed temperature trends were obtained from measurements during this period.

A CO₂ concentration of 320 ppm was used as representative of 1965 and a concentration of 360 ppm as representative of 1995 (Keeling and Whorf, 2005). Ozone concentrations were modified from the default 1985 level using trends in ozone levels from Bojkov and Fioletov (1995). The latitudinal variation in the trend (in %·decade⁻¹) they reported was approximated by the following sinusoid:

$$6 \cdot (1 - \sin(\text{lat} + 90)) \quad (5.1)$$

This was multiplied by -1 to find the percentage change from 1985 to 1995 levels and by 1.5 to find the percentage change from 1985 to 1965 levels. A value of 1.5 rather than 2 was chosen in the latter case, even though 1965 to 1985 constitutes two decades, because the trend found by Bojkov and Fioletov (1995) was based on data from 1970 onward, and the ozone concentration did not change much from 1965 to 1970.

All simulations were set at a low solar activity level (F10.7 = 80 sfu), low geomagnetic activity level (Kp = 2+), used the HLM gravity wave parameterization, and were run for 50 days (repeating the same day number) to reach a steady state.

5.3 Differences 1995-1965 due to CO₂ and ozone concentration changes

5.3.1 Temperature

Figure 5.1 shows that, as expected, an increase in CO₂ concentration and decrease in ozone concentration, results in global cooling throughout the middle and upper atmosphere. The middle atmospheric cooling maximizes at 1.3-2.2 K around 60 km, and decreases again towards the mesopause to 0.2-1.0 K. Above the mesopause region, from about 110 km onward, there is a very sharp gradient in the temperature response, leading to a maximum cooling in the thermosphere of 6.9-8.4 K. The zero temperature change at 15 km, rapidly increasing to an increase of ~0.5 K, is a consequence of a fixed lower boundary temperature that is assumed in the model and should be ignored.

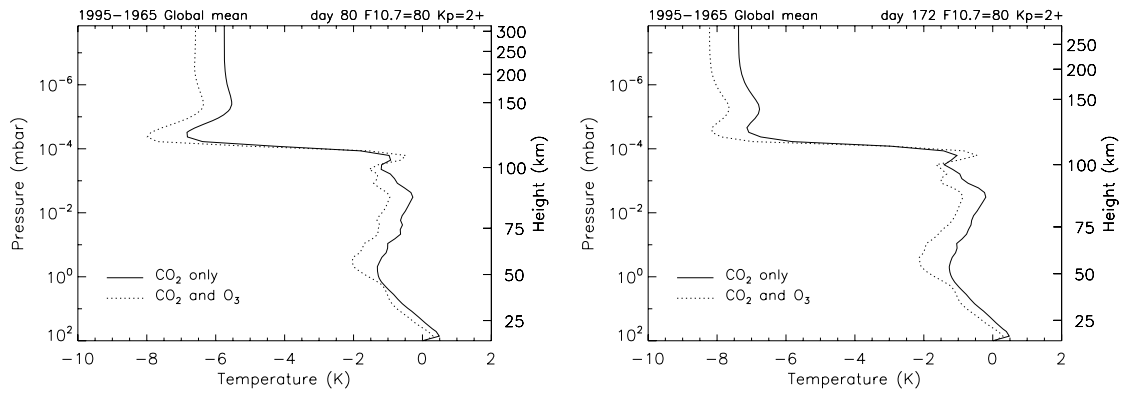


Figure 5.1. Difference in global mean temperature (K) for 1995-1965 at day 80 (left) and day 172 (right) due to a change in CO₂ concentration only and due to changes in both the CO₂ and ozone concentration.

In general there is more thermospheric cooling at day 172 (7.4-8.2 K at 250 km) than at day 80 (5.8-6.5 K at 250 km). The maximum cooling at day 80 occurs around 120-130 km (at 6.9-7.8 K), above which it relaxes to the values quoted above, while the maximum at day 172 is only reached from ~200 km onwards.

For both day 80 and day 172 there is an additional cooling effect due to changes in ozone concentration, except near the mesopause. In the thermosphere this amounts to ~11-12% extra cooling and in the middle atmosphere up to ~50-70%.

The change in global mean temperature as a function of constant height, rather than constant pressure, is shown in figure 5.2. The global mean cooling in this reference frame is stronger in the middle atmosphere (up to 3.0 K at 60-70 km) than in a constant pressure reference frame, but this decreases towards the mesopause. Just above the mesopause, even a warming can be seen of 1.0-3.3 K, which above 115-125 km turns again into a cooling that increases upwards, though not as steeply as in constant pressure coordinates. At ~280 km, a maximum cooling of 5.7-8.3 K is reached.

The zonal mean changes in temperature at day 80 and day 172 due to a change in CO₂ concentration only and due to changes in both the CO₂ and ozone concentration are presented in figure 5.3. There is not much latitudinal variation at day 80, but at day 172 there is stronger thermospheric cooling in the southern hemisphere (winter conditions), especially when also the ozone concentration is modified.

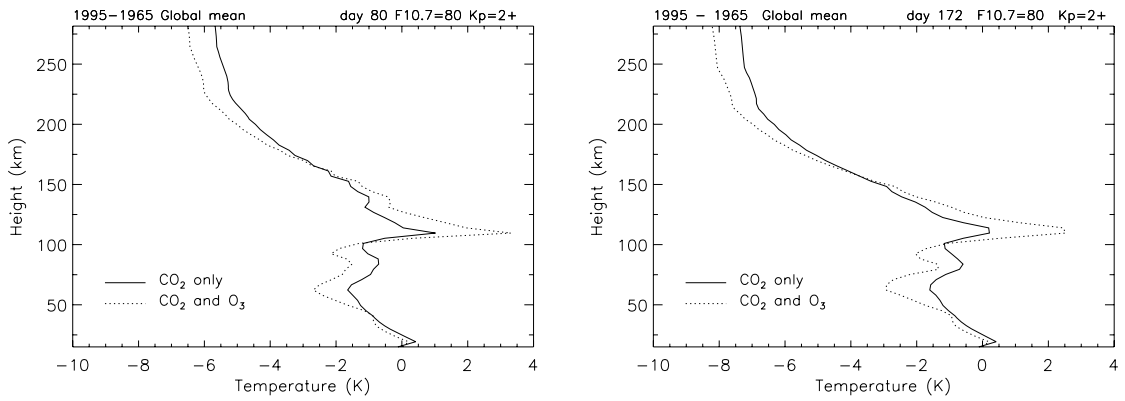


Figure 5.2. Difference in global mean temperature (K) for 1995-1965 at day 80 (left) and day 172 (right) due to a change in CO₂ concentration only and due to changes in both the CO₂ and ozone concentration in constant height coordinates.

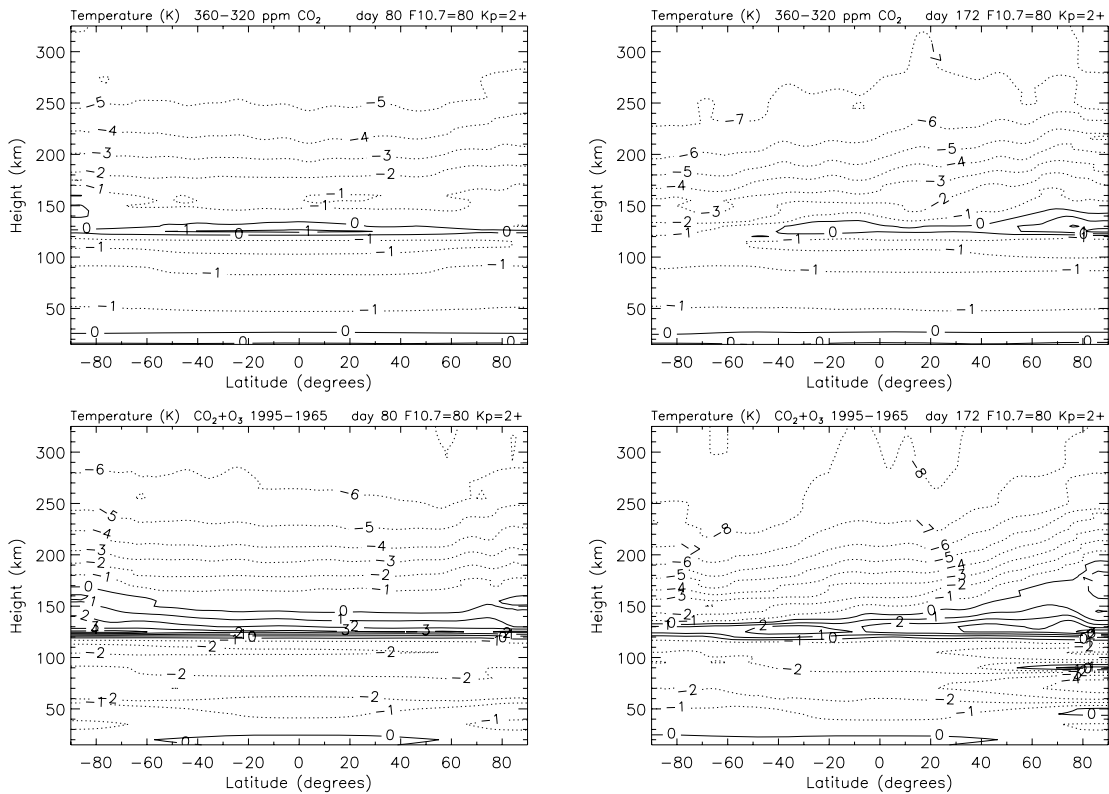


Figure 5.3. Difference in zonal mean temperature (K) for 1995-1965 at day 80 (left) and day 172 (right) due to a change in CO₂ concentration only (top) and due to changes in both the CO₂ and ozone concentration (bottom). Solid contours are positive; dashed contours negative.

5.3.2 Mesopause

The global mean changes in mesopause temperature, height and pressure are listed in tables 5.1, 5.2 and 5.3, respectively. In all cases the mesopause temperature decreases (by 0.8-1.4 K), but at day 80 the additional effect of ozone is to reduce the response, while it amplifies the response at day 172.

The height of the mesopause decreases by 0.5 km at day 80, but remains constant at day 172 when only changes in CO₂ concentration are considered. If also the ozone concentration is modified this causes a (further) lowering of the mesopause height by 1.2 and 0.7 km at day 80 and 172, respectively.

ΔT (K)	CO ₂ only	CO ₂ and O ₃
day 80	-1.0	-0.8
day 172	-1.2	-1.4

Table 5.1. Difference in global mean mesopause temperature (K) for 1995-1965 at day 80 and day 172 due to a change in CO₂ concentration only and due to changes in both the CO₂ and ozone concentration.

ΔH (km)	CO ₂ only	CO ₂ and O ₃
day 80	-0.5	-1.7
day 172	0.0	-0.7

Table 5.2. Difference in global mean mesopause height (km) for 1995-1965 at day 80 and day 172 due to a change in CO₂ concentration only and due to changes in both the CO₂ and ozone concentration.

ΔP (mbar)	CO ₂ only	CO ₂ and O ₃
day 80	$1.6 \cdot 10^{-5}$	$7.2 \cdot 10^{-5}$
day 172	$-9.5 \cdot 10^{-5}$	$-1.2 \cdot 10^{-4}$

Table 5.3. Difference in global mean mesopause pressure (mbar) for 1995-1965 at day 80 and day 172 due to a change in CO₂ concentration only and due to changes in both the CO₂ and ozone concentration.

Changes in mesopause pressure are positive at day 80, indicating that the mesopause moved downwards, and negative at day 172. The magnitude of the

changes we find may seem small at first, but given that the average mesopause pressure is of the order of 10^{-4} mbar, they are actually quite substantial (of the order of 10-50%), though it must be kept in mind that pressure decreases exponentially upwards and relatively large changes by percentage can thus easily be reached.

5.3.3 Density

The decrease in global mean density due to an increase in CO₂ concentration and the additional effects of the decrease in ozone concentration from 1965 to 1995 is shown in constant pressure coordinates in figure 5.4 and in constant height coordinates in figure 5.5. In constant pressure coordinates, the density increases nearly everywhere, while it decreases nearly everywhere in constant height coordinates. The reason for this difference will be discussed in section 5.4.1. Because all observations of long-term trends in density have been made in a constant height reference frame, the results will be discussed further based on figure 5.5 only.

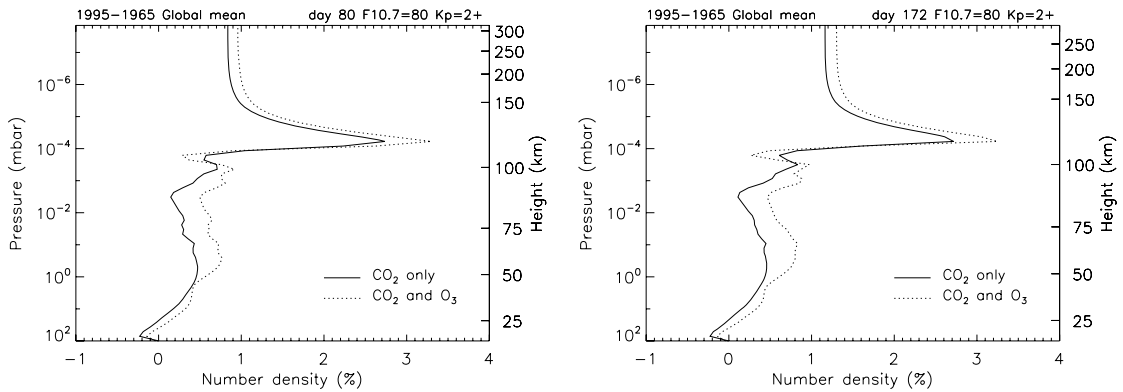


Figure 5.4. Difference in global mean density (%) for 1995-1965 at day 80 (left) and day 172 (right) due to a change in CO₂ concentration only and due to changes in both the CO₂ and ozone concentration in constant pressure coordinates.

Figure 5.5 shows that the decrease in density increases with height up to ~ 110 km to a maximum of $\sim 6\%$ for CO₂ effects only and nearly 10% for combined CO₂ and ozone effects. It then more or less stabilizes around ~ 4.5 - 6.5% , but at day 172 again increases further above ~ 220 km to 11-13% at ~ 280

km. At most altitudes there is an extra decrease in density of 1-2% due to the change in ozone concentration.

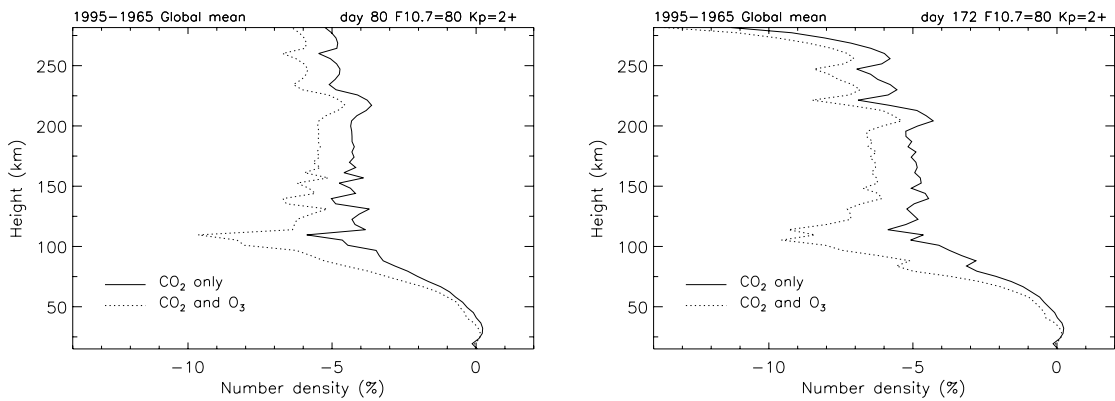


Figure 5.5. Difference in global mean density (%) for 1995-1965 at day 80 (left) and day 172 (right) due to a change in CO₂ concentration only and due to changes in both the CO₂ and ozone concentration in constant height coordinates.

5.3.4 Wind

The zonal mean changes in meridional and zonal wind strength are presented in figures 5.6 and 5.7, respectively. A positive sign reflects a strengthening in the wind and a negative sign a weakening. Changes in meridional wind strength are quite small, with at most a few ms^{-1} ($\sim 10\%$). They are somewhat larger at day 172 than at day 80, and larger when ozone changes are included than when they are not.

Changes in zonal wind strength are slightly larger than changes in meridional wind strength at a maximum of $\sim 4 \text{ ms}^{-1}$, but are still only of the order of 5-10% of typical zonal wind strengths. Changes in zonal wind strength are also larger at day 172 and larger when ozone effects are included, especially at high latitudes at day 80, but zonal wind strengths are generally higher at high latitudes, so that the percentage change might only be $\sim 5\%$.

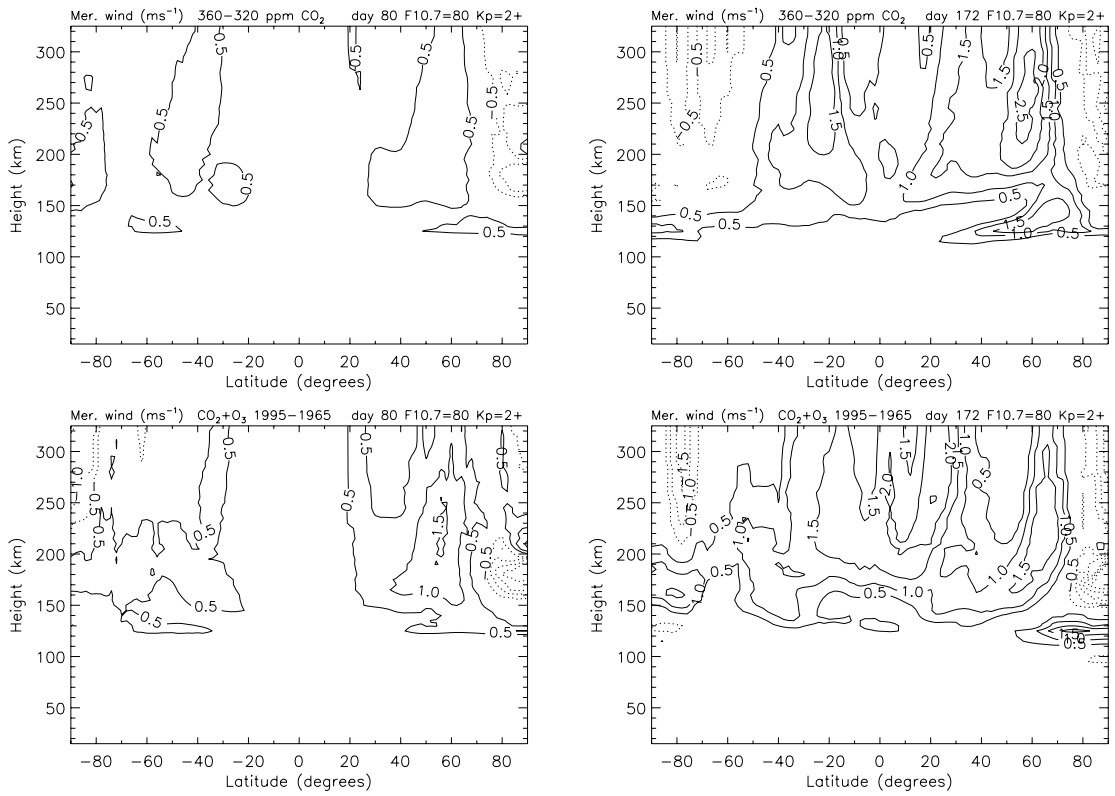


Figure 5.6. Difference in zonal mean meridional wind strength (ms^{-1}) for 1995-1965 at day 80 (left) and day 172 (right) due to a change in CO_2 concentration only (top) and due to changes in both the CO_2 and ozone concentration (bottom). Solid contours are positive; dashed contours negative.

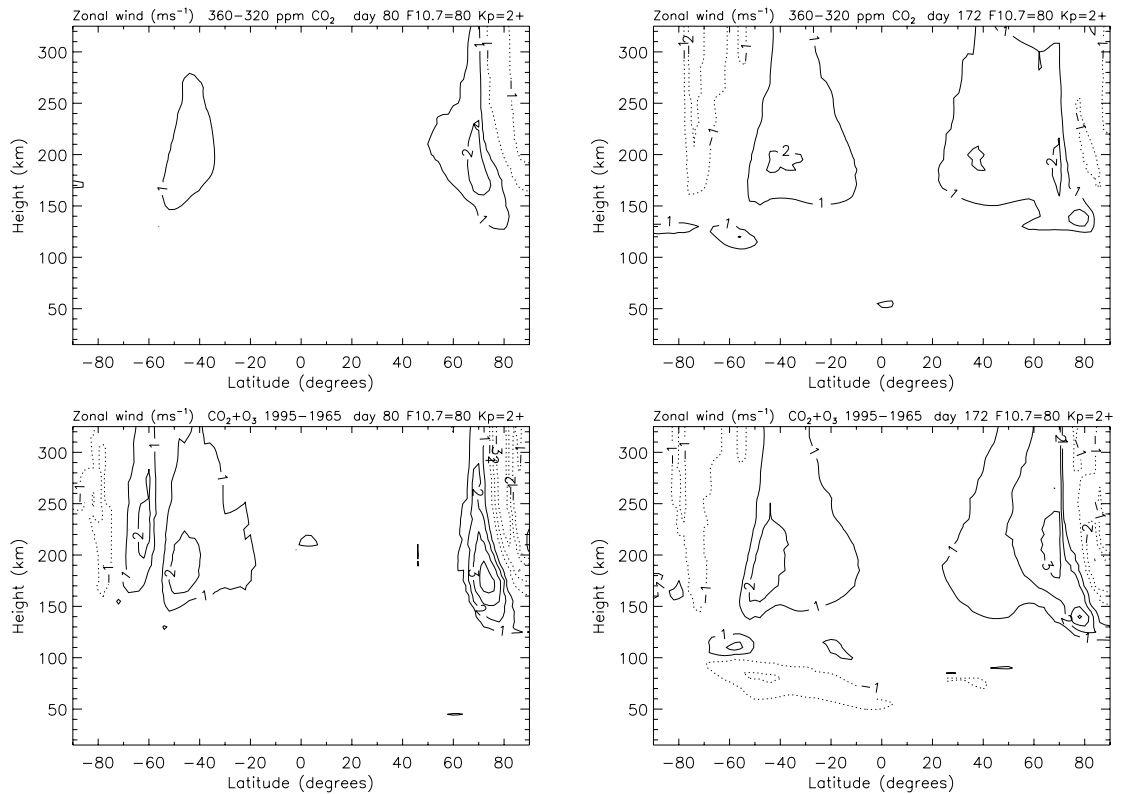


Figure 5.7. Difference in zonal mean zonal wind strength (ms^{-1}) for 1995-1965 at day 80 (left) and day 172 (right) due to a change in CO_2 concentration only (top) and due to changes in both the CO_2 and ozone concentration (bottom). Solid contours are positive; dashed contours negative.

5.3.5 Ionospheric parameters

The global mean changes in hmF2 and foF2 due to changes in CO_2 concentration only and both the CO_2 and ozone concentration are listed in tables 5.4 and 5.5. Changes in hmF2 range from -0.4 to -0.9 km. For both days the change is smaller at day 80 than at day 172, but at day 80 the additional effect of ozone is to cause a slightly larger lowering, while it is resulting in slightly less lowering at day 172.

Changes in foF2 range from 0.00 to +0.04 MHz. Changes are stronger at day 80 than at day 172, and for day 172 the trend is stronger when the additional effect of changes in ozone concentration is included. However, all changes are very small ($\leq 1\%$ of typical values for foF2).

$\Delta hmF2$ (km)	CO_2 only	CO_2 and O_3
day 80	-0.4	-0.5
day 172	-0.9	-0.8

Table 5.4. Difference in global mean hmF2 (km) for 1995-1965 at day 80 and day 172 due to a change in CO_2 concentration only and due to changes in both the CO_2 and ozone concentration.

$\Delta foF2$ (MHz)	CO_2 only	CO_2 and O_3
day 80	0.04	0.04
day 172	0.00	0.02

Table 5.5. Difference in global mean foF2 (MHz) for 1995-1965 at day 80 and day 172 due to a change in CO_2 concentration only and due to changes in both the CO_2 and ozone concentration.

5.4 Physical discussion of the obtained responses

5.4.1 Constant pressure versus constant height reference frame

We have seen that the temperature and density responses appear very different depending on the reference frame that is chosen. This is due to the contraction of the atmosphere in response to the cooling that takes place, as explained by Akmaev and Fomichev (1998).

The change in temperature seen at a constant height level is the sum of a change in temperature at a constant pressure level and the descent of air of lower pressure to that height level, as the atmosphere contracts. This means that a cooling seen at a constant height is either stronger (in the mesosphere, where temperature decreases upwards) or weaker (above the mesopause, where temperature increases upwards) than seen in constant pressure. Higher up in the thermosphere, where the temperature tends to a constant value, air descending from greater height will already have a similar temperature, so that the temperature response here remains similar, regardless of the reference frame.

Also the fact that we see an increase in density in a constant pressure reference frame, but a decrease in a constant height frame, is explained by this mechanism. First, note that it follows directly from the perfect gas law (2.1.2) that an increase in density at a fixed pressure level is expected, when the temperature at that pressure level decreases. However, due to the contraction of the

atmosphere, each pressure level moves down, and since the density decreases upwards, it is still possible for less dense air to appear at a fixed height.

5.4.2 Shape of temperature response

The most remarkable characteristic of the temperature response is probably the very sharp increase in cooling around 110-120 km (figure 5.1). There are several possible explanations for this effect. First of all, it might be due to a shift in mesopause position. The mesopause pressure increased (decreased) at day 80 (day 172), which means that the mesopause shifted downwards (upwards) in a constant pressure reference frame. In a constant height frame the mesopause shifts slightly down at both days. The effect of this on the temperature response seen in either reference frame, though this might be small in reality, is illustrated in figure 5.8.

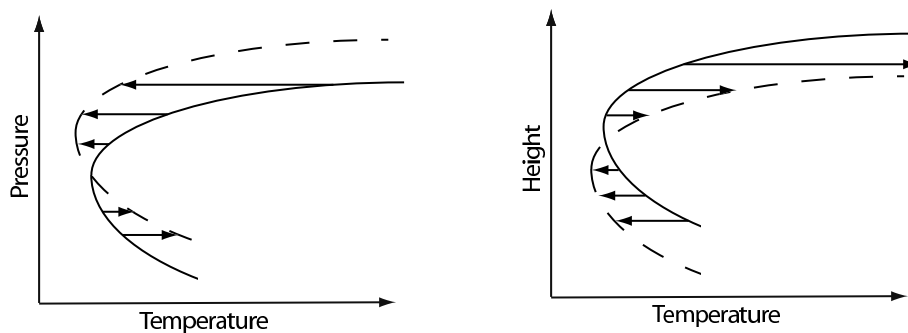


Figure 5.8. Sketch of the effect of a shift in mesopause position in a constant pressure (left) and a constant height (right) reference frame on the global mean vertical temperature profile at day 172. The solid line represents the original temperature profile (1965) and the dotted line the temperature profile after an increase in CO₂ (and ozone) concentration (1995). The arrows indicate the temperature response (pointing to the right for a warming and to left for a cooling).

In a constant pressure reference frame, an upward shift in the mesopause level, as we find at day 172, results in a cooling above the mesopause which increases rapidly upwards, corresponding to what we see in figure 5.1. It should also cause a relative warming below the mesopause. We do not see an actual

warming in figure 5.1, but it is possible that more cooling would have been present without this effect. However, at day 80 we find that the mesopause shifts downwards, and so the opposite effect would be expected, but figure 5.1 does not show this.

Also in a constant height frame the mesopause moves downwards, and therefore a rapidly increasing warming should occur above the mesopause and a cooling below. This is not at all what we see in figure 5.2, but compared to figure 5.1, the cooling occurring in the thermosphere is much more gradual. However, this effect is more likely explained by the contraction of the atmosphere, and the downward movement of constant pressure levels, causing warmer air from higher up to sink down, as already discussed in section 5.4.1. Overall then, a shift in mesopause level does not seem to explain the shape of the global mean temperature response.

An alternative explanation for the sharp cooling in the lower thermosphere is offered by Akmaev and Fomichev (1998). They assume that the vertical temperature profile in the thermosphere is a balance between radiative heating and molecular heat conduction (and so ignore any effects of convection, which is a reasonable assumption above the turbopause), and that the radiative heating does not depend on the temperature. The latter is not correct everywhere in the thermosphere, as radiative cooling rates are temperature sensitive, as they point out, and such influences will generally damp the effect considered here. However, we will follow their assumptions for now.

Following Akmaev and Fomichev (1998), we can write the energy balance equation for the thermosphere as:

$$\frac{g(x)}{\rho(x)c_p(x)} \frac{d}{dx} F(x) = h(x), \quad (5.2)$$

with $g(x)$ = gravitational acceleration,
 $\rho(x)$ = pressure,
 $c_p(x)$ = specific heat at constant pressure,
 $F(x)$ = molecular heat flux,
 $h(x)$ = radiative heating rate per unit mass,
 x = $\ln(\rho_0/\rho)$ (with ρ_0 = reference pressure).

If it is further assumed that composition depends only on pressure, which is a reasonable approximation according to Rishbeth (1990), and that the coefficient of

molecular thermal conduction can be described as $\lambda = \lambda_0(x)T^a$, the molecular heat flux $F(x)$ can be expressed as:

$$F(x) = -\frac{g(x)\mu(x)\lambda_0(x)}{R}T(x)^{a-1}\frac{dT(x)}{dx}, \quad (5.3)$$

with $\mu(x)$ = molecular mass,
 R = gas constant.

According to Banks and Kockarts (1973) $a = 0.69$ is a realistic value. In this case, and taking a lower boundary condition $T(x_b) = T_b$, where x_b is the lower boundary, equation (5.3) can be integrated to give:

$$T(x) = [(T_b)^a + aC(x)]^{1/a}, \quad (5.4)$$

with

$$C(x) = -\int_{x_b}^x [F(x) / B(x)]dx \geq 0, \quad (5.5)$$

and

$$B(x) = \frac{g(x)\mu(x)\lambda_0(x)}{R}. \quad (5.6)$$

If the lower boundary temperature T_{b0} of an initial temperature profile $T_0(x)$ is lowered by ΔT to give a new temperature profile $T_1(x)$, then the difference $T_1(x) - T_0(x)$ is given by:

$$T_1(x) - T_0(x) = [(T_b - \Delta T)^a + aC(x)]^{1/a} - [(T_b)^a + aC(x)]^{1/a}. \quad (5.7)$$

From (5.7) it can be seen that $T_1(x) - T_0(x) < 0$ for all $x > x_b$ ($a = 0.69$). This means that the entire thermosphere above the lower boundary x_b will cool, if the temperature at x_b decreases.

This corresponds to our findings, but we are now mainly interested in the evolution of this cooling as a function of x . Therefore we need to look at the gradient of $T_1(x) - T_0(x)$. Using equations (5.3) and (5.6), or taking the derivative of (5.7), this can be written as:

$$\frac{d}{dx} [T_1(x) - T_0(x)] = -\frac{F(x)}{B(x)} [(T_1(x))^{1-a} - (T_0(x))^{1-a}]. \quad (5.8)$$

Since $F(x) < 0$ and $T_1(x) - T_0(x) < 0$ for all $x > x_b$, this implies that:

$$\frac{d}{dx} [T_1(x) - T_0(x)] < 0. \quad (5.9)$$

Remembering that $T_1(x) - T_0(x) < 0$, this means that $T_1(x) - T_0(x)$ becomes more strongly negative with increasing x , and therefore any cooling that takes place at a certain level in the thermosphere will increase with increasing x (or decreasing p , upwards).

5.4.3 Shape of density response

The shape of the response in density is different from the response in temperature, even though the change in density results from the change in temperature. The density shows a more "integrated" effect, which follows from equation 5.10, which can be derived similarly to equation 2.3 (section 2.1.2):

$$\rho(z) = \rho_0 \exp \left(-g \frac{M}{k} \int_{z_0}^z \frac{dz'}{T(z')} \right). \quad (5.10)$$

The change in density at height z is thus caused by all the change in the temperature occurring between z and z_0 .

5.4.4 Seasonal differences

We have seen differences in cooling between day 80 and day 172, mainly in the thermosphere, and corresponding differences in the responses in density, hmF2, and winds. There were also differences between the summer and winter hemispheres in their thermospheric temperature response at day 172. Here we will first discuss the global mean differences between day 80 and 172, and then discuss summer-winter differences.

The stronger global mean cooling in the thermosphere at day 172 was also found by Akmaev and Fomichev (2000), though they studied January and April,

with the stronger response occurring in January. They are unsure whether this is a real effect and what is causing it (R.A. Akmaev, personal communication, 2008), and we do not have a definite mechanism yet either. However, the atmosphere certainly behaves differently at solstice compared to equinox in terms of temperature distribution, circulation patterns, etc., so that it is almost expected that a different response would occur. We will briefly explore a few possible mechanisms here.

First, differences in the vertical temperature structure between day 80 and day 172, and in the temperature gradient in the lower thermosphere, might alter the amplification of an initial cooling in the lower thermosphere with increasing height, as discussed in section 5.4.2. Also, according to the same theory, a small difference in the response between day 80 and day 172 will increase with decreasing pressure (upwards), just as the response itself increases with decreasing pressure. Therefore, a slightly stronger cooling at day 172 in the lower thermosphere could lead to a substantially stronger cooling higher up.

Another possibility is that a difference in the total amount of heating and cooling between day 80 and day 172 causes the relative impact of a change in CO₂ (and ozone) concentration to be different. The global mean cooling and heating rates are both somewhat larger at day 80 than at day 172, and figure 5.9 shows that the relative contribution of CO₂ cooling to the total cooling of the thermosphere is indeed slightly larger at day 172. Therefore, a change in the CO₂ concentration would be expected to lead to a larger cooling at day 172, as we have found.

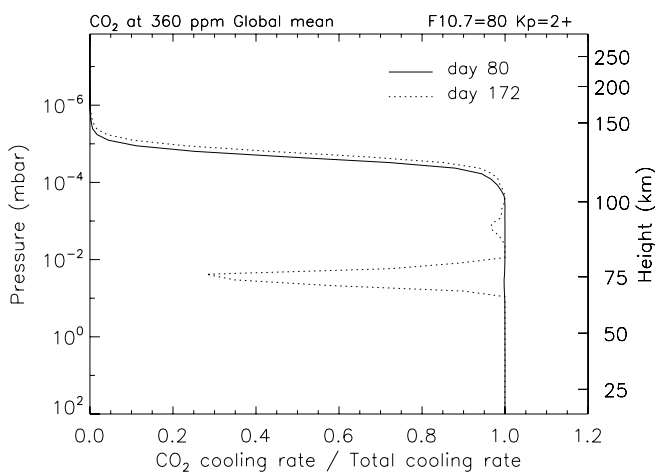


Figure 5.9. Ratio of the global mean CO₂ cooling rate to the global mean total cooling rate for the control case at day 80 and day 172.

The difference between the winter and summer hemisphere at day 172, with more cooling in the winter hemisphere, may also be related to the relative importance of CO₂ cooling. Figure 5.10 shows the ratio of the northern and southern hemispheric mean CO₂ cooling rate to the total cooling rate. At day 80 the ratios are nearly equal for both hemispheres, while differences occur at day 172. In the southern hemisphere (winter conditions) CO₂ cooling is somewhat less important near 80-90 km than in the northern hemisphere, while it is somewhat more important near 75 km. However, it is not obvious that the difference near 75 km could be dominant and hence be responsible for the larger cooling in the winter hemisphere. It is still possible that this is produced by an entirely different mechanism that we have not been able to identify yet.

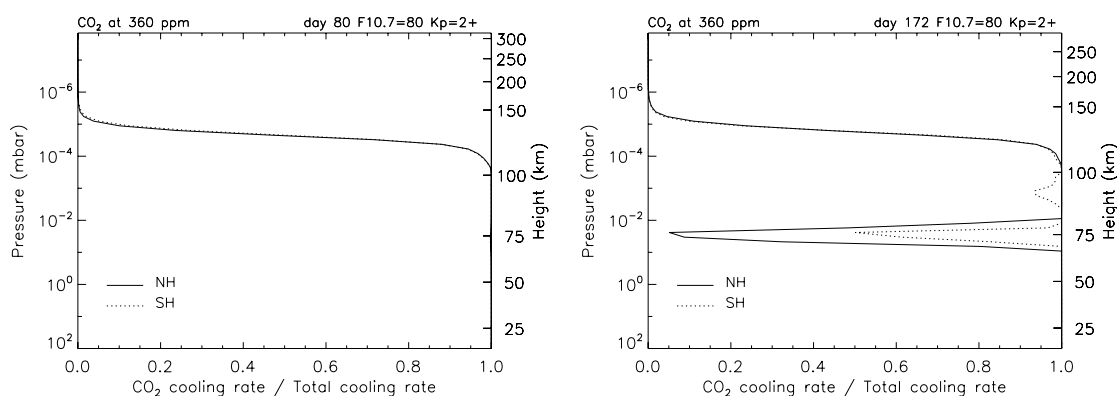


Figure 5.10. Ratio of the northern and southern hemispheric mean CO₂ cooling rate to the northern and southern hemispheric mean total cooling rate for the control case at day 80 and day 172.

5.4.5 Additional effects of changes in ozone concentration

In most parameters, we find that the additional effect of changes in ozone concentration is an increase in the response (i.e. larger cooling, decrease in density, change in wind strength) than obtained by changing the CO₂ concentration alone, as we would expect. However, we find that hmF2 decreases slightly more on day 80, but slightly less at day 172 when ozone effects are included. This is puzzling, since the change in hmF2 is presumably due to the change in temperature, which is larger when ozone effects are included throughout the F2 region for both days. It is possible though that the differences in response between CO₂ only and CO₂ and ozone combined are too small to be

significant. Also we may not have captured all of the true change in hmF2, since we have had to exclude some grid points in the night sector, where hmF2 was higher than the height range covered by CMAT2.

5.5 Comparison with other modelling studies and observations

5.5.1 Temperature

We find a maximum cooling in the middle atmosphere around 50-60 km of 2.1-2.2 K, when both ozone and CO₂ effects are included, and a smaller maximum of 1.3-1.4 K when only the CO₂ concentration change is considered. This is in fairly good agreement with Bremer and Berger (2002) and Akmaev et al. (2006), though overall our trends are somewhat smaller. Observed trends are considerably larger with $\sim 2.5 \text{ K}\cdot\text{decade}^{-1}$ at 50 km (7.5 K for 1965-1995 if a linear trend holds over this entire time window).

Higher up, temperature trends decrease to nearly no trend or even a warming in the mesopause region if viewed in a constant height reference frame. Also this is in agreement with other modelling studies, and indicated by some observations as well.

In the thermosphere, Akmaev et al. (2006) modelled a stronger cooling due to CO₂ forcing alone than due to the combined effects of CO₂ and ozone concentration changes. They claim that this is due to an enhancement of the apparent heating due to lowering of constant pressure levels when both CO₂ and ozone concentration changes are included. However, our results (in constant height) indicate that this effect is no longer dominant above 150-160 km, when cooling due to combined CO₂ and ozone forcing becomes stronger again than cooling due to CO₂ forcing alone. This may be the case because the ozone forcing is larger relative to the CO₂ forcing for 1980-2000, as modelled by Akmaev et al. (2006), than for 1965-1995, as modelled here. Also, the fact that Akmaev et al. (2006) did not include NO cooling in their model, which is important around 140-150 km, may play a role. Bremer and Berger (2002) only showed results up to 100 km.

Over the entire height range we find that changes are stronger for day 172 (in particular in the southern hemisphere, where winter conditions apply) than for day 80. Akmaev et al. (2006) modelled January and March, and found strongest cooling in January (in particular in the winter hemisphere). This is in agreement with our results, if we assume that day 172 is comparable to January. Berger and Dameris (1993) found slightly stronger cooling in summer, but their temperature

response in the lower thermosphere is generally very different from that in other modelling studies.

5.5.2 Mesopause

It is conceivable that due to the thermal restructuring of the entire middle and upper atmosphere, the position of the mesopause might shift. We do indeed find small shifts in temperature and height, and pressure. There are however strong gradients in the temperature response near the mesopause, so that observations made at slightly different vertical levels could show a relatively large difference in temperature, and temperature trends, between them (see e.g. figure 5.8). This might explain that some observational studies have indicated strong trends in the mesopause region, while others have not. Our results are consistent with the absence of a clear trend, as found by Beig et al. (2003).

We further note that we find a (small) cooling of the mesopause itself in all cases. The warming that is seen in a constant height frame near the mesopause is in fact above the mesopause, and caused by the descent of warmer thermospheric air from lower pressure levels, as a result of the contraction of the atmosphere.

5.5.3 Density

The overall height structure of the change in global mean density as modelled here is in good agreement with Akmaev et al. (2006): both show a strong increase in response up to ~ 100 -110 km, after which it stabilizes at a somewhat lower level (at least up to 200 km). Also, the combined effect of CO₂ and ozone concentration changes is stronger than that of CO₂ alone, and the response at day 172 or January is stronger than that at day 80 or March. However, the magnitude of the change in density per decade modelled by Akmaev et al. (2006) is approximately twice as large as modelled here. This is perhaps related to their larger temperature trends, though these did not differ as much from our results.

The trends found by Akmaev et al. (2006) appear in general quite large compared to observations or the modelling results by Roble and Dickinson (1989). For a doubling of the CO₂ and CH₄ concentration they found a 40% decrease in N₂ and O₂ density and a 25% decrease in O density at 200 km. If we assume that the response to a change in CO₂ concentration is mostly linear (which will be tested in chapter 6) and that most of the change found was due to CO₂ rather than CH₄,

this would correspond to approximately 5% (N_2 and O_2) and 3% (O) decrease in density for the 40 ppm change in CO_2 concentration as occurred from 1965 to 1995, which is in good agreement with our results. Bremer and Berger (2002) did not show trends in density.

Emmert et al. (2004) found a trend of 2% per decade at 200 km (so 6% for 1965-1995 if linear over this entire time window), which increased with height. This agrees very well both qualitatively and quantitatively with our modelled density decrease due to CO_2 and ozone concentration changes, though our results extend only up to 300 km.

Emmert et al. (2008) also found observational evidence of a seasonal dependence of trends in thermospheric density. They found the weakest trend in January and February, a larger trend at day 80, and a still somewhat larger trend at day 172, while trends were largest from September to November. Though we have only modelled day 80 and 172, these findings are consistent with our results, but not with those of Akmaev et al. (2006).

5.5.4 Wind

Jacobi et al. (2003) modelled a decrease in meridional wind at mid-latitudes in the mesopause region of up to 2 ms^{-1} in response to a 10% increase in CO_2 concentration and up to 10% decrease in ozone concentration. We find nearly no change (at most $0.2\text{-}0.3 \text{ ms}^{-1}$) in this region, which seems in agreement with the results of Rind et al. (1990), who found a 10-20% change in the residual circulation in response to a doubling of the CO_2 concentration (so a 1-2% change for a 40 ppm change in CO_2 concentration if the response is assumed linear).

Rishbeth and Roble (1992) found a maximum change in zonal winds of 6 ms^{-1} for a doubling of the CO_2 and CH_4 concentrations (so $\sim 0.6 \text{ ms}^{-1}$ for a 40 ppm change in CO_2 concentration if the response is assumed linear and the change in CH_4 concentration does not have a large effect). Our results indicate somewhat larger maximum changes, particularly at high latitudes, but at lower latitudes we model similar responses, especially when not considering the effects of ozone.

Most observed trends are based on measurements around 90 km and imply larger changes over a 30-year period than modelled here. Even our maximum change in zonal wind strength at day 172 at this altitude consists of at most a 2 ms^{-1} change, about three times smaller than changes implied by typical observed trends (section 3.2.3), and also observed trends in meridional winds imply much larger changes than modelled, even though these are often found not statistically significant.

It is possible that CMAT2 does not predict changes in winds correctly, for instance due to limitations of the gravity wave schemes and poorly constrained input parameters for those schemes. We have also not taken into account that a change in CO₂ concentration may change the gravity wave forcing from the lower atmosphere, as predicted by Rind et al. (1990). Alternatively, observed trends, where significant, may be (partly) due to other forcings, unrelated to changes in CO₂ and/or ozone concentration, or part of long-term dynamical cycles. This is supported by the findings of several workers that trends changed or terminated within the period they studied (e.g. Portnyagin et al., 2006), even though the CO₂ concentration continued to increase.

5.5.5 Ionospheric parameters

Rishbeth and Roble (1992) found a lowering of hmF2 of ~15 km for a doubling of the CO₂ and CH₄ concentrations, which would mean a lowering of ~1.5 km for a 40 ppm change in CO₂ concentration, assuming again a linear response and little influence of the change in CH₄ concentration at December solstice. More recently, Qian et al. (2008) found a similar decrease of 14 km for a doubling of the CO₂ concentration only (from a base level of 365 ppm). If we compare these results to our results for day 172, we find a somewhat smaller change of -0.9 km, but this is still of similar order of magnitude. The additional effect of the change in ozone concentration has not been studied before, and we find that this reduces the change at day 172 slightly (by 0.1 km), while it enhances it slightly at day 80 (also by 0.1 km).

Rishbeth and Roble (1992) found changes in foF2 of the order of 0.3 MHz, which would imply a change of $\sim 3 \cdot 10^{-2}$ MHz for a 40 ppm change under the same assumptions as above. Our results indicate similar changes, except at day 172 for effects of CO₂ only, when we find a much smaller change. However, all modelled changes are in general rather small and perhaps not significant, in agreement with the prediction by Rishbeth (1990) that foF2 would be little affected by changes in CO₂ concentration.

Observed trends in both hmF2 and foF2 can be considerably larger than modelled trends, though there is great variability in reported trends with respect to location, local time and season. Changes in CO₂ and ozone concentration on the other hand have a fairly uniform effect, causing a lowering of the F2 layer at all locations both at equinox and solstice, though the magnitude of this lowering may vary (see also Rishbeth and Roble, 1992). This may be an indication that other

processes have also contributed to observed long-term trends in hmF2 and foF2, as will be studied in more detail in chapter 7.

5.6 General discussion, conclusions and further work

In general, as expected, changes in ozone concentration, additional to changes in CO₂ concentration, increase the response in temperature, density and winds (by 10-70% depending on the parameter studied, the day number and the region within the atmosphere). The additional effect of changes in ozone concentration on the ionosphere had not been studied before. Here we find that this causes 25% extra lowering of hmF2 on day 80, but it reduces the response at day 172 by 10%. We need to be cautious with this result, as differences between CO₂ only and CO₂ and ozone combined are small, and we had to neglect some night time values. Changes in foF2 were generally very small, and probably not significant. In future work, these results should be verified with the updated version of CMAT2 that includes the GIP model and/or other models that represent the ionospheric structure more accurately than the version of CMAT2 used here does.

There is an overall agreement between responses in temperature, density, winds and hmF2 and foF2 to changes in CO₂ and ozone concentration as modelled by CMAT2 and as modelled in other studies, which gives confidence that CMAT2 can be used for these studies as well as other models. Some differences that are present can be attributed to differences in the periods that were studied, differences in the changes that were made to the atmospheric composition, and to some general differences between the models.

Most modelled changes in temperature and neutral wind are smaller than observed trends imply, and also changes in hmF2 and foF2 may be smaller than observed, even when ozone effects are included. This could be due to effects of other processes that were not considered here (or in other modelling studies), and also to some extent to errors in the data, as well as model inaccuracies and approximations. Some of these issues will be further investigated in chapter 6. On the other hand, the changes in density we find are in good agreement with observations, even though the change in temperature is considered to be the cause of the change in density, and any additional change in temperature (due to other processes than changes in CO₂ and ozone concentration) should cause an additional change in density.

Perhaps then, the difference in agreement between models and observations is due to a difference in altitude regime between temperature and

wind measurements on one hand, and density measurements on the other. Most temperature measurements are made in the stratosphere, mesosphere, and up to the mesopause region, while for the thermosphere only a few, mostly indirect measurements are available. Trends in winds are based on measurements around 90 km. In contrast, trends in density are only available for heights >200 km. In principle the density at these heights will also be affected by changes in temperature at lower altitudes, but the thermospheric cooling will contribute to this as well, and if this is somewhat overestimated, this could possibly balance the too low temperature change at lower altitudes, resulting in a very good match between observed and modelled density trends. It is indeed possible that modelling studies have overestimated the thermospheric cooling effect due to changes in CO₂ concentration, as noted by Akmaev et al. (2006), because recent studies have shown that there may be up to two times less CO₂ in the upper mesosphere and thermosphere than was previously assumed (Kaufmann et al., 2002; Kostsov and Timofeyev, 2003; O.A. Gusev, personal communication, 2008).

Based on this argument, one might expect a good match between observed and modelled changes in hmF2 and foF2 as well (since these occur also >200 km). However, hmF2 and foF2 can respond to other processes than changes in CO₂ and ozone concentration as well, which do not necessarily cause much change to the neutral atmosphere (e.g. long-term changes in the Earth's magnetic field, see chapter 7), and this may explain the discrepancy between modelled and observed changes at least to some extent.

Relatively little attention has been paid to seasonal differences in the responses to changes in CO₂ and ozone concentration, both in modelling and observational studies. Akmaev and Fomichev (1998; 2000) and Akmaev et al. (2006) did find differences between different seasons, but did not investigate this further. Still, Emmert et al. (2008) found that seasonal differences in observed trends in density are substantial, and concluded that this does need further study. We have considered here a few possible explanations for the seasonal differences we find, which are so far consistent with the results from Emmert et al. (2008). However, we examined only two seasons here, and further study will be necessary to establish whether the agreement holds for all seasons, and whether any of the mechanisms we suggested are indeed causing the variation we modelled. Recent model simulations with TIE-GCM with present-day and doubled CO₂ levels (Qian et al., manuscript in preparation) may assist with this.

6. Sensitivity analyses of modelled, CO₂-induced trends

6.1 Introduction

As mentioned in the previous chapter, there are various model approximations, as well as model noise, which could influence the results obtained from modelling studies. In this chapter, we investigate first of all the role of the gravity wave parameterization that is used in modelling the response to changes in CO₂ concentration. The gravity wave parameterization may be important, because gravity wave dissipation is a major influence on the middle atmospheric circulation and latitudinal temperature structure (see section 2.1.6). A change in the vertical temperature structure of the atmosphere due to a change in CO₂ concentration may cause changes to the dynamics, for example in the propagation of gravity waves in the middle atmosphere and their generation in the lower atmosphere (e.g. Rind et al., 1990). Any change in the circulation arising from a change in gravity wave forcing could then further modify the temperature structure, and other parameters associated with it. Since the effects of gravity waves need to be parameterized in global circulation models, the type of scheme that is used may affect the modelled response to a change in the CO₂ concentration.

The response obtained may also depend on the state of the atmosphere in the control case, and therefore the CO₂ concentration in the control case. Since studies concerned with a doubling of the CO₂ concentration often used different base levels, these can not easily be compared, and it is not clear either how they relate to the expected response to the actual change in CO₂ concentration over the past few decades. Can we assume that the response depends linearly on the change in concentration (in ppm), as we did for some comparisons in chapter 5? Or is it rather the relative change that matters? Another problem arising from using only two simulations to obtain a trend estimate is that these estimates necessarily suffer from model noise and sensitivity to starting conditions.

For these reasons we have performed modelling simulations with a wide range of CO₂ concentrations, using three different gravity wave schemes. This allows us to establish the sensitivity to both the gravity wave parameterization and exact CO₂ concentrations involved in a comparison, and also allows for a flexible comparison of our results to observed temperature trends and to other modelling studies. Further, we are able to show the evolution of each parameter as a function of the CO₂ concentration, and have obtained more robust trend estimates from the large number of simulations that we have done than can be obtained from two simulations only.

6.2 CMAT2 model settings

Model simulations were carried out for day 80 (equinox) and day 172 (solstice), with a wide range of CO₂ levels from 150 to 720 ppm. Three sets of simulations were performed, each with a different parameterization: simple Rayleigh friction, the HLM scheme, and the MK95 scheme (see section 4.2 for details). All simulations were set at a low solar activity level (F10.7 = 80 sfu), low geomagnetic activity level (Kp = 2+), and were run for 50 days (repeating the same day number) to reach a steady state.

6.3 Results

6.3.1 Temperature

For each of the three different gravity wave parameterizations, figure 6.1 shows the temperature response to a change in CO₂ concentration from 320 to 360 ppm at day 80 and day 172.

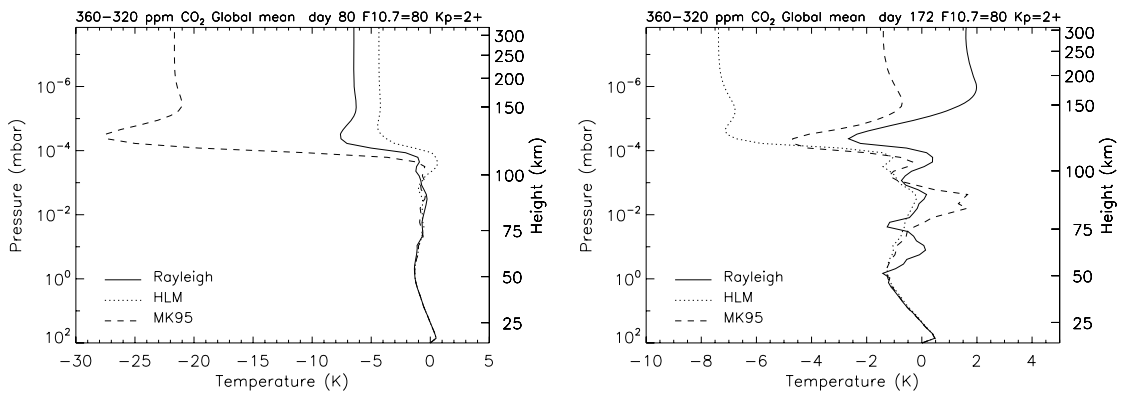


Figure 6.1. Difference in global mean temperature (K) for 1995-1965 at day 80 (left) and day 172 (right) due to a change in CO₂ concentration from 320 to 360 ppm for the three gravity wave parameterizations.

At day 80 there is a very large difference in the thermospheric cooling between Rayleigh friction and HLM on one hand (with maxima of 4.3-5.5 K) and MK95 on the other (with a maximum of 21.7 K), but responses are similar in the middle atmosphere.

At day 172 all responses are very different, in both the mesosphere and thermosphere. Within the mesosphere in particular Rayleigh drag and MK95 result in more variation with altitude in the temperature response, but we note that all trends are very small. In the thermosphere, the temperature responses become more or less constant with altitude above 150-200 km, with Rayleigh friction resulting in a small positive temperature change (up to 1.6 K) and MK95 in a small negative change (up to -1.4 K). The HLM scheme gives a much more pronounced thermospheric cooling (up to 7.4 K), and its vertical temperature change profile resembles that of day 80.

Figure 6.2 shows the global mean temperature in the thermosphere (at $2.9 \cdot 10^{-7}$ mbar) as a function of the CO_2 concentration for the three different gravity wave parameterizations. Overall the temperature decreases roughly linearly with increasing CO_2 concentration, but there are kinks or steps at some concentrations (e.g. at 360 ppm at day 80).

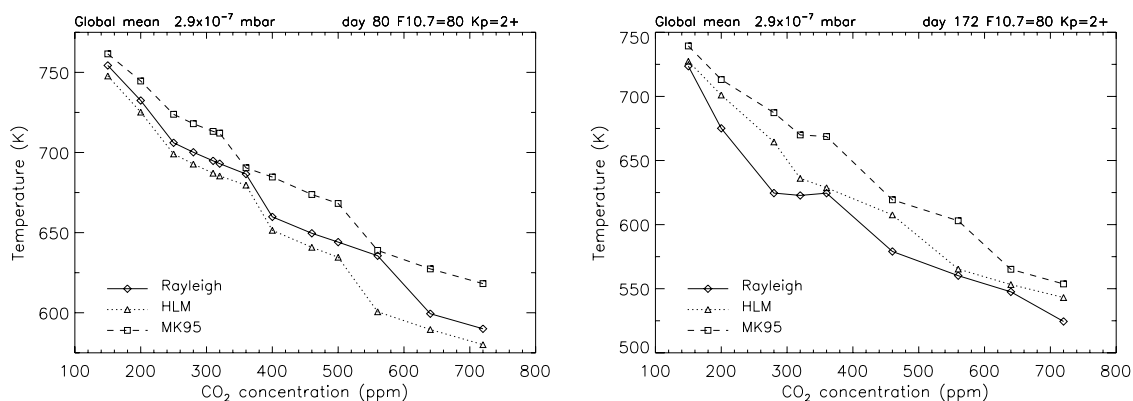


Figure 6.2. Global mean temperature (K) in the thermosphere (at $2.9 \cdot 10^{-7}$ mbar) as a function of CO_2 concentration at day 80 (left) and day 172 (right) for the three gravity wave parameterizations.

Figures 6.3 and 6.4 are similar to figure 6.2, but are for fixed pressure levels in the mesopause region ($3.1 \cdot 10^{-4}$ bar, ~ 100 km at 360 ppm) and the mesosphere ($2.4 \cdot 10^{-2}$ bar, ~ 75 km at 360 ppm), respectively. In the mesopause region, Rayleigh friction and the HLM scheme show very similar behaviour at day 80, with a small increase in temperature at low CO_2 concentrations, and a nearly linear decrease after 250 ppm. MK95 shows drastically different behaviour though, and at day 172 all schemes result in very different behaviour.

In the mesosphere all schemes give similar behaviour for both days, except Rayleigh friction at day 172 for CO₂ concentrations higher than 460 ppm. Otherwise the curves are slightly concave, but fairly smooth, with only minor kinks near 360 ppm.

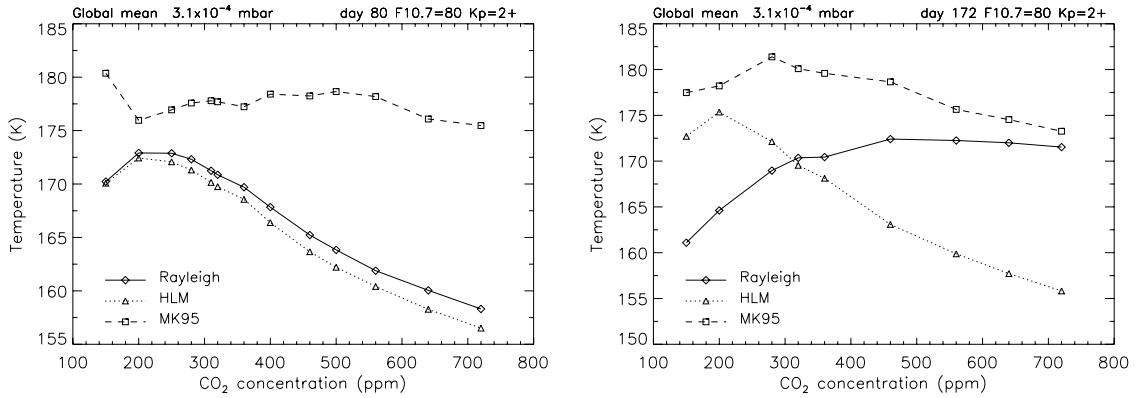


Figure 6.3. Global mean temperature (K) in the mesopause region (at $3.1 \cdot 10^{-4}$ mbar) as a function of CO₂ concentration at day 80 (left) and day 172 (right) for the three gravity wave parameterizations.

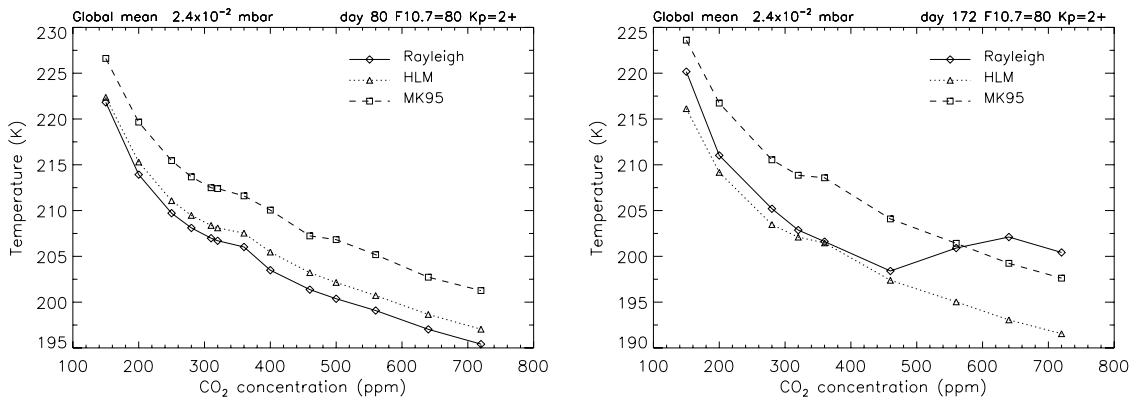


Figure 6.4. Global mean temperature (K) in the mesosphere (at $2.4 \cdot 10^{-2}$ mbar) as a function of CO₂ concentration at day 80 (left) and day 172 (right) for the three gravity wave parameterizations.

6.3.2 Mesopause

The changes in mesopause temperature, height and pressure are listed in tables 6.1, 6.2 and 6.3, respectively, for each of the three gravity wave

parameterizations. At day 80 there is a stronger temperature response for MK95 and Rayleigh friction (of -2.9 K and -1.1 K, respectively), but a slightly weaker response for HLM (-1.0 K). At day 172 the mesopause temperature lowers by 0.8-1.2 K for HLM and MK95, but there is a slight increase for Rayleigh friction of 0.1 K.

ΔT (K)	Rayleigh	HLM	MK95
day 80	-1.1	-1.0	-2.9
day 172	0.1	-1.2	-0.8

Table 6.1. Difference in global mean mesopause temperature (K) at day 80 and 172 due to a change in CO₂ concentration from 320 to 360 ppm for the three gravity wave parameterizations.

ΔH (km)	Rayleigh	HLM	MK95
day 80	-0.4	-0.5	0.2
day 172	-0.1	0.0	0.1

Table 6.2. Difference in global mean mesopause height (km) at day 80 and 172 due to a change in CO₂ concentration from 320 to 360 ppm for the three gravity wave parameterizations.

ΔP (mbar)	Rayleigh	HLM	MK95
day 80	$4.8 \cdot 10^{-6}$	$1.6 \cdot 10^{-5}$	$-1.8 \cdot 10^{-5}$
day 172	$-1.0 \cdot 10^{-6}$	$-9.5 \cdot 10^{-5}$	$-5.7 \cdot 10^{-5}$

Table 6.3. Difference in global mean mesopause pressure (mbar) at day 80 and 172 due to a change in CO₂ concentration from 320 to 360 ppm for the three gravity wave parameterizations.

At day 80, the mesopause height decreases somewhat according to the Rayleigh and HLM parameterizations, but MK95 finds it increases slightly. At day 172 there is only a very minor change in mesopause height for each of the schemes.

The mesopause pressure decreases at day 172 for all gravity wave schemes, though only a very small change is found for Rayleigh friction (of the order of 10^{-6} at an average mesopause pressure of the order of 10^{-4}). At day 80,

Rayleigh and HLM find the mesopause pressure increases (though again by a very small amount in case of Rayleigh friction), but it decreases according to MK95.

Figures 6.5, 6.6 and 6.7 show the mesopause temperature, height and pressure as a function of the CO₂ concentration. At day 80 there is little change in mesopause temperature for concentrations smaller than 250 ppm for Rayleigh friction and HLM, but after the temperature decreases smoothly, in a nearly linear fashion with increasing CO₂ concentration. MK95 results in many more kinks, and overall a decreasing response with increasing CO₂ concentration. At day 172 the HLM scheme results in similar behaviour to day 80, while Rayleigh friction shows first a decrease in mesopause temperature with increasing CO₂ concentration, but an increase after 280 ppm. MK95 now gives a smooth, concave curve, reflecting a progressively weaker decrease in mesopause temperature with increasing CO₂ concentration.

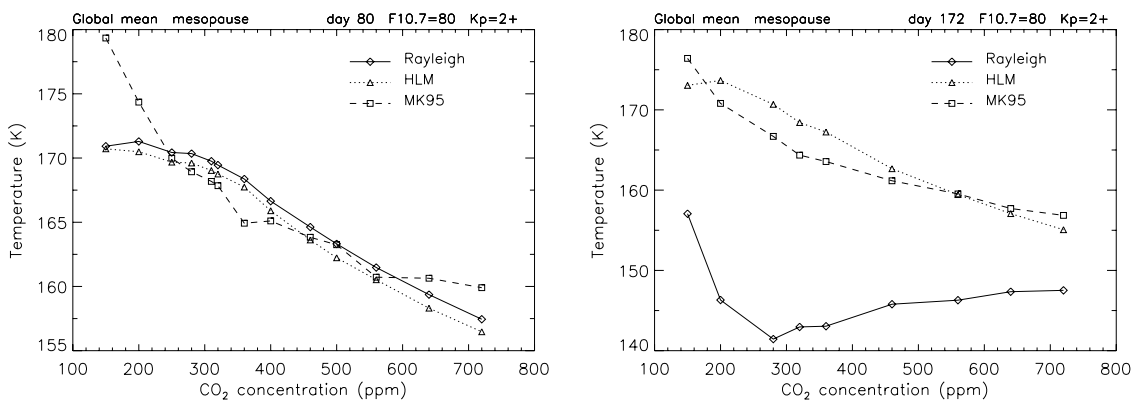


Figure 6.5. Global mean mesopause temperature (K) as a function of CO₂ concentration at day 80 (left) and day 172 (right) for the three gravity wave parameterizations.

The mesopause height decreases in all cases with increasing CO₂ concentration in a mostly linear way on both days, though steps can be seen again at several points.

The mesopause pressure shows similar behaviour at day 80 for Rayleigh friction and HLM, with the pressure first decreasing, but then increasing for CO₂ concentrations of ~280-460 ppm, and little change for higher CO₂ concentrations. For MK95, the pressure decreases with increasing CO₂ concentration at first, but at higher CO₂ concentrations this becomes progressively weaker. At day 172 there is

overall a slight increase for MK95, while there is no clear trend for Rayleigh friction and HLM.

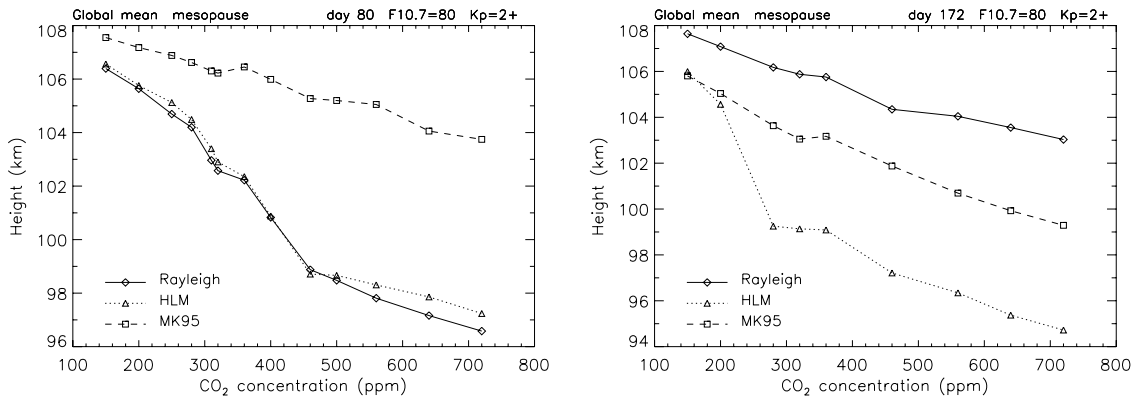


Figure 6.6. Global mean mesopause height (km) as a function of CO₂ concentration at day 80 (left) and day 172 (right) for the three gravity wave parameterizations.

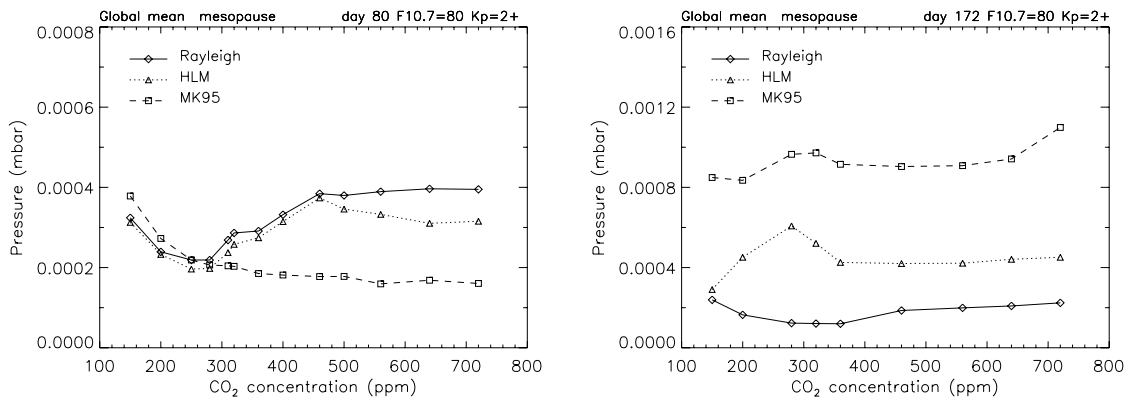


Figure 6.7. Global mean mesopause pressure (mbar) as a function of CO₂ concentration at day 80 (left) and day 172 (right) for the three gravity wave parameterizations.

6.3.3 Density

The percentage change in global mean density for the three gravity wave parameterizations is shown in figure 6.8. As with the temperature, also here, the response at day 80 is much larger for MK95 (at a maximum of nearly 18%) than for Rayleigh friction and the HLM scheme (at maxima of 5.5 and 5%), while all

parameterizations yield rather different results at day 172, and also from a lower altitude onward than at day 80.

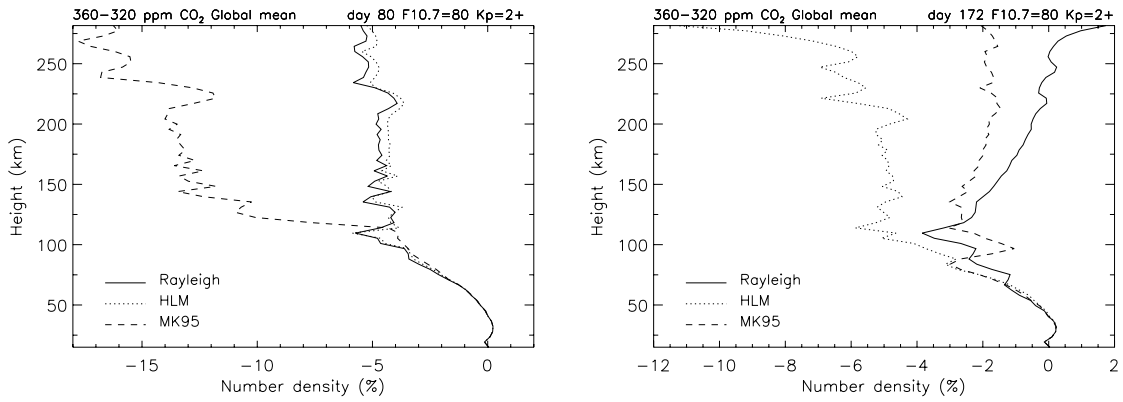


Figure 6.8. Difference in global mean density (%) for 1995-1965 at day 80 (left) and day 172 (right) due to a change in CO₂ concentration from 320 to 360 ppm for the three gravity wave parameterizations.

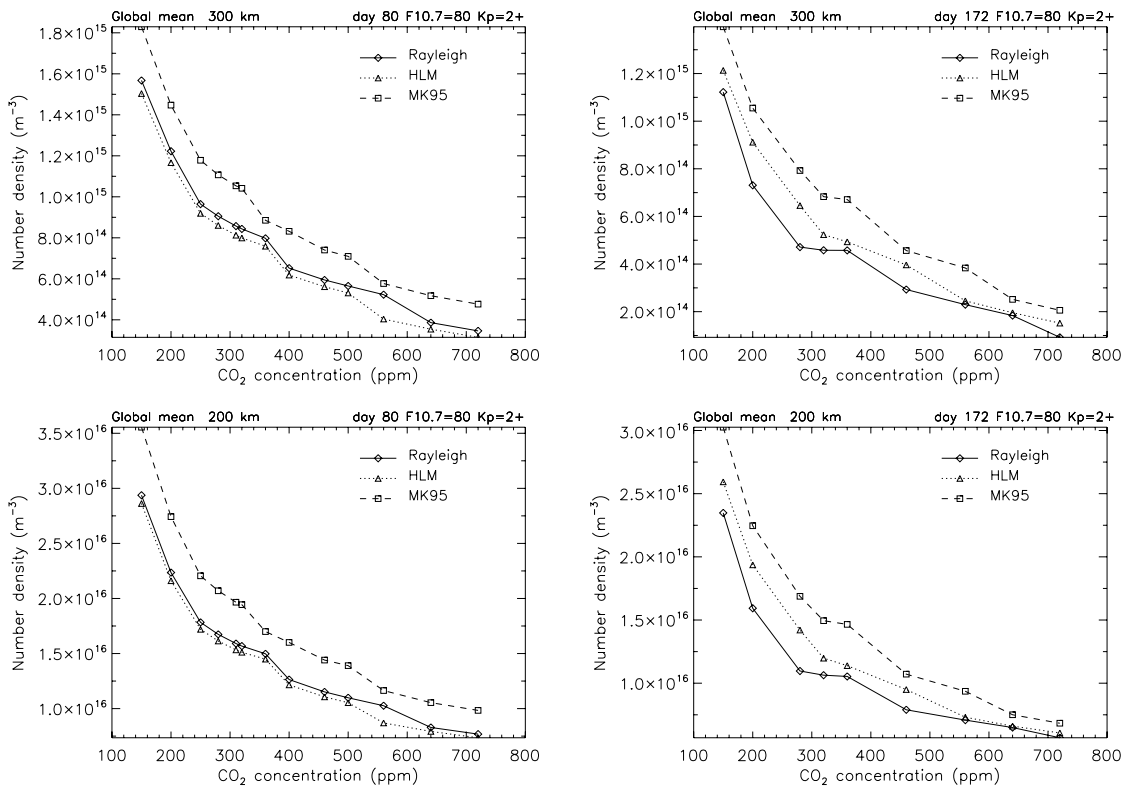


Figure 6.9. Global mean density at 200 km (bottom) and 300 km (top) as a function of CO₂ concentration at day 80 (left) and day 172 (right) for the three gravity wave parameterizations.

The global mean thermospheric density at 200 and 300 km as a function of the CO₂ concentration is shown in figure 6.9. The curves are all concave, so that the decrease in density becomes weaker with increasing CO₂ concentration, but there are some kinks or steps again (e.g. near 360 ppm).

6.3.4 Wind strength

Figures 6.10 and 6.11 show the zonal mean change in meridional and zonal wind strength, respectively. The HLM scheme gives only small changes in either (up to $\sim 2.5 \text{ ms}^{-1}$), as was also found in chapter 5. The other gravity wave parameterizations result in considerably larger changes, especially at day 172, with maximum changes up to 15 and 10 ms^{-1} in meridional and zonal wind strength, respectively, for the MK95 scheme, and up to $\sim 50 \text{ ms}^{-1}$ in both for Rayleigh friction at high latitudes. At day 80 changes in wind strength are somewhat smaller: up to 10 ms^{-1} for MK95 and up to 5 ms^{-1} for Rayleigh friction (both zonal and meridional wind strength).

We have shown before that wind strength increases in some locations and decreases in others, and therefore it would be meaningless to calculate a global mean. Instead, we have chosen one location (52°N, 18°E) to study wind strength as a function of CO₂ concentration. This location corresponds to the nearest model grid point to the station of Collm (and will be referred to as such in the following for simplicity), for which long-term trends have been observed (Bremer et al., 1997; Jacobi and Kürschner, 2006). Other locations corresponding to other stations for which long-term trends have been published were also investigated, but give similar results, which are therefore not shown. The meridional and zonal wind at Collm as a function of CO₂ concentration is shown in figures 6.12 and 6.13, respectively, each for three different altitudes: 100, 200 and 300 km.

There is no clear trend in meridional wind present at 300 km, with especially Rayleigh friction and MK95 resulting in many kinks without a consistent pattern, while HLM gives very little change at all. At 200 km there is a more consistent pattern of increasing wind strength with increasing CO₂ concentration, in particular at day 80, but there are still many steps in the curves. At 100 km MK95 shows again large variability without a clear trend, while Rayleigh friction and HLM result in nearly constant wind strength.

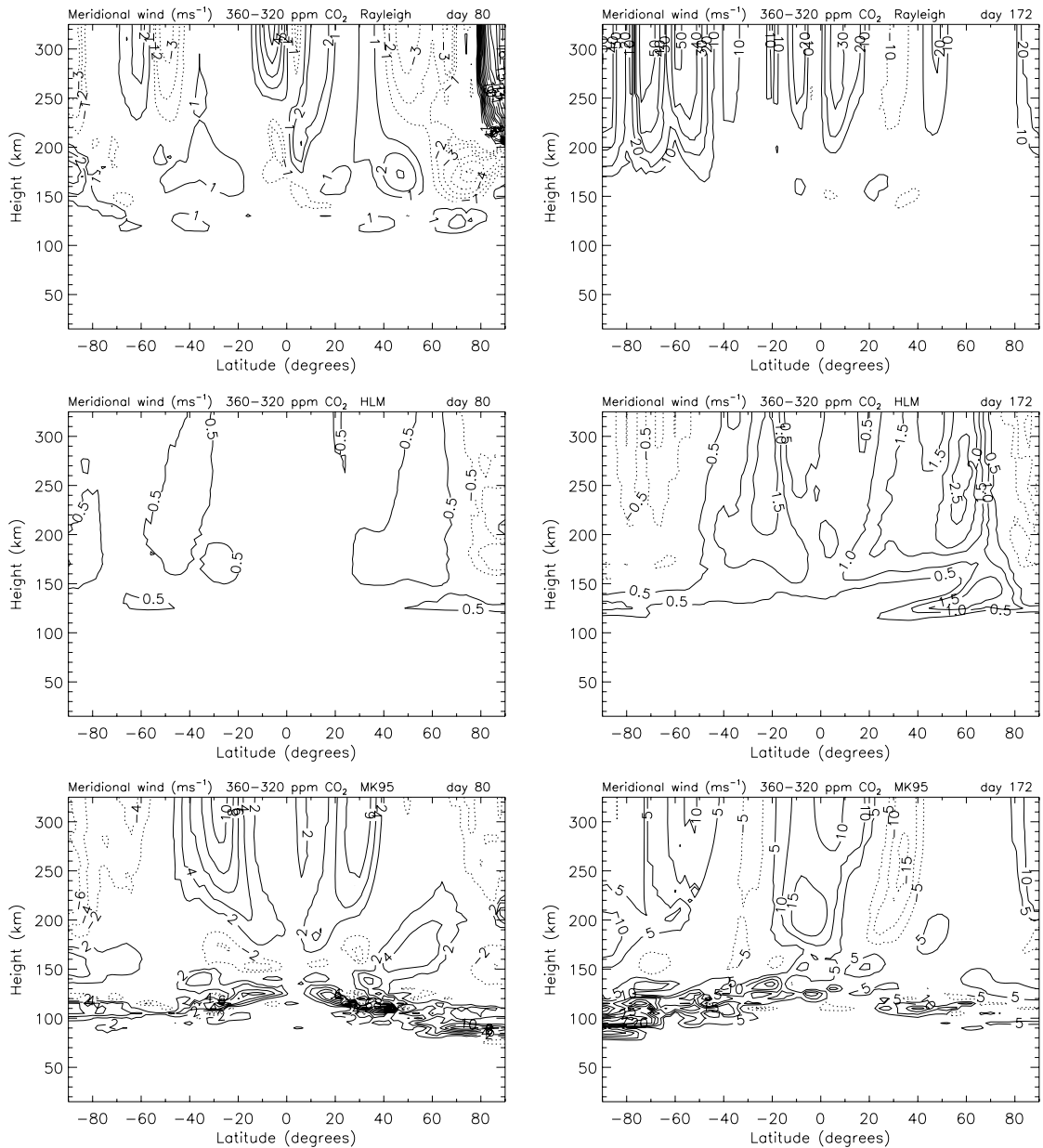


Figure 6.10. Difference in zonal mean meridional wind strength (ms^{-1}) for 1995-1965 at day 80 (left) and day 172 (right) due to a change in CO_2 concentration from 320 to 360 ppm for Rayleigh friction (top), HLM (middle) and MK95 (bottom). Solid contours are positive; dashed contours negative. Note the differences in contour interval.

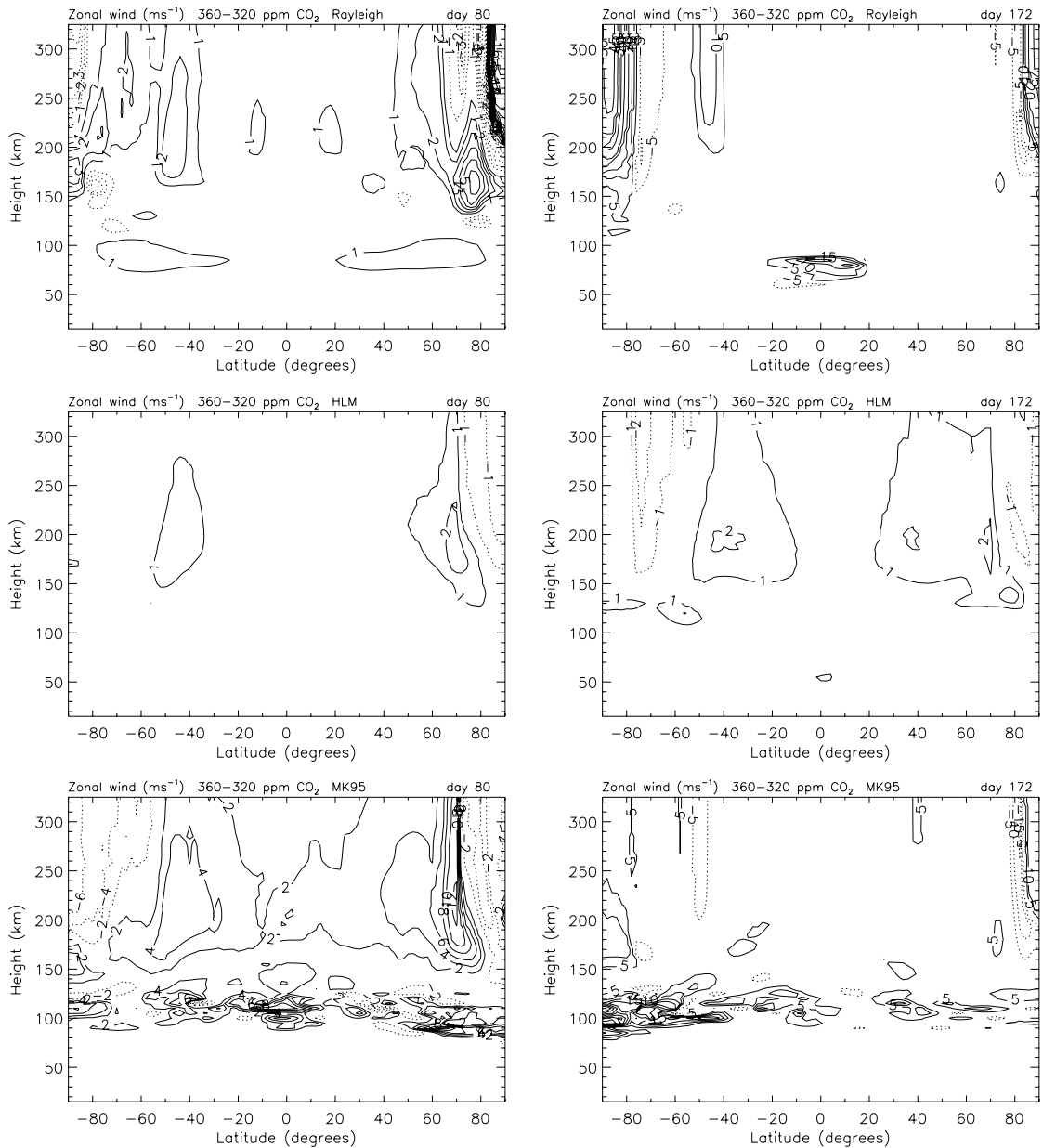


Figure 6.11. Difference in zonal mean zonal wind strength (ms^{-1}) for 1995-1965 at day 80 (left) and day 172 (right) due to a change in CO_2 concentration from 320 to 360 ppm for Rayleigh friction (top), HLM (middle) and MK95 (bottom). Solid contours are positive; dashed contours negative. Note the differences in contour interval.

The zonal wind at Collm shows no clear trend at 300 km at day 80 for MK95, but Rayleigh friction and HLM both seem to give an increase in strength for CO_2 concentrations <250 ppm, then very little change until ~ 400 ppm and a gradual decrease in strength for higher concentrations. At day 172 all three gravity wave schemes show an overall increase in zonal wind strength, both at

300 and 200 km altitude. At day 80, zonal winds at 200 km decrease in strength for low CO₂ concentrations (<360 ppm), but show only a small trend after that, and in case of MK95 they show again strong variability. Also at 100 km MK95 results in highly variable winds at day 80, but less so at day 172. The other two gravity wave schemes both show only small trends at 100 km, some being positive and some negative.

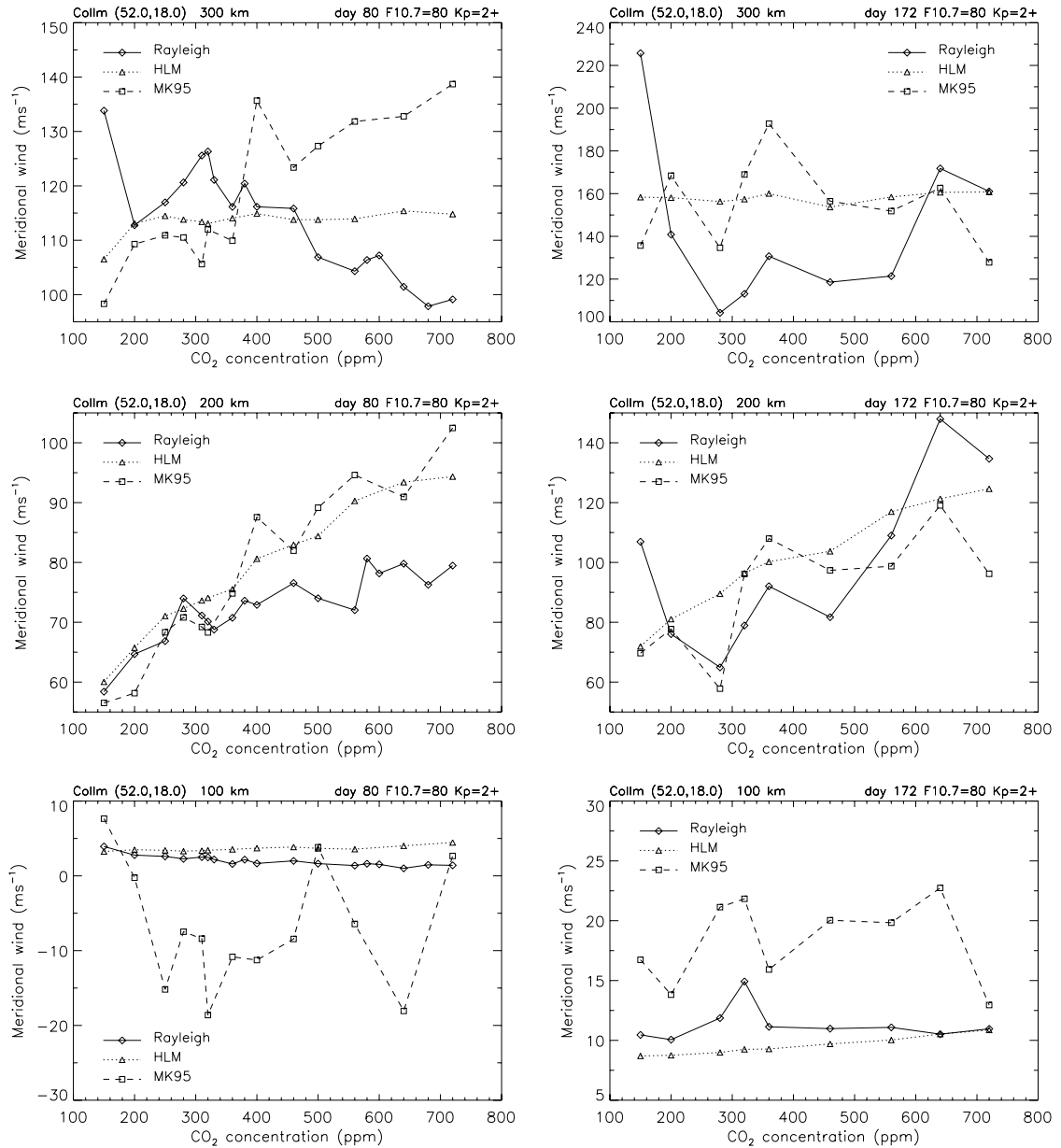


Figure 6.12. Meridional wind (ms⁻¹) at Collm (52.0°N,18.0°E) at 300 km (top), 200 km (middle) and 100 km (bottom) altitude as a function of CO₂ concentration at day 80 (left) and day 172 (right) for the three gravity wave parameterizations.

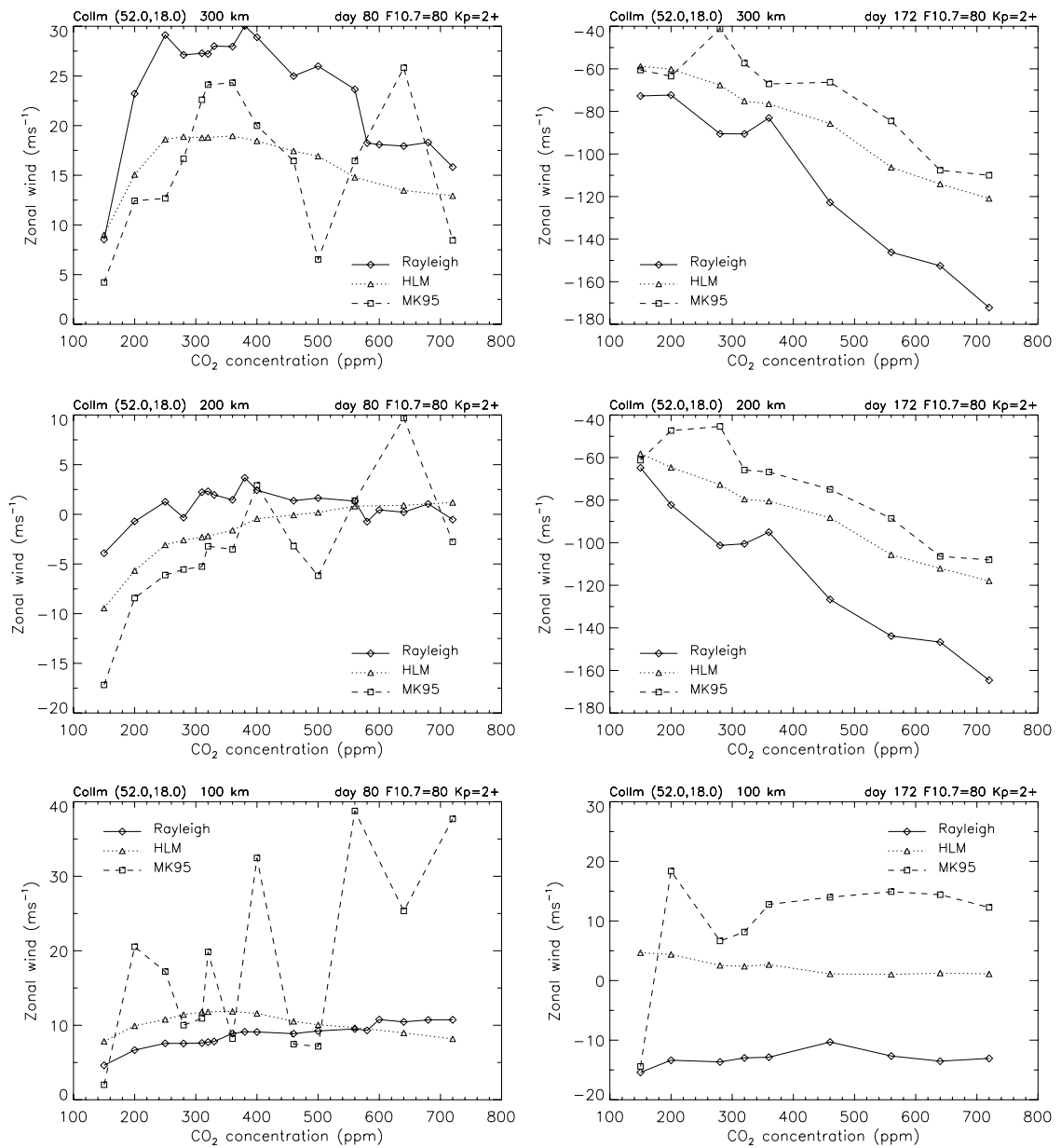


Figure 6.13. Zonal wind (ms^{-1}) at Collm ($52.0^{\circ}\text{N}, 18.0^{\circ}\text{E}$) at 300 km (top), 200 km (middle) and 100 km (bottom) altitude as a function of CO_2 concentration at day 80 (left) and day 172 (right) for the three gravity wave parameterizations.

6.3.5 Ionospheric parameters

The global mean changes in hmF2 and foF2 for the three gravity wave parameterizations are given in tables 6.4 and 6.5. The differences between the changes in hmF2 reflect similar differences as seen in the thermospheric temperature and density responses. At day 80, MK95 gives the largest change in hmF2 with a lowering of 1.5 km, ~ 3 times as large as for Rayleigh and HLM. At

day 172 HLM gives the strongest lowering, at -0.9 km, while Rayleigh friction gives a smaller decrease in hmF2 (-0.3 km) and MK95 gives a slight increase (0.1 km).

Changes in foF2 vary as well between the different gravity wave parameterizations, but are in general very small and probably insignificant, except for MK95 at day 80, where we also found an exceptionally large change in temperature.

$\Delta hmF2$ (km)	Rayleigh	HLM	MK95
day 80	-0.5	-0.4	-1.5
day 172	-0.3	-0.9	0.1

Table 6.4. Difference in global mean hmF2 (km) for 1995-1965 at day 80 and day 172 due to a change in CO₂ concentration from 320 to 360 ppm for the three different gravity wave parameterizations.

$\Delta foF2$ (MHz)	Rayleigh	HLM	MK95
day 80	0.05	0.04	0.15
day 172	-0.01	0.00	0.03

Table 6.5. Difference in global mean foF2 (MHz) for 1995-1965 at day 80 and day 172 due to a change in CO₂ concentration from 320 to 360 ppm for the three different gravity wave parameterizations.

Figures 6.14 and 6.15 show the global mean height of the peak of the F2 layer, hmF2, and its critical frequency, foF2, as a function of the CO₂ concentration. Both the hmF2 and foF2 plots show quite a few steps, which may be to some extent related to a limited number of data points that contributed to the global mean. Overall though, hmF2 decreases with increasing CO₂ concentration in similar ways for the three gravity wave parameterizations, except perhaps for MK95 at day 80. There is a fairly linear relationship between hmF2 and CO₂ concentration at day 172, but there seems to be a change in slope at 360 ppm at day 80 for Rayleigh friction and HLM, with hmF2 decreasing more rapidly for higher concentrations.

At day 80, there is an overall increase in foF2 with increasing CO₂ concentration, but there is nearly no change from 150 to 200 ppm, and at very high concentrations (>560 ppm) there is a smaller increase or even a decrease in

the case of the HLM scheme. At day 172 foF2 increases at first with increasing CO₂ concentration, but decreases again for higher concentrations, which happens at a different point for each gravity wave scheme.

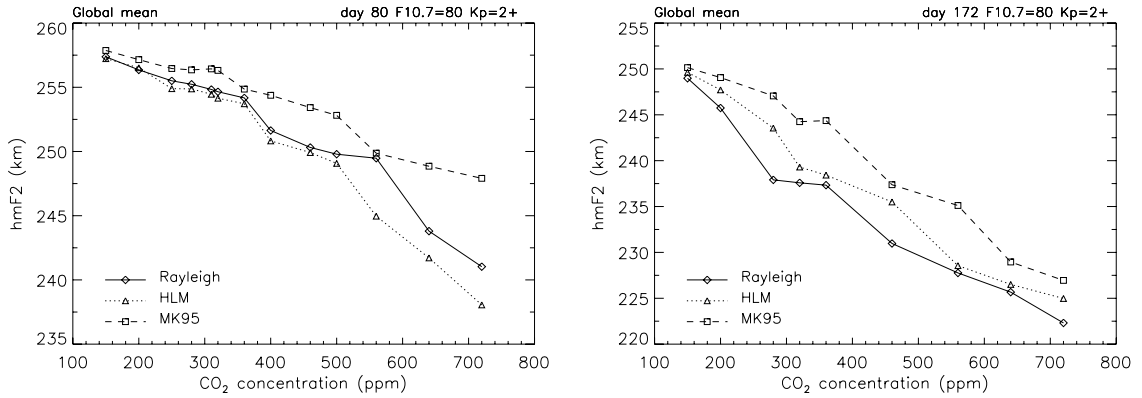


Figure 6.14. Global mean hmF2 (km) as a function of CO₂ concentration at day 80 (left) and day 172 (right) for the three gravity wave parameterizations.

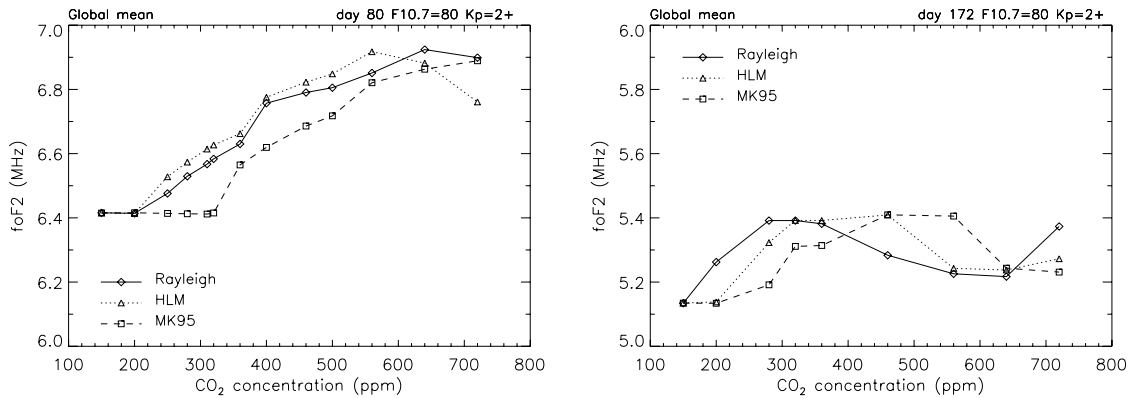


Figure 6.15. Global mean foF2 (MHz) as a function of CO₂ concentration at day 80 (left) and day 172 (right) for the three gravity wave parameterizations.

6.4 Improved trend estimates

When studying the differences between simulations with 320 and 360 ppm for each of the three different gravity wave parameterizations, we find that the response obtained can depend strongly on the gravity wave scheme that is used. However, this is mostly related to the relatively narrow window chosen for

comparison, which makes the result sensitive to local steps or kinks in the [parameter]-CO₂ function.

The cause of the kinks in the [parameter]-CO₂ functions is unclear. We do not believe they are physically realistic, as the stepwise behaviour is more suggestive of a modelling issue, which could have many possible causes. It does not seem to be directly related to any problem with the gravity wave parameterization used, as similar behaviour occurs with all three parameterizations used here. Since the only other factor that is changing between the simulations carried out is the CO₂ concentration, we suggest it may be related to the CO₂ cooling parameterization used in CMAT2 (Fomichev et al., 1998), which is widely used also in other models. However, it is beyond the scope of the present work to investigate this hypothesis further. Rather we will focus on removing the effects of unrealistic steps in the [parameter]-CO₂ relationships to obtain improved trend estimates.

To remove the effects of the steps, we find the tangent of the overall [parameter]-CO₂ relationship at 340 ppm, and multiply this by 40 to get the expected change in the parameter for a 40 ppm change as occurred from 1965 to 1995. In cases where the overall [parameter]-CO₂ relationship was linear over the entire CO₂ range studied here, we simply fit a straight line. In other cases we find a range around 320-360 ppm for which the overall relationship can be approximated by a straight line fit.

6.4.1 Temperature

Improved trends for the temperature at three levels in the atmosphere are given in table 6.6. We find there is much better agreement in the thermosphere between the gravity wave parameterizations, and there is also good agreement in the mesosphere, but in the mesopause region, the obtained trends still differ substantially between the different parameterizations.

We now find a thermospheric cooling of 10.2-11.2 K at day 80 and 12.4-13.0 K at day 172, which is ~65-95% more than what we found in chapter 5. Clearly, this earlier result was affected by the kink in the temperature-CO₂ relation in the thermosphere near 360 ppm (figure 6.2). Our improved values are in better agreement with the results by Akmaev et al. (2006).

The lack of agreement in the mesopause region suggests that this is simply a difficult region to model accurately. However, the absence of a consistent trend is in fact in agreement with observations.

In the mesosphere we also find a somewhat larger change in temperature than in chapter 5, which again brings our results in better agreement with e.g. Akmaev et al. (2006) and observations.

$\Delta T (K \cdot (40 \text{ ppm})^{-1})$	<i>Rayleigh</i>	<i>HLM</i>	<i>MK95</i>	CO_2 range (ppm)
<i>$2.9 \cdot 10^{-7}$ mbar</i>				
day 80	-11.2	-11.9	-10.2	150-720
day 172	-12.4	-12.9	-13.0	150-720
<i>$3.1 \cdot 10^{-4}$ mbar</i>				
day 80	-1.3	-1.5	0.3	250-400
day 172	0.7	-2.0	-0.6	280-460
<i>$2.4 \cdot 10^{-2}$ mbar</i>				
day 80	-1.5	-1.4	-1.4	280-460
day 172	-1.5	-1.3	-1.4	280-460

Table 6.6. Change in global mean temperature (K) in the thermosphere (at $2.9 \cdot 10^{-7}$ mbar), mesopause region (at $3.1 \cdot 10^{-4}$ mbar) and mesosphere (at $2.4 \cdot 10^{-2}$ mbar) for a 40 ppm change in CO_2 concentration, obtained from the best-fitting straight line over the range indicated for the three gravity wave parameterizations.

6.4.2 Mesopause

Table 6.7 gives improved trends in temperature, height and pressure at the mesopause. Trends in mesopause temperature are still opposite in sign between Rayleigh friction on one hand and HLM and MK95 on the other at day 172, but otherwise there is better agreement. Trends in mesopause height agree well at day 172, but at day 80 MK95 gives a much smaller trend than the other gravity wave schemes. Trends in mesopause pressure agree well between Rayleigh friction and HLM, but the trend for MK95 is an order of magnitude smaller and negative at day 80, and an order of magnitude larger at day 172.

Though results at the mesopause itself, rather than at a constant pressure level within the mesopause region, are different, also here we find that MK95 often produces different results than Rayleigh friction and HLM, confirming that this area is particularly sensitive to the type of gravity wave scheme that is used.

<i>Mesopause</i>	<i>Rayleigh</i>	<i>HLM</i>	<i>MK95</i>	<i>CO₂ range (ppm)</i>
<i>$\Delta T (K \cdot (40 \text{ ppm})^{-1})$</i>				
day 80	-1.4	-1.4	-1.1	310-560
day 172	0.9	-1.7	-1.1	280-460
<i>$\Delta H (km \cdot (40 \text{ ppm})^{-1})$</i>				
day 80	-1.0	-1.1	-0.2	250-400
day 172	-0.4	-0.5	-0.4	280-460
<i>$\Delta P (mbar \cdot (40 \text{ ppm})^{-1})$</i>				
day 80	$3.44 \cdot 10^{-5}$	$3.74 \cdot 10^{-5}$	$-6.74 \cdot 10^{-6}$	280-460
day 172	$3.47 \cdot 10^{-6}$	$1.06 \cdot 10^{-6}$	$1.07 \cdot 10^{-5}$	150-720

Table 6.7. Change in global mean temperature (K) and height (km) of the mesopause for a 40 ppm change in CO₂ concentration, obtained from the best-fitting straight line over the range indicated for the three gravity wave parameterizations.

6.4.3 Density

Improved trends in density at 200 and 300 km from straight line fits near 340 ppm are presented in table 6.8. The percentages were calculated by dividing the trend obtained in $m^{-3} \cdot (40 \text{ ppm})^{-1}$ by the average of the density at 320 and 360 ppm.

<i>$\Delta \rho (\% \cdot (40 \text{ ppm})^{-1})$</i>	<i>Rayleigh</i>	<i>HLM</i>	<i>MK95</i>	<i>CO₂ range (ppm)</i>
<i>300 km</i>				
day 80	-8.1	-8.2	-7.9	280-500
day 172	-8.4	-10.2	-8.7	280-560
<i>200 km</i>				
day 80	-7.3	-7.3	-7.1	280-500
day 172	-5.8	-7.7	-7.3	280-560

Table 6.8. Change in global mean density (%) at 200 and 300 km for a 40 ppm change in CO₂ concentration, obtained from the best-fitting straight line over the range indicated for the three gravity wave parameterizations.

At both altitudes there is very good agreement between the gravity wave schemes at day 80, with trends of -7.9 to -8.2% at 300 km, and -7.1 to -7.3% at 200 km. At day 172 HLM gives a stronger trend at 300 km (-10.2%) than the other two (-8.4 and -8.7%), and Rayleigh friction gives a weaker trend (-5.8%) at

200 km than the other two (-7.3 and -7.7%), but there is still much better agreement than obtained in section 6.3.3.

The improved trends for HLM are approximately twice as large as found in chapter 5 at day 80 and approximately 50% larger at day 172. This now makes them larger than observed trends by Emmert et al. (2004).

6.4.4 Winds

Tables 6.9 and 6.10 show the change in meridional and zonal winds, respectively, at Collm for a 40 ppm change in CO₂ concentration. In many cases, there are still large differences between trends obtained with different gravity wave parameterizations. This might be expected, since we saw in figures 6.12 and 6.13 that often no clear trend could be found.

In particular at 100 km, we find very small overall trends in most cases, which do not explain observed trends near this altitude. Therefore, from the present modelling results there is no evidence that these trends are indeed caused by changes in CO₂ concentration. However, the general inconsistency between trends obtained with different gravity wave schemes suggests that we are not yet able to model the effects of changes in CO₂ concentration on the winds accurately. Perhaps further improvements on these parameterizations need to be made, and more constraints on the gravity wave characteristics they rely on need to be collected, in order to do this.

$\Delta v_{mer} (ms^{-1} \cdot (40 ppm)^{-1})$	Rayleigh	HLM	MK95	CO ₂ range (ppm)
300 km				
day 80	-1.8	0.1	2.6	200-720
day 172	3.2	0.2	-1.9	220-720
200 km				
day 80	1.5	2.6	3.9	200-460
day 172	4.1	3.6	2.7	150-720
100 km				
day 80	-0.2	0.1	-0.1	150-720
day 172	0.0	0.2	0.1	150-720

Table 6.9. Change in meridional wind (ms⁻¹) at Collm at 100, 200 and 300 km for a 40 ppm change in CO₂ concentration, obtained from the best-fitting straight line over the range indicated for the three gravity wave parameterizations.

$\Delta v_{zon} (ms^{-1} \cdot (40 ppm)^{-1})$	Rayleigh	HLM	MK95	CO ₂ range (ppm)
300 km				
day 80	-0.3	-0.3	-0.7	280-460
day 172	-7.5	-4.7	-4.1	150-720
200 km				
day 80	0.2	0.6	1.1	250-460
day 172	-6.6	-4.3	-4.3	150-720
100 km				
day 80	0.4	-0.1	1.7	150-720
day 172	0.0	-0.2	0.1	200-720

Table 6.10. Change in zonal wind (ms^{-1}) at Collm at 100, 200 and 300 km for a 40 ppm change in CO₂ concentration, obtained from the best-fitting straight line over the range indicated for the three gravity wave parameterizations.

6.4.5 Ionospheric parameters

The changes in hmF2 and foF2, calculated from the best-fitting straight line over two different intervals, are given in table 6.11. We find a slightly smaller change in hmF2 when a smaller range is considered, which would be expected from figure 6.14, since the overall slope over this range is smaller. However, the differences are small. For foF2 we find slightly stronger changes at day 80 when a smaller range is considered, which is again expected from figure 6.15. Still, changes in foF2 remain very small, and probably not significant.

<i>Ionosphere</i>	Rayleigh	HLM	MK95	CO ₂ range (ppm)
$\Delta hmF2 (km \cdot (40 ppm)^{-1})$				
day 80	-1.1	-1.4	-0.8	150-720
day 172	-1.8	-1.8	-1.7	150-720
$\Delta hmF2 (km \cdot (40 ppm)^{-1})$				
day 80	-1.0	-1.1	-0.7	250-500
day 172	-1.7	-1.8	-1.8	250-560
$\Delta foF2 (MHz \cdot (40 ppm)^{-1})$				
day 80	0.04	0.03	0.04	150-720
day 172	0.00	0.00	0.01	150-720
$\Delta foF2 (MHz \cdot (40 ppm)^{-1})$				
day 80	0.05	0.05	0.06	250-560
day 172	0.00	0.00	0.01	150-720

Table 6.11. Change in global mean hmF2 (km) and foF2 (MHz) for a 40 ppm change in CO₂ concentration, obtained from the best-fitting straight line over the ranges indicated for the three gravity wave parameterizations.

The changes in hmF2 we find here are larger than found in chapter 5, which makes them in better agreement with other modelling results (e.g. Rishbeth and Roble, 1992).

6.5 Concluding remarks

For some parameters the overall relationship with the CO₂ concentration was linear (e.g. thermospheric temperature, hmF2). In those cases, the assumption of linearity made in chapter 5 when comparing results from CO₂ doubling studies with our 1995-1965 results was valid. Direct comparison of doubling studies that used different base levels on the other hand, would not be entirely correct, as they changed the CO₂ concentration by different amounts.

Other parameters (e.g. density at 200 and 300 km) showed a gradual weakening of their change with increasing CO₂ concentration. In those cases, dividing a change obtained by doubling the CO₂ concentration from 360 ppm by 9 to obtain the change per 40 ppm would lead to an underestimate of this change. Comparison of doubling studies with different base levels could coincidentally lead to a fairly accurate result, but not necessarily.

By performing simulations with a wide range of CO₂ concentrations, and establishing the overall [parameter]-CO₂ relationships, we obtained more robust trend estimates than can be obtained by comparing two simulations only. In particular when only a small change in CO₂ concentration is studied (e.g. from 320 to 360 ppm), the response obtained may be very inaccurate due to steps or kinks in the overall [parameter]-CO₂ relationship, which is usually fairly smooth otherwise.

Our improved trends still show a remaining sensitivity to the gravity wave parameterization that is used, varying from 15-17% in case of the mesospheric and thermospheric temperature response to as much as 55% in case of hmF2 at day 80 and as little as 3-4% in case of the density response at 200 and 300 km at day 80. Interestingly, the sensitivity of the density response is much higher at day 172 (20-27%), while the sensitivity of the response in hmF2 is much weaker at day 172 (6%). Responses of parameters at the mesopause or in the mesopause region and wind responses show a stronger dependency on the gravity wave parameterization, which may be partly related to an actual stronger dependency on gravity wave forcing, but also to model inaccuracies.

Most of our improved trends are in better agreement with observations and the modelling results from Akmaev et al. (2006) than those found in chapter 5, except for changes in density, which were in excellent agreement before, and

changes in winds, which mostly did not show any consistent trends. In chapter 5 it was suggested that the thermospheric cooling might be overestimated in our results, while cooling in the middle atmosphere was underestimated. Though our improved results now do show stronger cooling in the middle atmosphere, they also show stronger cooling in the thermosphere, and we may still (or even more) be overestimating this cooling, which would also cause the density decrease at 200 and 300 km to be overestimated.

7. Modelled effects of geomagnetic field changes on hmF2 and foF2

7.1 Introduction

The large differences in observed trends in hmF2 and foF2 from one location to another suggest these trends can not be explained by changes in greenhouse gas and/or ozone concentrations alone, since much more uniform global trends would then be expected. Alternative hypotheses to explain observed ionospheric trends have therefore been proposed, such as long-term changes in geomagnetic activity (Danilov and Mikhailov, 2001; Mikhailov, 2006) and long-term changes in the Earth's magnetic field (Foppiano et al., 1999; Elias and De Adler, 2006). The latter will be further investigated in this chapter.

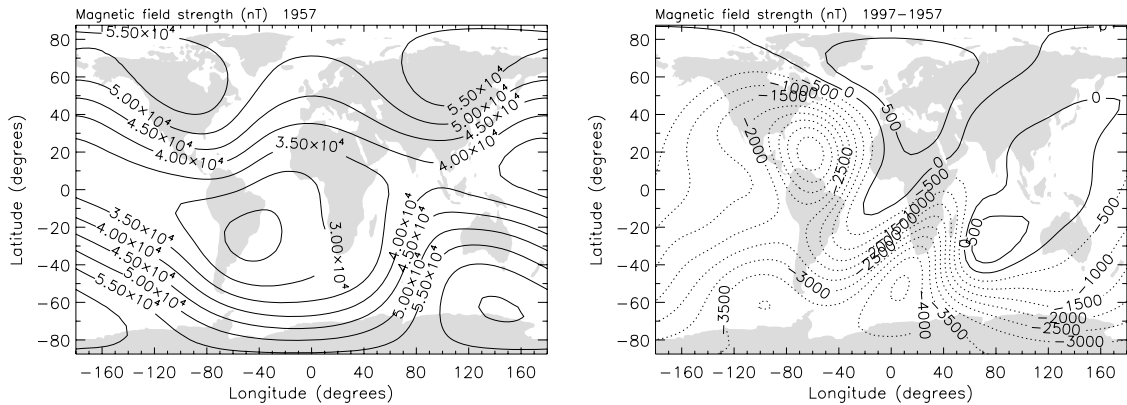


Figure 7.1. Magnetic field strength (nT) in 1957 (left) and the difference with 1997 (1997-1957, right). Solid contours are positive; dashed contours negative.

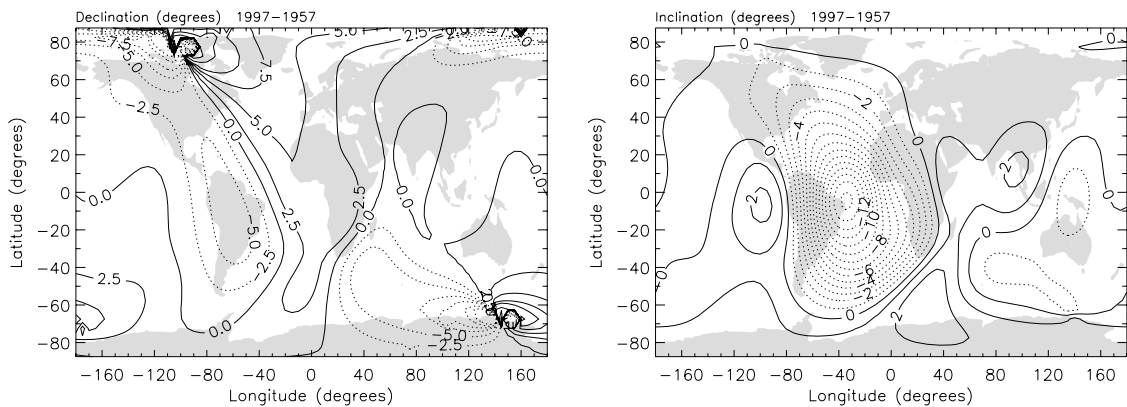


Figure 7.2. Difference in declination ($^{\circ}$) (left) and inclination ($^{\circ}$) (right) for 1997-1957. Solid contours are positive; dashed contours negative.

Figure 7.1 shows the Earth's magnetic field strength B in 1957, when many ionospheric stations started operating, and the difference with the year 1997 (1997-1957), based on the IGRF (Maus et al., 2005). Figure 7.2 shows the difference in declination and inclination between 1957 and 1997.

The Earth's magnetic field affects the ionosphere in various ways. In addition to shielding the Earth from energetic charged particles (or structuring the paths of those particles that do enter the terrestrial system), and organizing magnetospheric convection and its coupling to the ionosphere (see section 2.2.2), the geomagnetic field influences the transport of ionospheric plasma by neutral winds, and affects the generation of dynamo electric fields that induce additional plasma drifts. The neutral wind is also affected by the magnetic field, through the manner in which the field influences ion drag. These processes, collectively called electrodynamic, are further detailed below.

Consider a neutral horizontal wind \mathbf{v}_n with a component $\mathbf{v}_{n,par}$ parallel to the horizontal component of the magnetic field (positive in the magnetic field direction). Ions and electrons will be driven along magnetic field lines by this wind at a velocity $v_{n,par} \cos(I)$, where I is the field inclination with respect to the horizontal. The upward component of this velocity, $v_{n,par,v}$, is equal to $-v_{n,par} \cos(I) \sin(I)$, as illustrated in figure 7.3 (see also Rishbeth, 1998). A change in either $\mathbf{v}_{n,par}$ or the inclination (or both) will alter $v_{n,par,v}$ and thereby the height of the F2 layer: when $v_{n,par,v}$ increases, $hmF2$ increases and vice versa. It is expected that $foF2$ will also increase (decrease) somewhat as $hmF2$ increases (decreases) due to this effect (Rishbeth, 1998).

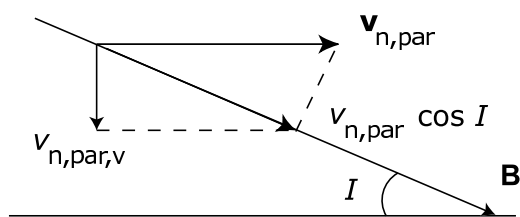


Figure 7.3. Diagram showing the component $v_{n,par,v}$ as discussed above. The magnetic field \mathbf{B} makes an angle I with the horizontal, which is drawn here in the magnetic north-south direction (so that there is no magnetic field in or out of the plane). $\mathbf{v}_{n,par}$ is the component of the neutral wind parallel to this direction and $v_{n,par,v}$ is the upward component of $v_{n,par} \cos(I)$. $v_{n,par,v}$ is therefore a negative quantity in this sketch.

The change in the $\sin(I) \cos(I)$ factor is shown in figure 7.4. The change in this factor indicates that changes in hmF2 and foF2 may be expected, though the magnitude of this change would strongly depend on location. Note that $\mathbf{v}_{n,par}$ will also change as the magnetic field changes, because changes in the declination will change the projection of \mathbf{v}_n onto the magnetic north direction, even if the horizontal wind itself stayed constant. Additional changes in the wind itself are also expected to occur though, through changes in ion drag.

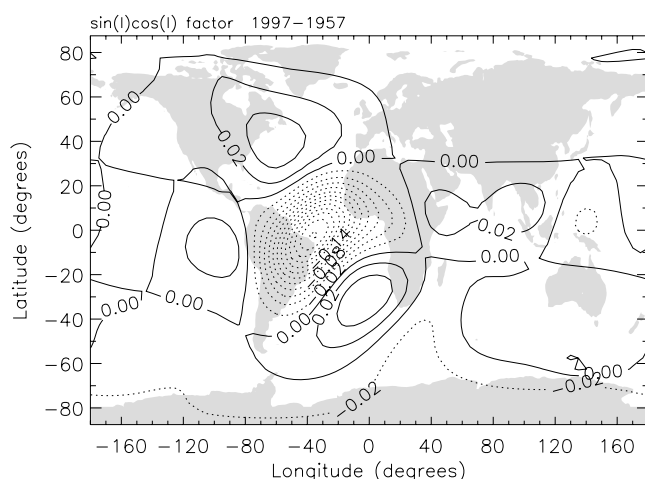


Figure 7.4. Difference in $\sin(I) \cos(I)$ factor for 1997-1957. Solid contours are positive; dashed contours negative.

A change in the direction of the magnetic field changes the ion drag acting on the wind. Ion drag is proportional to the difference of ion and neutral velocities. If we neglect for the moment electric field effects on the ion velocity, then in the F region this velocity is zero in the magnetic east-west direction, and approximately $v_{n,par} \cos(I)$ along the magnetic field, which has a horizontal component in the magnetic northward direction of $v_{n,par} \cos^2(I)$. Thus horizontal ion drag is anisotropic, being proportional to $v_{n,east}$ in the magnetic eastward direction, and to $v_{n,par} - v_{n,par} \cos^2(I) = v_{n,par} \sin^2(I)$ in the magnetic meridional direction. A change in magnetic declination will change the axis of the anisotropy with respect to geographic coordinates, thus changing the ion drag on the wind. Additionally, a change in I will change the strength of ion drag in the magnetic meridional direction.

The neutral wind is also responsible for the generation of a dynamo electric field through $\mathbf{E}_{dyn} = \mathbf{v}_n \times \mathbf{B}$. Both the change in \mathbf{v}_n itself, as described above, and the changes in declination and inclination will alter the component of \mathbf{v}_n perpendicular

to \mathbf{B} . In addition, a change in the magnitude of \mathbf{B} will change the ionospheric conductivity. These combined effects will induce a change in the electric field \mathbf{E}_{dyn} . The change in \mathbf{E} and \mathbf{B} will not only cause changes to the ion drag exerted on the neutral wind, further modifying \mathbf{v}_n , but will also modify the \mathbf{ExB} drift of ions and electrons. The vertical component of this drift can be expected to change the peak height of the F2 layer and foF2 too.

7.2 Methods

From the above it is hard to determine analytically in what sense the \mathbf{ExB} drift and the neutral wind will change, how various changes will interact, and how hmF2 and foF2 will be modified as a consequence. Therefore, a numerical model which takes the electrodynamic coupling mechanisms into account is needed to solve this problem. Previous studies that have attempted to quantify the long-term effects of changes in the magnetic field used a constant neutral wind field (Jarvis et al., 1998; Elias and De Adler, 2006) and could therefore not do this.

Here, we use TIE-GCM (see section 4.4) to investigate to what extent changes in the Earth's magnetic field since 1957 have induced changes in the Earth's ionosphere. TIE-GCM provides a self-consistent solution of the electro-dynamics for geomagnetic latitudes lower than 60° that is needed to determine the combined effects of changes in the Earth's magnetic field strength and direction.

We have performed full year simulations both with the IGRF of 1957 and that of 1997. For all simulations a moderate solar activity level ($F_{10.7} = 150$ sfu) was used. The cross-polar cap potential was set at 45 kV and the hemispheric power of precipitating auroral particles was set to 16 GW, reflecting geomagnetically quiet conditions. Any effects of changes in particle precipitation, expansion/contraction of the auroral oval, and changes in high-latitude convection that might occur due to a change in the Earth's magnetic field strength were not accounted for. The model does account for high-latitude effects due to changes in the orientation of the field, and for the lower latitude effects as described in the introduction.

We will show the differences between the results both globally for selected seasons and universal times, and at two selected locations throughout the year for all local times. These locations, given in table 7.1, were chosen close to two ionospheric stations in areas where the change in the magnetic field has been relatively large and for which long-term trends in hmF2 and foF2 were published (see table 3.4). Though the locations we chose do not exactly coincide with the

ionospheric station named, we will refer to them as such in the following for simplicity.

	<i>Argentine Islands</i>		<i>Concepción</i>	
	1997-1957		1997-1957	
Location (lat,lon)	-65.2, -64.3		-36.8,-73.0	
Model location (lat,lon)	-67.5, -65.0		-37.5,-75.0	
B (nT)	$4.26 \cdot 10^4$	$-3.74 \cdot 10^3$	$5.09 \cdot 10^4$	$-2.36 \cdot 10^3$
D (°)	12.10	0.03	6.66	-4.84
I (°)	-59.46	0.12	-34.70	-2.89
sin (I) cos (I)	-0.4376	-0.0010	-0.4680	-0.0154

Table 7.1. Details of the selected locations for this study. For both model locations the magnetic field strength B , declination D , inclination I , and the “factor” $\sin (I) \cos (I)$ of 1957 are given. The change of each of these quantities from 1957 to 1997 is also given.

7.3 Results

7.3.1 Global change in hmF2 and foF2

The global change in hmF2 and foF2 from 1957 to 1997 for day 80 and day 172, both at 0 and 12 UT, is shown in figures 7.5 and 7.6. Changes are very small in most regions, but become much larger over the Atlantic Ocean and South America, roughly from -50° to $+50^\circ$ degrees latitude and -90° to $+10^\circ$ longitude (somewhat varying with season and local time), which is the same region where the change in the $\sin (I) \cos (I)$ factor is largest. Near the equator, changes in hmF2 reach up to ± 20 km ($\sim 5\%$) and changes in foF2 up to ± 0.5 MHz ($\sim 10\%$) for most seasons and times of day, and in some cases even larger changes can be found.

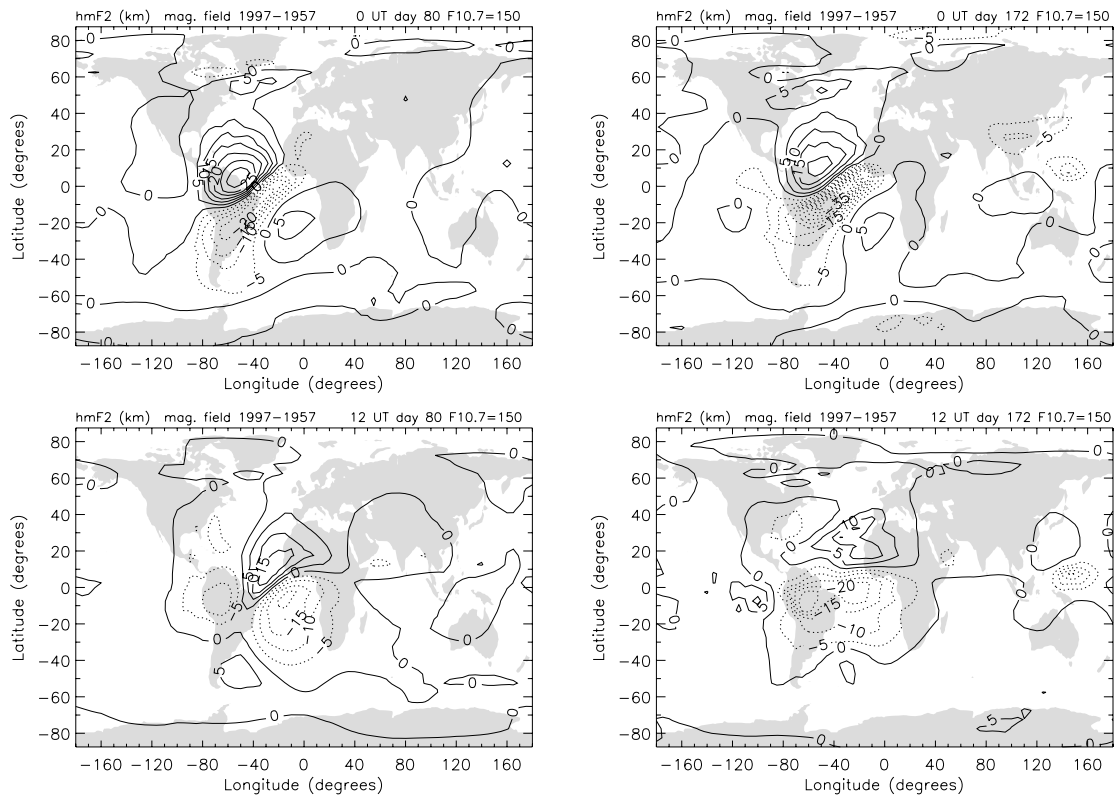


Figure 7.5. Difference in hmF2 (km) for 1997-1957 due to changes in the Earth's magnetic field at day 80 (left) and day 172 (right) at 0 UT (top) and 12 UT (bottom).

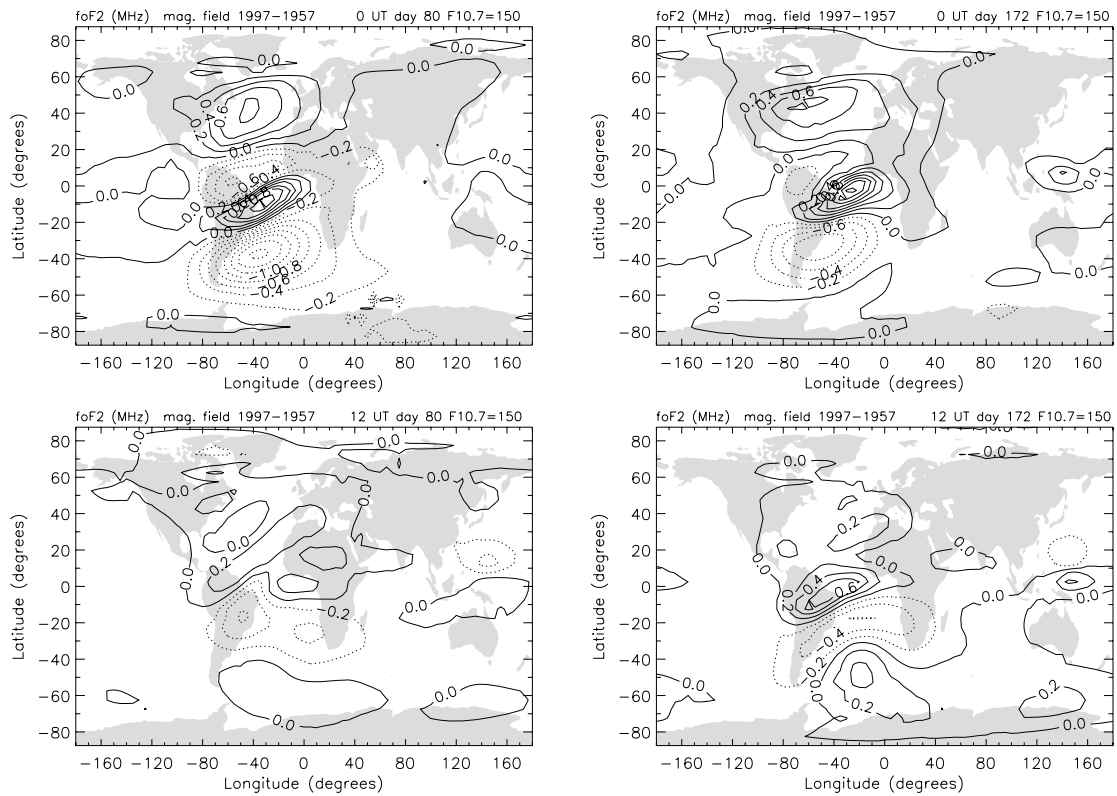


Figure 7.6. Difference in foF2 (MHz) for 1997-1957 due to changes in the Earth's magnetic field at day 80 (left) and day 172 (right) at 0 UT (top) and 12 UT (bottom).

7.3.2 Seasonal and diurnal variation

Figures 7.7 and 7.8 show the change in hmF2 and foF2 at Concepción and Argentine Islands as a function of season and local time. Concepción shows the strongest changes in hmF2 and foF2, ranging from approximately -12 to +6 km and -0.8 to +0.3 MHz, respectively. Changes at Argentine Islands are generally weaker, and also show a very different pattern. Results from additional locations (not shown) confirm that changes in hmF2 and foF2 depend strongly on season and local time, varying not only in magnitude, but even in sign, and that this dependence is in turn dependent on location.

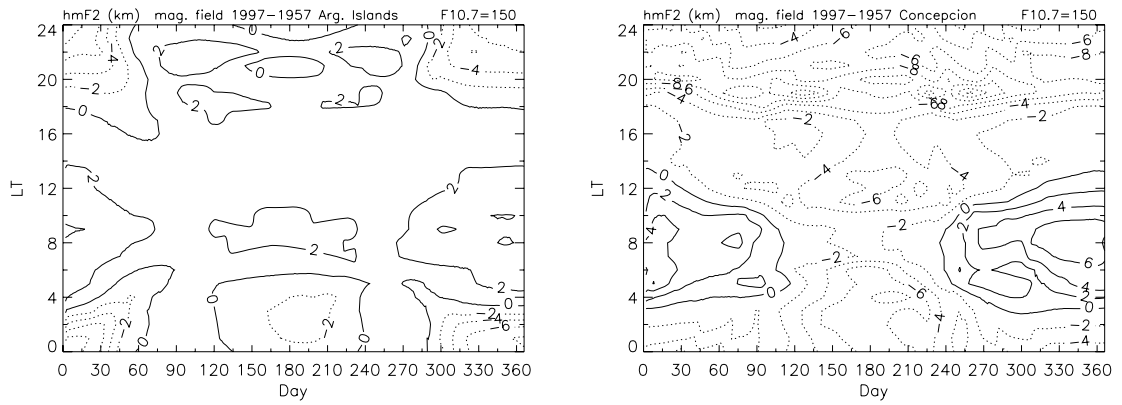


Figure 7.7. Seasonal and diurnal variation of the difference in hmF2 (km) for 1997-1957 at Argentine Islands (left) and Concepción (right) due to changes in the Earth's magnetic field.

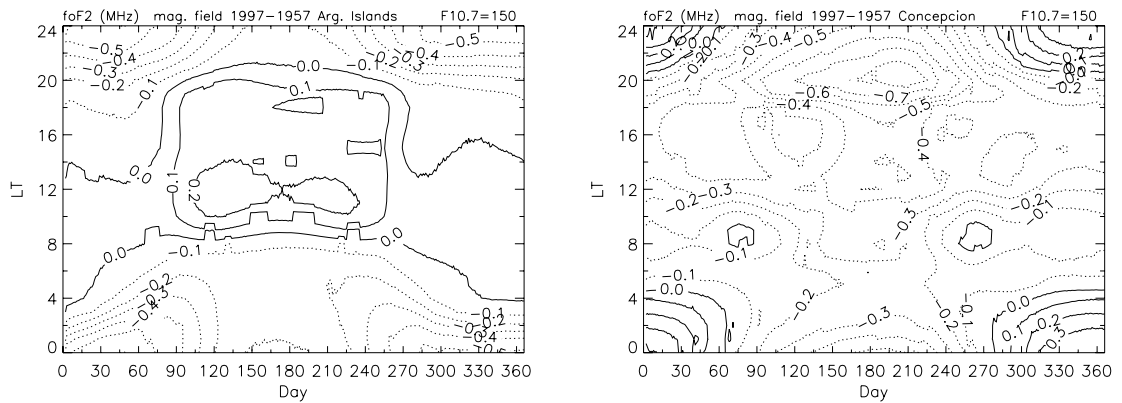


Figure 7.8. Seasonal and diurnal variation of the difference in foF2 (MHz) for 1997-1957 at Argentine Islands (left) and Concepción (right) due to changes in the Earth's magnetic field.

7.4 Discussion

7.4.1 Cause of modelled changes in hmF2 and foF2

In the introduction we identified two possible causes of changes in hmF2 and foF2 in relation to changes in the Earth's magnetic field: changes in $v_{n,par,v}$ and changes in the vertical component of the \mathbf{ExB} drift. These quantities, which we will also refer to from now on as $\Delta v_{n,par,v}$ and $\Delta v_{E,v}$, are shown in figures 7.9 and 7.10, again for day 80 and 172, at 0 and 12 UT. The global pattern of $\Delta v_{n,par,v}$ is most similar to the patterns of $\Delta hmF2$ and $\Delta foF2$, while there is not much similarity

between those and the pattern of $\Delta v_{E,v}$. This suggests that the change in $v_{n,par,v}$ is the more important factor of the two in causing the changes in hmF2 and foF2, though it does not fully explain them. This may be because we show $\Delta v_{n,par,v}$ at the same time as $\Delta hmF2$ and $\Delta foF2$, while it takes time for $\Delta v_{n,par,v}$ to cause a change in hmF2 and foF2. Also, we show $\Delta v_{n,par,v}$ at the hmF2 height, while $\Delta v_{n,par,v}$ at other heights will also influence hmF2 and foF2.

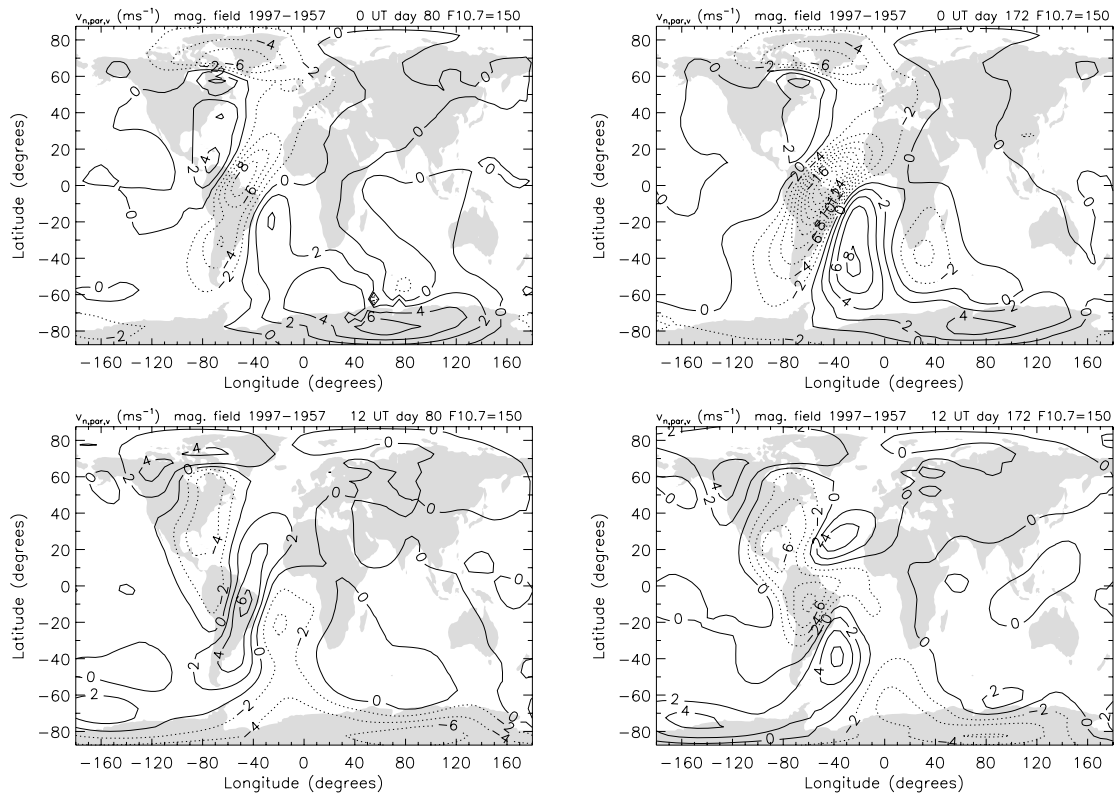


Figure 7.9. Difference in $v_{n,par,v}$ (ms^{-1}) at hmF2 height for 1997-1957 due to changes in the Earth's magnetic field at day 80 (left) and day 172 (right) at 0 UT (top) and 12 UT (bottom).

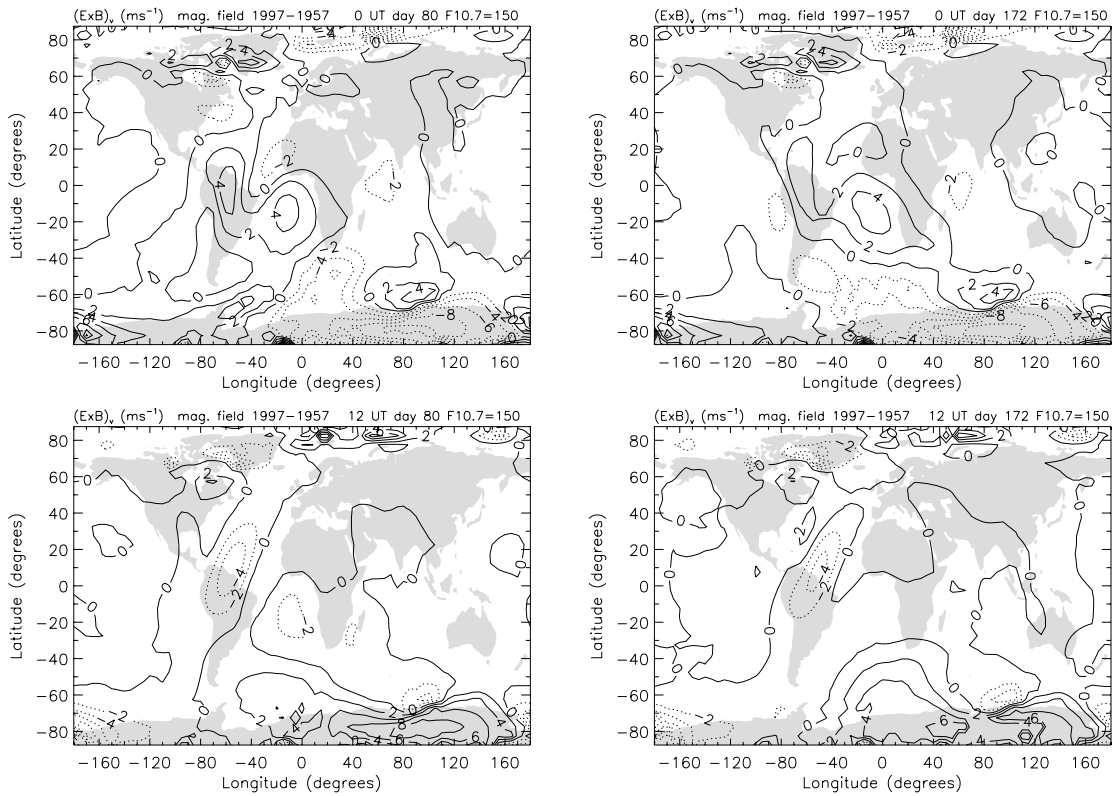


Figure 7.10. Difference in vertical \mathbf{ExB} drift (ms^{-1}) at hmF2 height for 1997-1957 due to changes in the Earth's magnetic field at day 80 (left) and day 172 (right) at 0 UT (top) and 12 UT (bottom).

The change in $v_{n,\text{par},v}$ itself can be due to changes in the horizontal neutral wind, changes in its projection onto magnetic field lines due to changes in the declination, and changes in the inclination affecting the $\sin(I) \cos(I)$ factor. In order to identify the relative importance of each of these factors, figures 7.11 and 7.12 show again difference plots of $v_{n,\text{par},v}$ at day 80 and 0 UT, but this time calculated with a fixed neutral wind field and declination (figure 7.11) and a fixed neutral wind field only (figure 7.12). Any changes in $v_{n,\text{par},v}$ in figure 7.11 are therefore due to changes in the inclination, while they are due to changes in both inclination and declination in figure 7.12. This shows that changes in the inclination alone do not completely explain the global pattern in $\Delta v_{n,\text{par},v}$, while changes in the inclination and declination together capture most of it. Any remaining differences between figures 7.9 (for day 80, 0 UT) and 7.12 are due to changes in the wind itself.

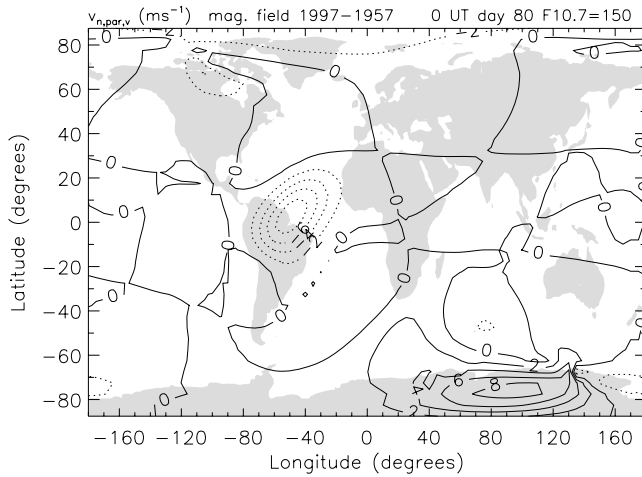


Figure 7.11. Difference in $v_{n,par,v}$ (ms^{-1}) at hmF2 height at day 80 and 0 UT for 1997-1957 due to changes in the magnetic field, but calculated by keeping the horizontal neutral wind and declination constant at the 1957 values.

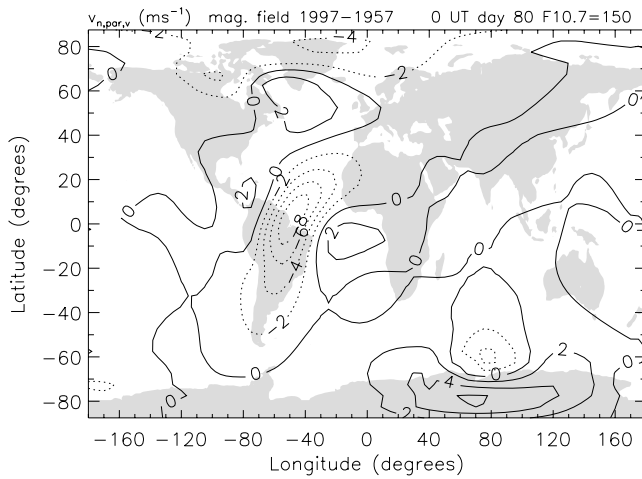


Figure 7.12. Difference in $v_{n,par,v}$ (ms^{-1}) at hmF2 height at day 80 and 0 UT for 1997-1957 due to changes in the magnetic field, but calculated by keeping the horizontal neutral wind constant at the 1957 values.

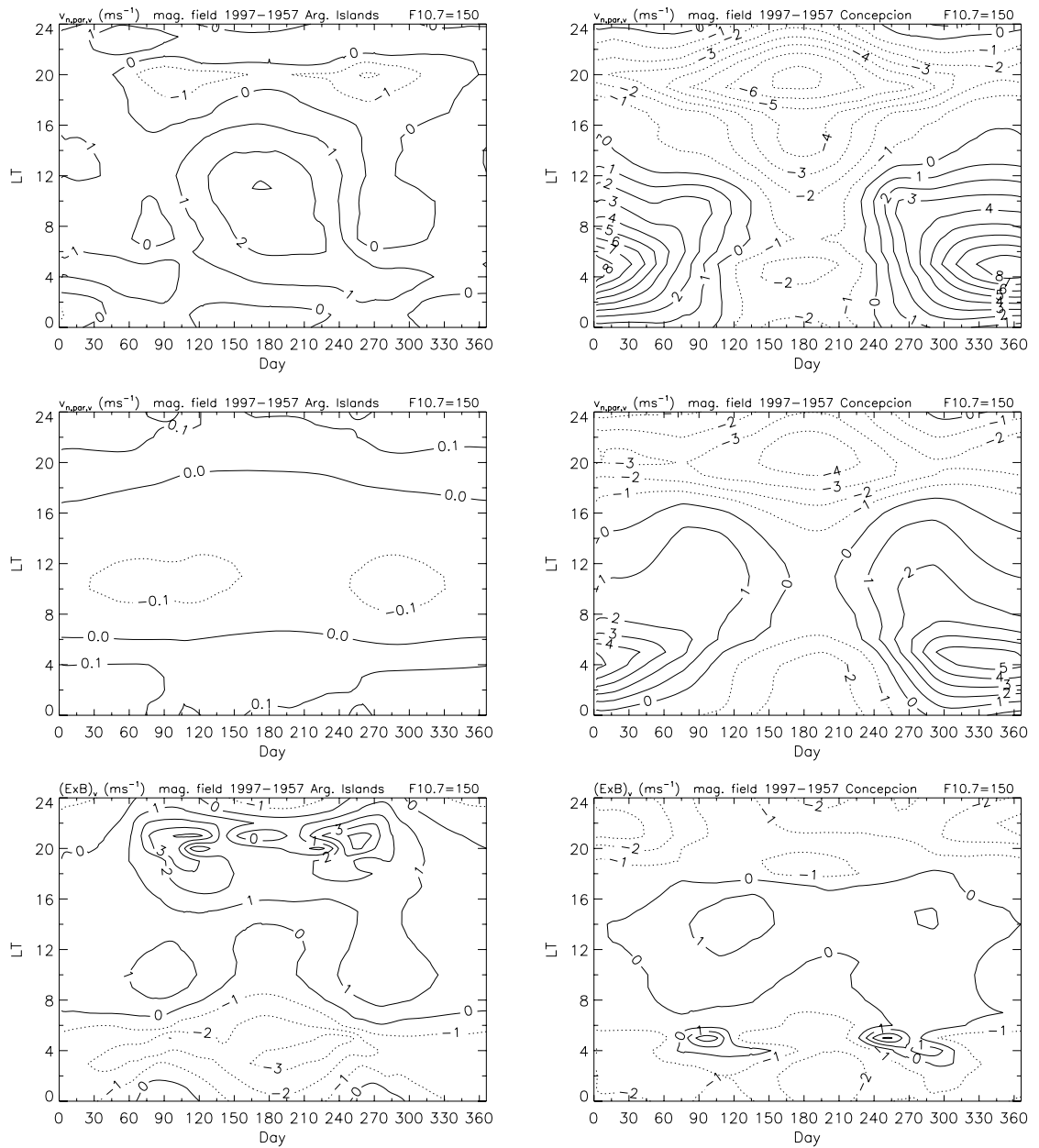


Figure 7.13. Seasonal and diurnal variation of the difference in $v_{n,par,v}$ (top), $v_{n,par,v}$ calculated with the constant wind field of 1957 (middle), and the vertical component of the \mathbf{ExB} drift $v_{E,v}$ (bottom) at hmF2 height for 1997-1957 at Argentine Islands (left) and Concepción (right) due to changes in the Earth's magnetic field. Note that the middle plot for Argentine Islands ($v_{n,par,v}$ with the constant wind field of 1957) has a contour interval of 0.1 ms^{-1} , while all other plots have a contour interval of 1 ms^{-1} .

Figure 7.13 shows the diurnal and seasonal variation in $\Delta v_{n,par,v}$ and $\Delta v_{E,v}$, as well as in $\Delta v_{n,par,v}$ calculated with the fixed neutral wind of 1957, for the two selected locations. At Concepción the seasonal/diurnal pattern in $\Delta v_{n,par,v}$ roughly

resembles the pattern in ΔhmF2 , indicating that it is also an important contributor to this variation, but it resembles the pattern in ΔfoF2 only vaguely. At Argentine Islands there is still less similarity between ΔhmF2 and ΔfoF2 on one hand and either $\Delta v_{n,\text{par},v}$ or $\Delta v_{E,v}$ on the other hand, suggesting that some of the changes in hmF2 and foF2 are caused by more complicated processes than just changes in $v_{n,\text{par},v}$ and $v_{E,v}$. The seasonal/diurnal variation in $\Delta v_{n,\text{par},v}$ is only in part caused by changes in the declination and inclination (for $\sim 50\text{-}80\%$ at Concepción and $<50\%$ at Argentine Island), with changes in the wind playing an important role as well, especially at Argentine Islands.

7.4.2 Implications for and comparison with other long-term trend studies

It is not surprising that changes in hmF2 and foF2 are most pronounced over the Atlantic Ocean and South America, as the largest changes in the magnetic field have occurred here, especially with respect to its direction. Unlike Jarvis et al. (1998), we show that contributions to long-term trends in hmF2 and foF2 from changes in the magnetic field can be substantial (up to ± 20 km and ± 0.5 MHz) and must be taken into account in this area. It is important to be aware of this when interpreting observations of long-term trends. When studying long-term trends in relation to changes in greenhouse gas concentrations only, it may be best to use observations from locations outside the area affected by magnetic field changes, though the results from the present study could in principle be used to correct for effects related to such changes to first order. The high seasonal and diurnal variation in ΔhmF2 and ΔfoF2 shows that it is essential to separate data with respect to local time and season before deriving long-term trends.

Jarvis et al. (1998) found that changes in the magnetic field could not produce a significant change in hmF2 at Argentine Islands. Though this station is at the edge of the area that is affected by changes in the magnetic field, we do find a significant effect on hmF2 here, especially at night in December and January. We suspect that the very small change found by Jarvis et al. (1998) must be related to the constant wind field they used in their calculations. We showed that in particular at Argentine Islands, changes in the wind v_n are largely responsible for the change in $\Delta v_{n,\text{par},v}$, which seems to be the most important contributor to the total change in hmF2 and foF2 in general. Specifically at Argentine Islands though, the seasonal/diurnal pattern in $\Delta v_{n,\text{par},v}$ does not match the modelled patterns in ΔhmF2 and ΔfoF2 so well, which may indicate that even more complex electrodynamic processes are responsible for these changes. In any case this means that it is important to solve for the interaction between

magnetic and electric fields and the neutral wind self-consistently, as we have done here, rather than using a fixed wind field.

The next question to address is whether the changes in hmF2 and foF2 we found could help explain observed long-term trends. Observed trends in hmF2 and foF2 are likely caused by the combined effects of changes in the magnetic field, changes in greenhouse gas and ozone concentrations, and possibly long-term changes in geomagnetic activity. Mikhailov (2006) argues that long-term changes in geomagnetic activity can explain most of the observed trends in foF2, but not those in hmF2, which is rather more affected by global cooling. However, we have seen in previous chapters that global cooling due to changes in CO₂ and ozone concentration as occurred from 1965 to 1995 can not fully explain trends in hmF2 either. Therefore we might expect that trends in hmF2 are mainly caused by changes in the magnetic field in those areas that are most affected, and that observed trends in these areas should compare relatively well with our modelled changes.

Observed trends in hmF2 and foF2 were given in table 3.4. Modelled changes for the same stations are given in table 7.2, all for day 80 at 12 local time. The order of magnitude of our largest values of hmF2 trends (in the South Atlantic, where we do not have ionospheric stations) is indeed similar to the order of magnitude of reported trends in hmF2, but observed trends at any particular station are often larger than our modelled ones. Observed trends in foF2 are almost an order of magnitude larger than modelled trends for some stations, while values are closer for others.

The strongest trends in hmF2 are observed at Concepción and Port Stanley, which are located in the area where magnetic field changes have been relatively large. However, the trend at Sodankylä is almost as strong, even though it is outside this area, and substantial trends are also observed at, for instance, Ahmedabad, Juliusruh and Poitiers that do not particularly stand out in our modelling results.

The strongest trends in foF2 by far are observed at Argentine Islands, followed by Ahmedabad and Concepción. Our modelling results show a stronger change at Concepción, with Argentine Islands showing large changes only at night from October to March, and even then not nearly as large as observed. At Ahmedabad we modelled only a very small change in foF2 as a consequence of changes in the magnetic field.

The overall pattern of modelled trends shows a marked change at a longitude of ~10-30°E, depending somewhat on season, UT, latitude and whether we consider hmF2 or foF2. Though the dividing line is mostly a bit more west than in the pattern found by Bremer (1998), this is still a remarkable similarity.

However, Bremer (1998) found mostly positive trends west of 30°E (in Europe), and negative trends in the east, while we model predominantly (weak) positive trends in western Europe, but find almost no change east of 30°. Also, we do not find an increase of foF2 trend magnitude with (geomagnetic) latitude, as Danilov and Mikhailov (1999) did, unless a specific latitude band would be selected.

When comparing the overall observed and modelled seasonal/diurnal patterns of $\Delta hmF2$ and $\Delta foF2$ where these are available, we find that the two do not match. For instance, the observed trend in foF2 at Argentine Islands (Elias and De Adler, 2006) shows a maximum around 6 LT and a minimum around 15 LT from March to September, while we find a maximum around 12 LT and a minimum at night for the same months. The observed trend in hmF2 at Concepción (Foppiano et al., 1999) is negative from 6 LT to midnight, with strong positive values around August from 0-4 LT, while we find positive values only from 4-12 LT in September-March and much more diurnal variation in negative trends than observed.

<i>Station name</i>	<i>Lat. (°)</i>	<i>Lon. (°)</i>	$\Delta hmF2$ (km)	$\Delta hmF2$ (km· decade ⁻¹)	$\Delta foF2$ (MHz)	$\Delta foF2$ (MHz· decade ⁻¹)
Churchill	58.8	-94.2	-0.20	-0.05	+0.17	+0.04
Ottawa	45.4	-75.9	-0.96	-0.24	+0.22	+0.06
Huancayo	-12.0	-75.3	-6.03	-1.51	+0.12	+0.03
Concepción	-36.8	-73.0	-5.41	-1.35	-0.37	-0.09
Port Stanley	-51.7	-57.8	-0.49	-0.12	-0.08	-0.02
Arg. Islands	-65.2	-64.3	+1.86	+0.47	+0.13	+0.03
Sodankylä	67.4	26.7	+0.92	+0.23	-0.02	-0.01
Lycksele	64.6	18.8	+0.87	+0.22	-0.02	-0.01
Yakutsk	62.0	129.6	+0.40	+0.10	0.00	0.00
Leningrad	60.0	30.7	+0.98	+0.25	-0.02	-0.01
Uppsala	59.8	17.6	+0.97	+0.24	-0.01	0.00
Tomsk	56.5	84.9	+0.05	+0.01	-0.02	-0.01
Sverdlovsk	56.4	58.6	+0.38	+0.10	-0.02	-0.01
Gorky	56.2	44.3	+0.85	+0.21	-0.03	-0.01
Moscow	55.5	37.3	+0.89	+0.22	0.00	0.00
Juliusruh	54.6	13.4	+1.29	+0.32	+0.04	+0.01
Irkutsk	52.5	104.0	-0.05	-0.01	-0.02	-0.01
Slough	51.5	-0.6	+0.20	+0.05	+0.09	+0.02
Dourbes	50.1	4.6	+0.20	+0.05	+0.11	+0.03
Poitiers	46.6	0.3	+0.20	+0.05	+0.19	+0.05
Wakkanai	45.4	141.7	+0.17	+0.04	+0.07	+0.02
Alma-Ata	43.3	76.9	-0.08	-0.02	-0.03	-0.01
Boulder	40.0	-105.3	-0.93	-0.23	+0.20	+0.05
Akita	39.7	140.1	-0.08	-0.02	+0.08	+0.02
Ashkhabad	37.9	58.3	-0.16	-0.04	-0.03	-0.01
Kokubunji	35.7	139.5	-0.10	-0.03	0.03	+0.01
Yamagawa	31.2	130.6	-1.05	-0.26	+0.04	+0.01
Okinawa	26.3	127.8	-1.48	-0.37	+0.02	+0.01
Ahmedabad	23.0	72.6	-1.65	-0.41	-0.08	-0.02
Maui	20.8	-156.5	+0.72	0.18	+0.12	+0.03

<i>Station name</i>	<i>Lat. (°)</i>	<i>Lon. (°)</i>	$\Delta hmF2$ (km)	$\Delta hmF2$ (km· decade ⁻¹)	$\Delta foF2$ (MHz)	$\Delta foF2$ (MHz· decade ⁻¹)
Townsville	-19.6	146.9	-1.38	-0.35	+0.04	+0.01
Johannesburg	-26.1	28.1	-3.87	-0.97	-0.27	-0.07
Mundaring	-32.0	116.2	-0.50	-0.13	-0.02	-0.01
Grahamstown	-33.3	26.5	-3.10	-0.78	-0.17	-0.04
Canberra	-35.3	149.0	-0.57	-0.14	-0.05	-0.01
Hobart	-42.9	147.3	-0.91	-0.23	-0.10	-0.03

Table 7.2. Overview of modelled trends in hmF2 and foF2 for 1997-1957 due to changes in the Earth's magnetic field for the grid point closest to each station that is listed (TIE-GCM uses a grid from -87.5° to +87.5° latitude and -180° to +180° longitude with a 5°x5° spacing), all at day 80 at 12 LT. The first six stations are in the American-Atlantic sector (-100 to -10 longitude) and are separately ordered by geographical latitude, as in table 3.4.

On the basis of the comparisons above, it seems that changes in the magnetic field can account for a substantial fraction of observed long-term trends in certain locations (e.g. ~30-50% at Concepción and ~20% at Argentine Islands), and can explain some of the regional variation, but certainly not all. The seasonal/diurnal variation in observed trends is not explained by changes in the magnetic field. This indicates that there are other important factors that have contributed to long-term trends in the ionosphere at these locations.

Modelling of trends due to changing greenhouse gas and/or ozone concentrations (e.g., Rishbeth and Roble, 1992; Akmaev and Fomichev, 2000; Akmaev et al., 2006) have not yet detailed the expected seasonal and local-time variations. Also here, in chapters 5 and 6, we have only considered two seasons, and all changes were for 0 UT (so different local times for different longitudes). In future studies it would be worthwhile to study seasonal and diurnal variations in trends due to changes in CO₂ and ozone concentration in more detail. Recent model simulations with TIE-GCM by Qian et al. (manuscript in preparation, 2008) are working towards this goal.

Further improvements to the present study could be made by accounting for possible changes in the high-latitude potential associated with changes in magnetic field strength, which is not possible with the TIE-GCM alone. However, we may be able to pursue this in the more distant future with a coupled ionosphere-magnetosphere model.

Finally, it may be possible that there is an interaction between global cooling effects and effects of changes in the magnetic field, since both affect the wind field. Though changes in wind are typically small, they clearly do affect the

height of the F2 layer. It would therefore be interesting to do simulations with the NCAR Thermosphere-Ionosphere-Mesosphere-Electrodynamics General Circulation Model (TIME-GCM; Roble and Ridley, 1994), an extension of TIE-GCM to include the mesosphere, with changes in composition only, changes in magnetic field only, and both changes at the same time. A study like this is currently being planned.

7.5 Summary and conclusions

Our modelling results show that decadal changes in the Earth's magnetic field are capable of causing substantial changes in hmF2 and foF2 in those regions where magnetic field changes have been relatively large. Changes in $v_{n,par,v}$ seem to be responsible for most of the global pattern in $\Delta hmF2$ and $\Delta foF2$, and relate mostly to changes in the $\sin(I) \cos(I)$ factor and the declination, though changes in the neutral wind also play a role. Changes in the vertical \mathbf{ExB} drift seem to be less important. Seasonal and diurnal patterns in $\Delta foF2$ and $\Delta hmF2$ are also partly explained by changes in $v_{n,par,v}$, but more complicated, yet unidentified processes likely play an important role in some locations as well.

Over South America and the Atlantic Ocean, changes in hmF2 and foF2 due to changes in the magnetic field are large enough to contribute significantly to long-term trends, and this should be taken into account when interpreting observations. A first comparison with observations for a few locations shows that changes in the magnetic field alone can explain some of the observed regional variation in trends, but not diurnal and seasonal variations. This may be due to additional effects of changes in greenhouse gas concentrations, or still other long-term changes in the atmosphere system. Possibly, changing effects of magnetosphere-ionosphere coupling due to changes in the strength of the magnetic field, which were not considered here, could also be important.

8. Solar and geomagnetic activity effects in long-term trend modelling

8.1 Introduction

In modelling studies, a certain solar and geomagnetic activity level usually needs to be prescribed. Since the atmosphere, and especially the thermosphere, responds strongly to changes in solar and geomagnetic activity, any perturbation to the system may be expected to cause a different response, depending on the levels that are chosen. However, it is not obvious which level is most appropriate for comparison with observations. Most observed trends are corrected for solar cycle influences, and sometimes also for geomagnetic activity fluctuations, and are therefore not representative of any level in particular. Also, the underlying assumption that solar and geomagnetic activity are independent parameters, unrelated to the long-term trend, is probably not entirely correct.

A few studies that considered trends for different solar and/or geomagnetic activity levels separately, found that observed trends in foF2 and thermospheric density depended on these activity levels (Poole and Poole, 2002; Alfonsi et al., 2008; Emmert et al., 2008). Rishbeth and Roble (1992) and Qian et al. (2006, 2008) showed that also modelled trends due to changes in CO₂ concentration were different for solar minimum and solar maximum.

Here we extend the modelling work mentioned above by performing not only simulations for solar minimum and maximum, but also for four intermediate solar activity levels, each with CO₂ and ozone concentrations representative of 1965 and 1995. This enables us to assess the role of the solar activity level on modelled trends in more detail, and for more parameters, than was done by the above studies. In addition, we consider the role of the geomagnetic activity level on modelled trends due to changes in CO₂ and ozone concentration, which has not been studied before. Finally, we also performed a second set of simulations with TIE-GCM at lower solar activity than that used in chapter 7, to briefly explore the role of the solar activity level in trends caused by changes in the Earth's magnetic field.

8.2 CMAT2 and TIE-GCM model settings

CMAT2 model simulations were carried out for day 80 and day 172, with the CO₂ and ozone concentration levels of 1965 and 1995. These were set up in the same way as in chapter 5, but each set, consisting of four runs (day 80 and 172, 1965 and 1995), was run with six different F10.7 values (80, 100, 125, 150,

175 and 200 sfu) and three different Kp index values (2+, 4o and 6-), resulting in a total of 6x3 sets, including the set of chapter 5.

Also two additional runs with TIME-GCM with the magnetic fields of 1957 and 1997, respectively, were carried out with F10.7 = 80 sfu. All other model settings were the same as in chapter 7. However, global results will now be shown for 12 local time (LT) rather than 0 and 12 UT, because observed trends are usually derived for a particular local time, and data coverage is best for noon hours.

8.3 Changes in CO₂ and ozone concentration

8.3.1 Temperature

Figure 8.1 shows the global mean response in temperature to changes in CO₂ and ozone concentration (1995-1965) for six different F10.7 values at the standard low geomagnetic activity of Kp = 2+. Both at day 80 and day 172 there is nearly no difference in the response throughout the middle atmosphere, but in the thermosphere there is.

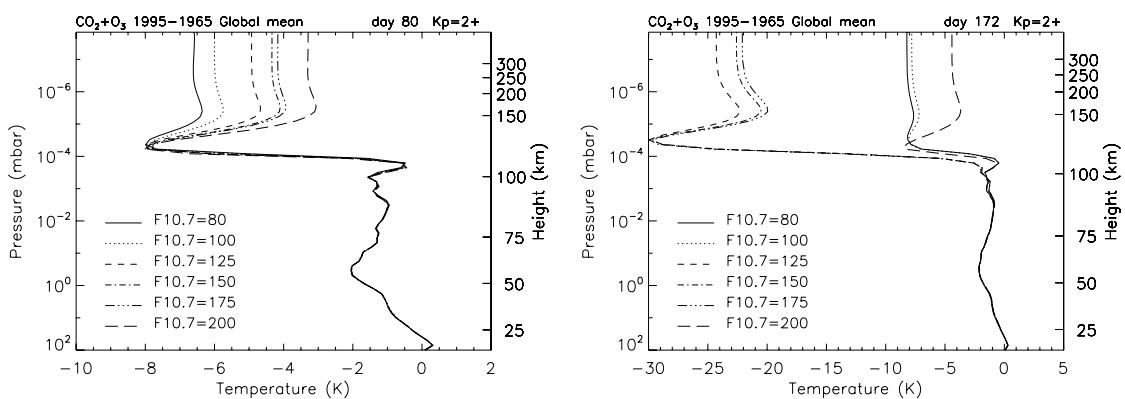


Figure 8.1. Difference in global mean temperature (K) for 1995-1965 at day 80 (left) and day 172 (right) due to changes in CO₂ and ozone concentration for six different F10.7 values in a constant pressure reference frame (Kp = 2+).

At day 80 the temperature response becomes smaller for increasing solar activity level, from -6.6 K at F10.7 = 80 sfu to -3.3 at F10.7 = 200 sfu for altitudes > 250 km. At day 172 the same behaviour might be seen for the very

low and highest F10.7 values, but intermediate F10.7 values from 125 to 175 sfu give a much stronger response, though within this group the response becomes again slightly weaker with increasing activity level. Also, at day 172 differences occur from somewhat lower altitudes onwards (~ 100 km) than at day 80 (~ 110 - 120 km).

The global mean temperature response for three different Kp values (at the standard low solar activity of F10.7 = 80 sfu) is shown in figure 8.2. Also in this case the only differences in response occur in the thermosphere, and these are much smaller than the differences in response between different solar activity levels, with a maximum difference of ~ 0.5 K at day 80 and ~ 0.7 K at day 172. For both days the response becomes slightly weaker for increasing geomagnetic activity level.

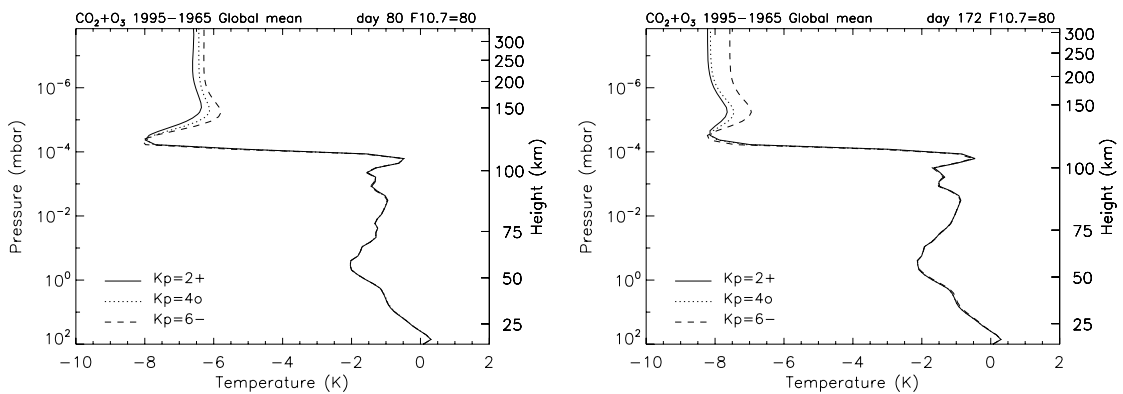


Figure 8.2. Difference in global mean temperature (K) for 1995-1965 at day 80 (left) and day 172 (right) due to changes in CO₂ and ozone concentration for three different Kp index values in a constant pressure reference frame (F10.7 = 80 sfu).

To study if the dependency of the thermospheric temperature response on the solar activity level depends in itself on the geomagnetic activity level, figure 8.3 shows the temperature response at a fixed pressure level in the thermosphere as a function of F10.7 for all three Kp values. At day 80 the behaviour is very similar for all three Kp levels, but at day 172, the response becomes stronger already at F10.7 = 100 sfu for Kp = 6-, instead of at F10.7 = 125 sfu. Also the differences in response between different Kp levels are larger (1-2 K) for F10.7 = 125-175 sfu.

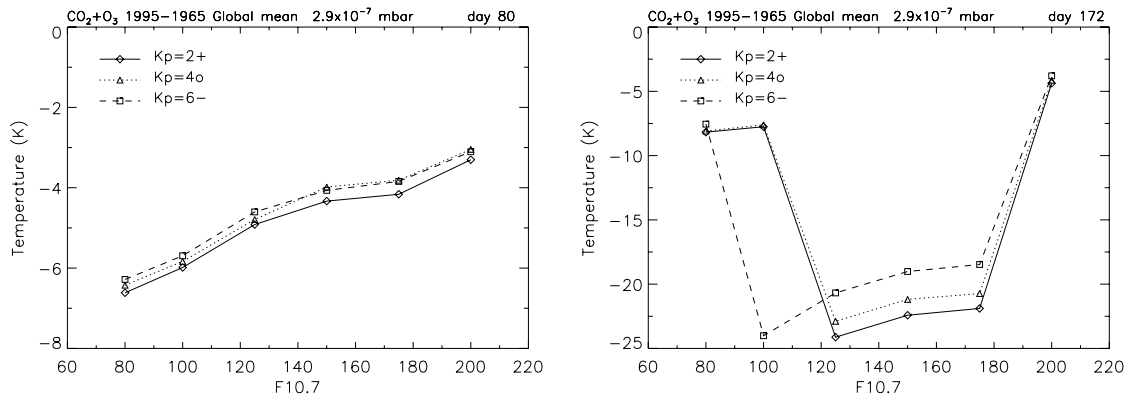


Figure 8.3. Difference in global mean temperature (K) in the thermosphere (at $2.9 \cdot 10^{-7}$ mbar) for 1995-1965 at day 80 (left) and day 172 (right) due to changes in CO_2 and ozone concentration as a function of F10.7 for three different Kp values.

8.3.2 Density

Figure 8.4 shows the response in global mean density for the six F10.7 values. At day 80 the results show little difference until ~ 100 km, and from 100 to 160 km the response oscillates around an average which decreases upwards from approximately 9% to 5-5.5% decrease in density. At higher altitudes different F10.7 levels lead to a different development of the response with height. For low solar activity levels the decrease in density remains approximately constant at 5-5.5% until ~ 200 km, and then somewhat increases with increasing height, while the response decreases with increasing height at higher solar activity levels.

At day 172 there is also little difference until ~ 100 km. For intermediate solar activity levels (F10.7 = 125-175 sfu), the response increases above 100 km until a maximum of -13% is reached at 130 km. It is then constant until ~ 210 km, above which it increases again further. For the lowest activity levels however, the response reaches a maximum of -10% at 100-110 km, and then decreases to -7% at 130 km. At higher altitudes the behaviour is similar as for the intermediate solar activity levels. For the highest activity level, the response is similar as for the lowest activity levels until 100-110 km, but above it monotonically decreases until -3% at 280 km.

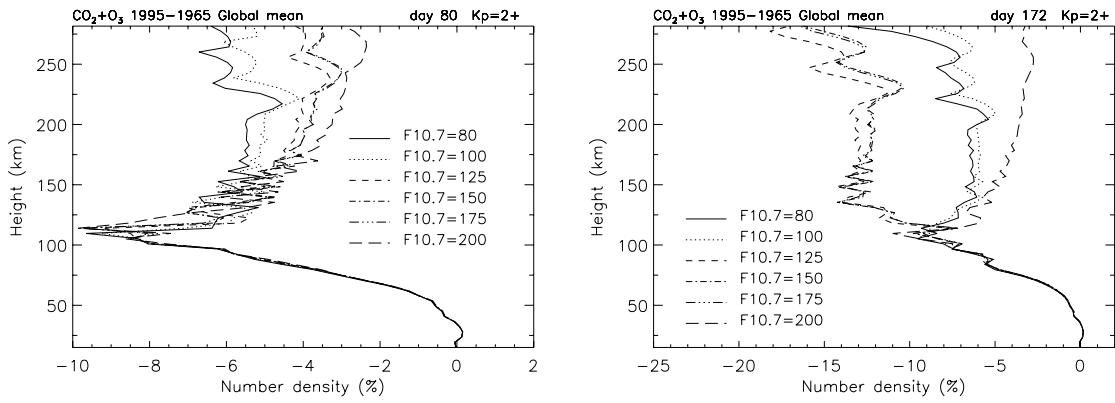


Figure 8.4. Difference in global mean density (%) for 1995-1965 at day 80 (left) and day 172 (right) due to changes in CO₂ and ozone concentration for six different F10.7 values in a constant height reference frame (Kp = 2+).

The response in density for three different Kp values, all at low solar activity (F10.7 = 80 sfu) is presented in figure 8.5. Again, until ~100 km there is no difference in the response, but at higher altitudes differences become larger, especially between Kp = 2+ and Kp = 4o on one hand and Kp = 6- on the other hand.

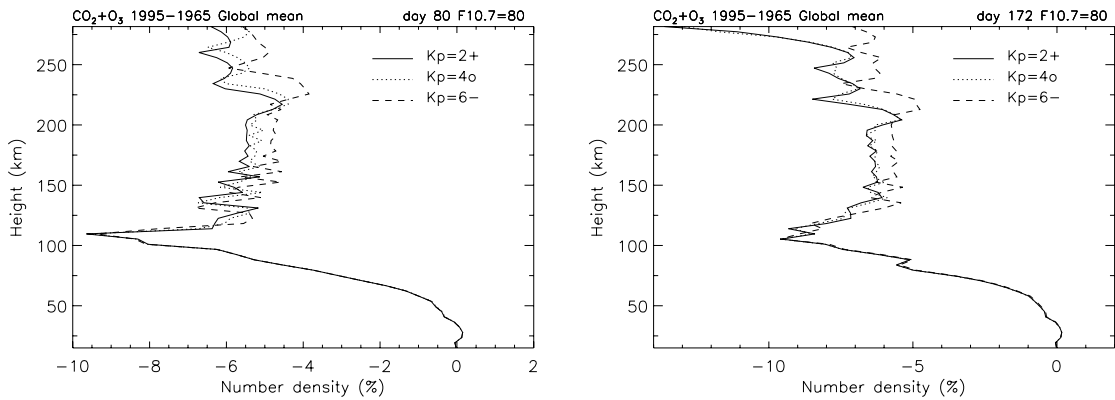


Figure 8.5. Difference in global mean density (%) for 1995-1965 at day 80 (left) and day 172 (right) due to changes in CO₂ and ozone concentration for three different Kp index values in a constant height reference frame (F10.7 = 80 sfu).

Figure 8.6 shows the behaviour of the density response as a function of F10.7 for the three Kp values at 200 and 300 km altitude. The general behaviour is similar to the thermospheric temperature response. Differences between

different Kp levels becomes larger for higher altitudes at day 80, but at day 172 this depends on the solar activity level. For instance, the difference in response between Kp = 2+ and Kp = 6- at F10.7 = 100 sfu is larger at 300 km than at 200 km, but at F10.7 = 125-175 sfu it is smaller at 300 km. This is probably due to the “waviness” of the density response profile (likely caused by a numerical instability), which makes the difference between Kp levels alternating between relatively small and relatively large.

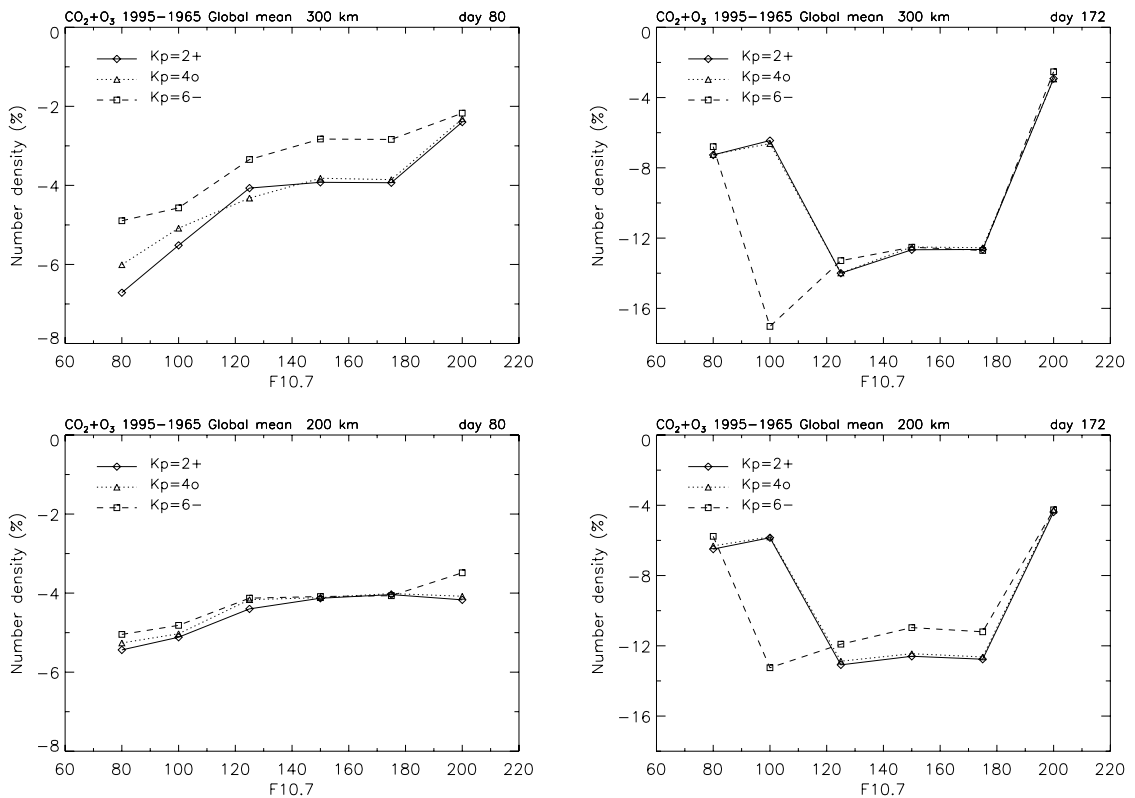


Figure 8.6. Difference in global mean density (%) for 1995-1965 at 200 km (bottom) and 300 km (top) at day 80 (left) and day 172 (right) due to changes in CO₂ and ozone concentration as a function of F10.7 for three different Kp values.

8.3.3 Ionospheric parameters

The difference in global mean hmF2 as a function of solar activity level for three Kp levels is shown in figure 8.7. The response in hmF2 is rather strongly dependent on the solar activity level that is used, and in different ways for different geomagnetic activity. Both factors together thus determine what response is obtained. Changes in hmF2 are generally larger at day 172 than at

day 80. For a few combinations of F10.7, Kp and day number, a positive response is found, even though cooling of the thermosphere is theoretically predicted to cause a lowering of the F2 layer under all circumstances.

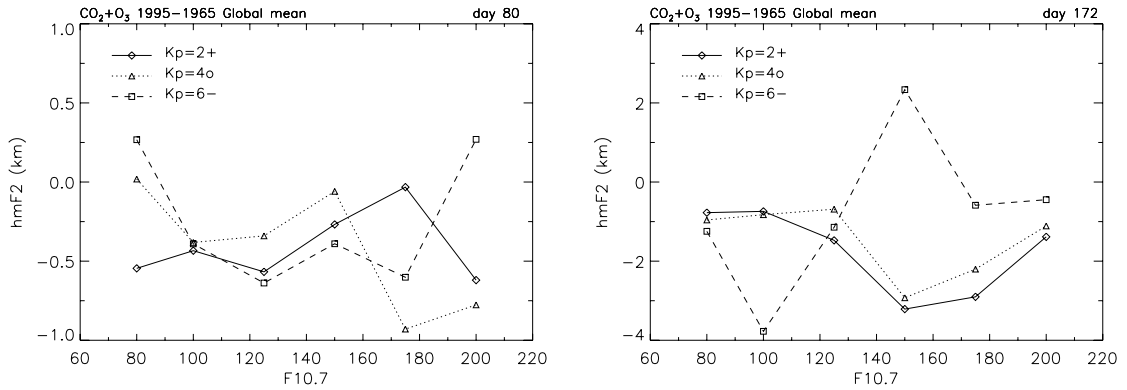


Figure 8.7. Difference in global mean hmF2 (km) for 1995-1965 at day 80 (left) and day 172 (right) due to changes in CO₂ and ozone concentration as a function of F10.7 for three different Kp levels.

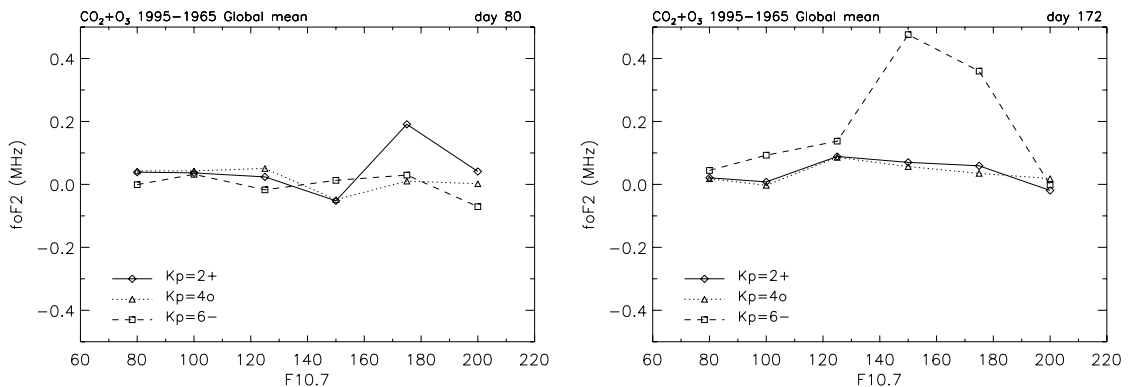


Figure 8.8. Difference in global mean foF2 (MHz) for 1995-1965 at day 80 (left) and day 172 (right) due to changes in CO₂ and ozone concentration as a function of F10.7 for three Kp levels.

Differences in foF2, shown in figure 8.8, depend relatively little on the solar and geomagnetic activity level, except for high solar activity levels at day 80 and the highest Kp level on day 172. While most responses in foF2 are very small, and probably not significant, they do become larger for a few specific conditions, such

as $F_{10.7} = 175$ sfu with $K_p = 2+$ at day 80, or $F_{10.7} = 150-175$ sfu with $K_p = 6-$ at day 172.

8.4 Changes in the Earth's magnetic field

8.4.1 Global maps of hmF2 and foF2

Figures 8.9 and 8.10 show the difference in hmF2 and foF2 due to changes in the Earth's magnetic field from 1957 and 1997 for $F_{10.7}$ levels of 80 sfu and 150 sfu at 12 LT. Over South America and the Atlantic Ocean, where effects are most pronounced, differences in hmF2 are up to $\sim 25\%$ larger at the higher solar activity level. Differences in foF2 are up to $\sim 30\%$ larger around the equator (from $\sim 20^\circ\text{N}$ to 20°S), but up to $\sim 35\%$ smaller around 40°S .

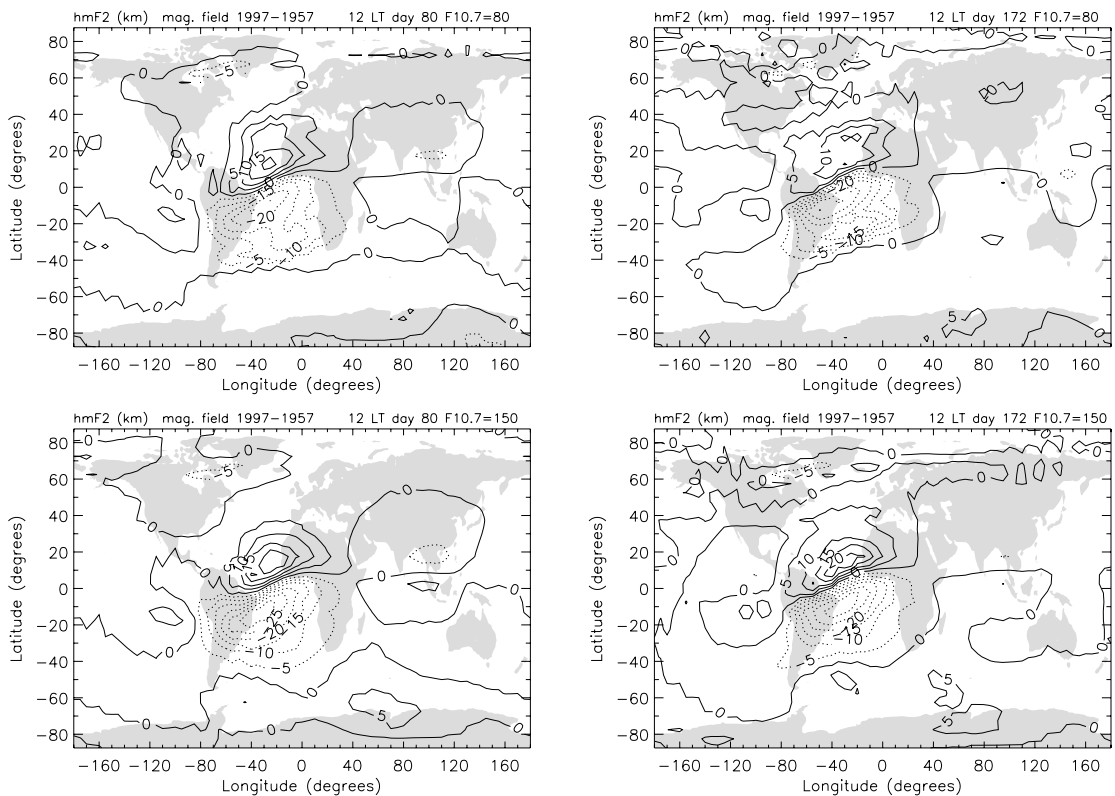


Figure 8.9. Difference in hmF2 (km) for 1997-1957 due to changes in the Earth's magnetic field for $F_{10.7} = 80$ sfu (top) and $F_{10.7} = 150$ sfu (bottom) at day 80 (left) and day 172 (right) at 12 LT.

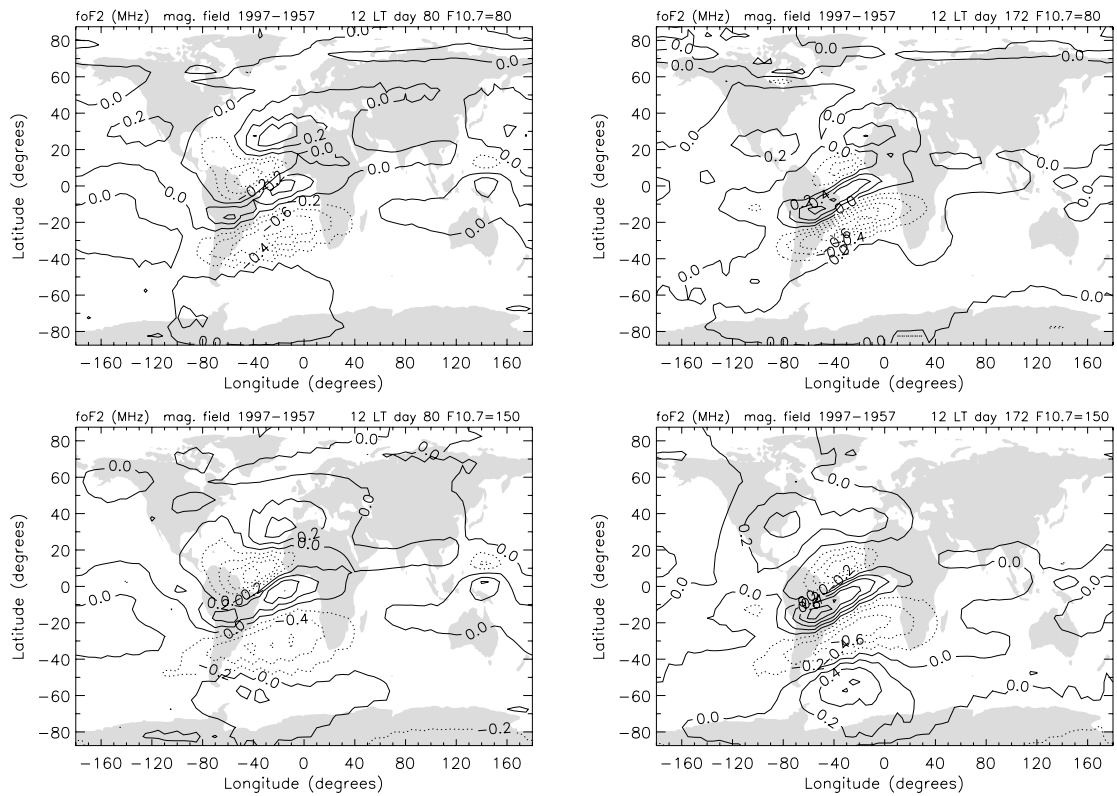


Figure 8.10. Difference in foF2 (MHz) for 1997-1957 due to changes in the Earth's magnetic field for F10.7 = 80 sfu (top) and F10.7 = 150 sfu (bottom) at day 80 (left) and day 172 (right) at 12 LT.

8.4.2 Seasonal and diurnal variation

Figure 8.11 and 8.12 show the seasonal and diurnal variation of the modelled trends in hmF2 and foF2, respectively, for Argentine Islands and Concepción for F10.7 = 80 sfu, to be compared with figures 7.7 and 7.8, which showed the same for F10.7 = 150 sfu. At most times, the trends are weaker for the lower solar activity, but there are some exceptions. For instance, the change in hmF2 at Argentine Islands in August at 19 LT or at Concepción in October at 12 LT is stronger for F10.7 = 80 sfu. Also, at Concepción the trend in hmF2 has a different sign for ~September-April for ~11-20 LT, depending on the solar activity level.

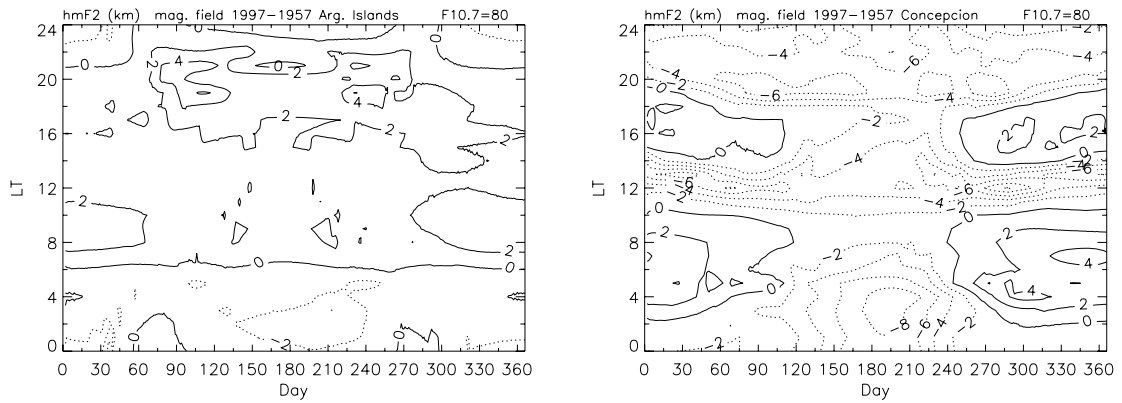


Figure 8.11. Seasonal and diurnal variation of the difference in hmF2 (km) for 1997-1957 at Argentine Islands (left) and Concepción (right) for F10.7 = 80 sfu due to changes in the Earth's magnetic field.

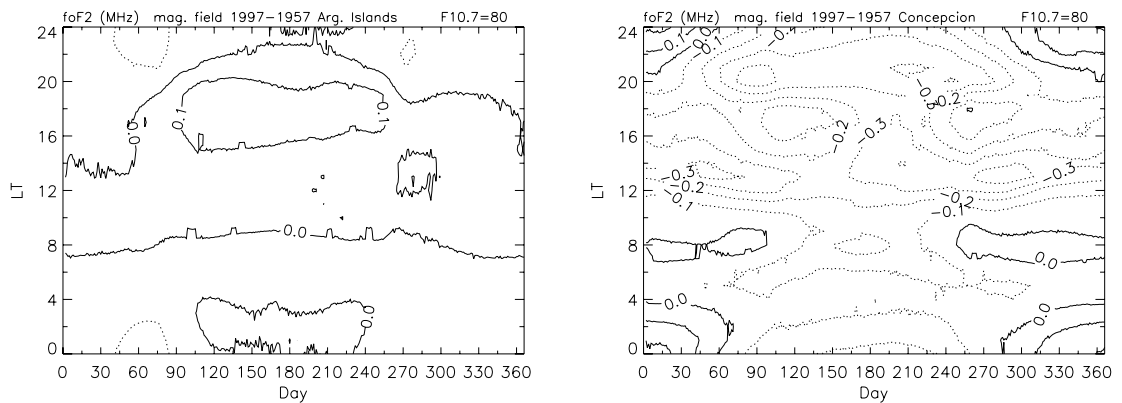


Figure 8.12. Seasonal and diurnal variation of the difference in foF2 (MHz) for 1997-1957 at Argentine Islands (left) and Concepción (right) for F10.7 = 80 sfu due to changes in the Earth's magnetic field.

8.5 Physical discussion of the obtained responses

8.5.1 Changes in CO₂ and ozone concentration

At day 80 we find that the responses in thermospheric temperature and density decrease with increasing solar activity level. This is in agreement with the modelling results of Qian et al. (2006), who found a smaller trend in thermospheric density for solar maximum conditions and a larger trend at solar minimum. They argued that the dependency of the trend on solar activity level is

due to CO₂ cooling being the dominant cooling process at solar minimum, while NO cooling becomes more important at solar maximum.

Figure 8.13 shows the ratio of the CO₂ cooling rate to the total cooling rate for low, intermediate and high solar activity. At day 80 we find indeed that CO₂ cooling is relatively more important in the lower thermosphere for lower solar activity. The mechanism suggested by Qian et al. (2006) can therefore explain our results for day 80.

For day 172 we found that responses in thermospheric temperature and density were much stronger for intermediate solar activity than for low and high activity. However, figure 8.13 shows that CO₂ cooling becomes again progressively more important for lower solar activity in the thermosphere for altitudes above 110-120 km, similar to day 80. At day 172 there is also a layer of slightly reduced importance of CO₂ cooling near 90 km though, where this pattern is reversed. Here CO₂ cooling is relatively more important for higher solar activity, and this could also affect the heat balance at higher altitudes. Therefore, the relative importance of CO₂ cooling on the temperature at altitudes of 110-130 km may be decided by its relative importance in situ as well as lower down, and perhaps this gives a higher net importance for CO₂ cooling at intermediate solar activity levels. This would explain the sharper increase in temperature response for F10.7 values of 125-175 sfu from ~110 km onward. However, we must bear in mind that this balance could be rather sensitive and possibly not represented as accurately as needed by CMAT2.

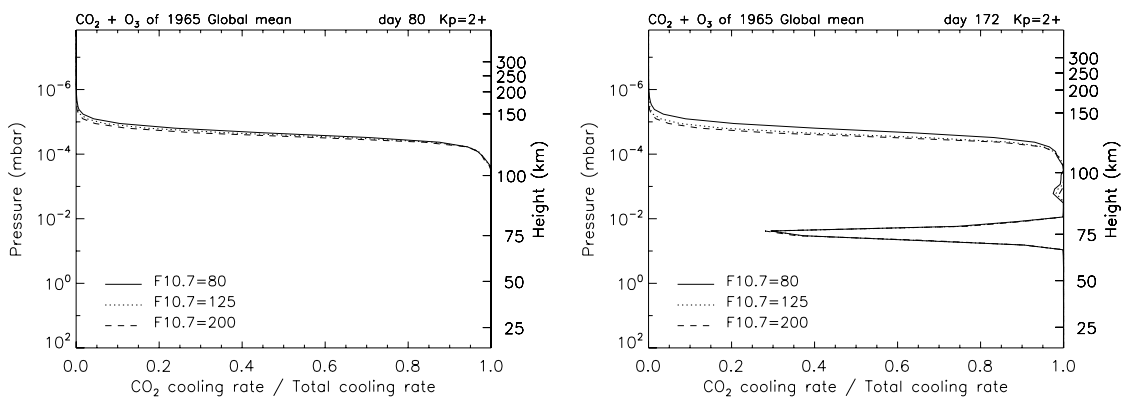


Figure 8.13. Ratio of the global mean CO₂ cooling rate to the total cooling rate at day 80 (left) and day 172 (right) for low (80 sfu), intermediate (125 sfu) and high (200 sfu) F10.7 values for CO₂ and ozone levels of 1965.

8.5.2 Changes in the Earth's magnetic field

In chapter 7 we found that the changes in hmF2 and foF2 were for a large part due to changes in $v_{n,par,v}$. Therefore, one might expect the dependency of these changes on solar activity level to be related to a dependency of changes in $v_{n,par,v}$ on the solar activity level. However, figure 7.14 shows that changes in $v_{n,par,v}$ show relatively little dependency on F10.7, especially in the area where the strongest changes in hmF2 and foF2 occur. Therefore this can explain at most a small part of the differences we saw in figures 8.9 and 8.10.

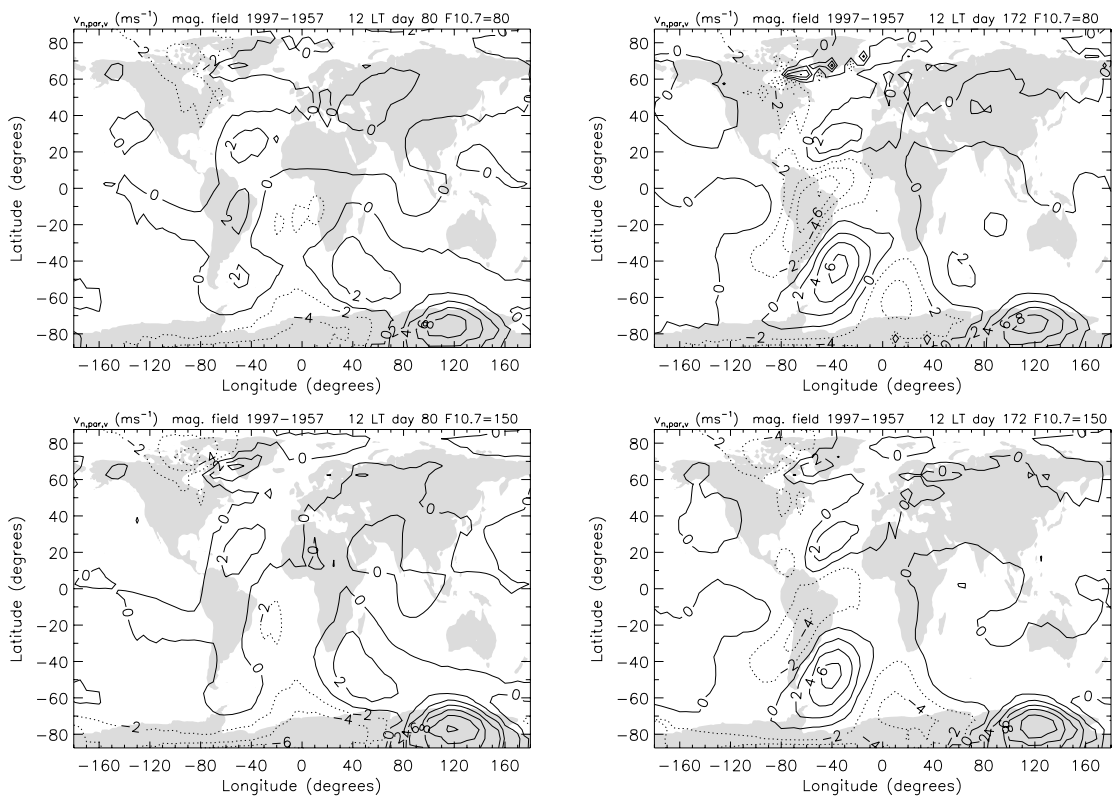


Figure 8.14. Difference in $v_{n,par,v}$ (ms^{-1}) for 1997-1957 due to changes in the Earth's magnetic field for F10.7 = 80 sfu (top) and F10.7 = 150 sfu (bottom) at day 80 (left) and day 172 (right) at 12 LT.

Another possible explanation for differences in the change in hmF2 for different solar activity levels could be a difference in scale height. Figure 8.15 shows the change in hmF2 divided by the local scale height, so that any differences related to this are removed. At day 80, relative changes in hmF2 are of similar magnitude around 20°S, but around 10°N they are stronger (by up to

~20%) for the lower solar activity. At day 172 relative differences are of similar magnitude around 10°N, but stronger (by up to ~25%) for the lower solar activity around 20°S. This means that differences in scale height are responsible for part of the difference in $\Delta hmF2$ for $F10.7 = 80$ sfu and $F10.7 = 150$ sfu. Where the differences now appear stronger for lower solar activity level, this must have been counteracted by another process to give the weaker response as seen in figure 8.9.

Differences in scale height should not be able to affect foF2, but perhaps the absolute magnitude of foF2 is important for the change that is obtained. Therefore figure 8.16 shows the difference in foF2 as a percentage. However, percentage changes in foF2 are smaller for the higher solar activity level, when foF2 is larger, indicating that changes in foF2 are not larger when foF2 itself is larger. Therefore we do not have an explanation yet for the differences in $\Delta foF2$ we saw in figure 8.10.

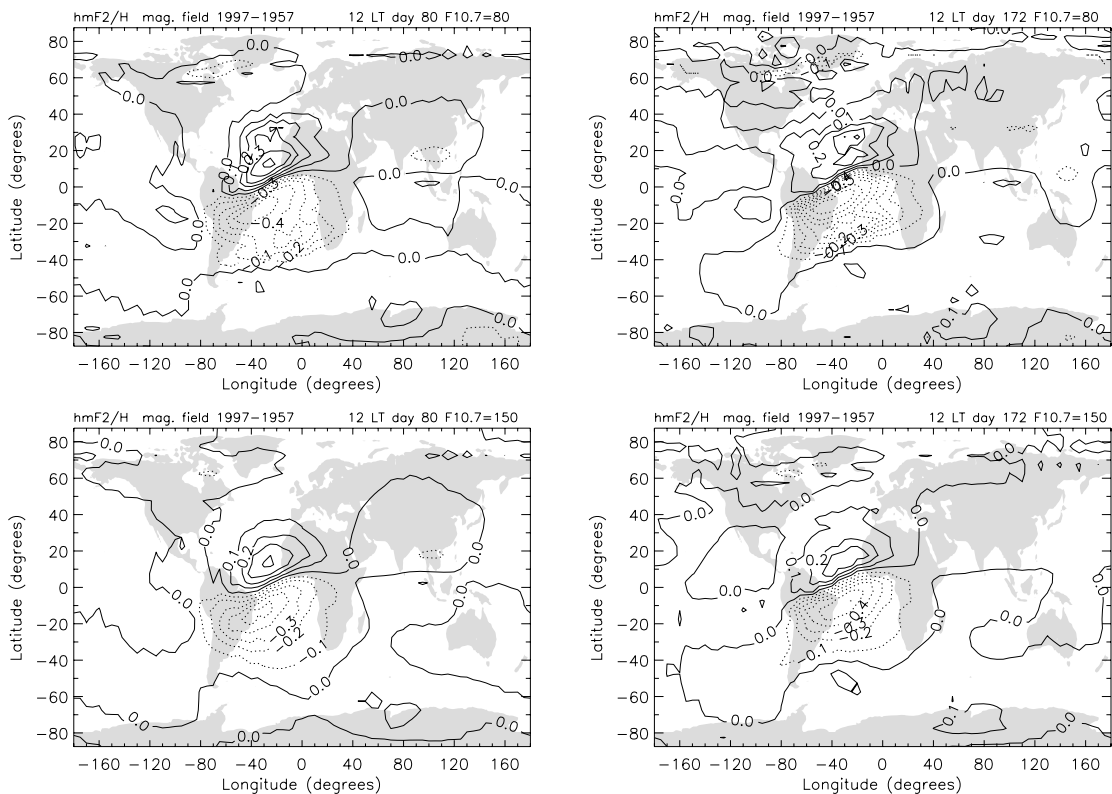


Figure 8.15. Difference in $hmF2/H$ for 1997-1957 due to changes in the Earth's magnetic field for $F10.7 = 80$ sfu (top) and $F10.7 = 150$ sfu (bottom) at day 80 (left) and day 172 (right) at 12 LT.

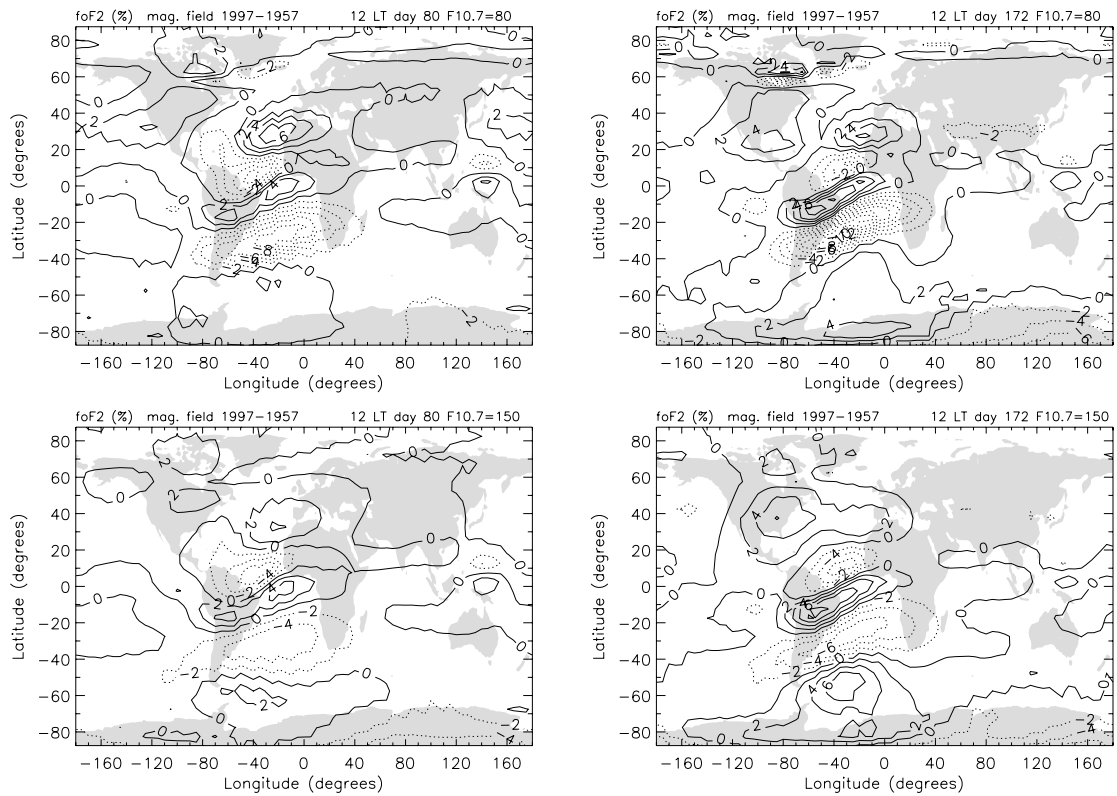


Figure 8.16. Difference in foF2 (%) for 1997-1957 due to changes in the Earth's magnetic field for F10.7 = 80 sfu (top) and F10.7 = 150 sfu (bottom) at day 80 (left) and day 172 (right) at 12 LT.

8.6 Comparison with observations

8.6.1 Thermospheric density

Emmert et al. (2004, 2008) studied annual mean trends in density between 200 and 700 km for different F10.7 bins, and found that they are larger for lower solar activity, though for F10.7 > 120 sfu any differences between F10.7 bins are within the error estimate and therefore not statistically significant. They further found that trends were largely independent from geomagnetic activity. These results are in qualitative agreement with our modelling results for day 80, though these are for a lower altitude than the results of Emmert et al. (2008). At day 172 however, we find a much stronger density response for intermediate solar activity levels, and in general our density trend magnitude at 300 km is larger than observed by Emmert et al. (2004, 2008).

8.6.2 Ionospheric parameters

Poole and Poole (2002) used a neural network technique to find trends in foF2 for Grahamstown (33°S, 26°E) for different solar and geomagnetic activity conditions. They found more strongly negative trends for high solar activity than for low solar activity, while there was little difference in trend between low and high geomagnetic activity.

We have found that the trend in foF2 for the location of Grahamstown due to changes in the magnetic field is indeed more strongly negative for higher solar activity, both for day 80 and day 172, and the order of magnitude of the trend they reported is in good agreement with our modelled trend as well. Changes in CO₂ and ozone concentration produced only a small trend in foF2 that did not show much variation with solar activity level. The trend in foF2 at Grahamstown, including its variation with solar activity level, may therefore be explained by changes in magnetic field only.

8.7 Conclusions

The thermospheric temperature and density responses to changes in CO₂ and ozone concentration depend on the solar activity level that is chosen. At day 80 the responses at F10.7 = 200 sfu are up to 50% smaller than those at F10.7 = 80 sfu, and at day 172 the maximum difference in response between different solar activity levels is even larger. Also the modelled responses in hmF2 and foF2 to changes in the Earth's magnetic field depend on the solar activity level that is described, with typical differences in responses between F10.7 = 80 sfu and F10.7 = 150 sfu of 25-35%. Differences in geomagnetic activity level have much smaller effects.

Comparisons with observed trends for different solar activity, where available, show overall agreement with modelling results (except results at day 172 for changes in CO₂ and ozone concentration), indicating that the dependency of the modelled responses on solar activity largely corresponds to the true behaviour of the atmosphere. This means that upper atmospheric responses to perturbations change continuously as solar activity changes, causing a non-linearity in the response that can not be filtered out by the method outlined in section 3.1.

It may therefore be better to derive trends separately for different solar activity levels, as a few studies have done. This will not only avoid non-linear effects of solar activity changes on obtained trends, but is also essential for a

better understanding of the dependency of trends on solar activity level, and makes comparisons between modelling results and data more straightforward.

In addition, since different mechanisms cause a different dependency of the resulting trend on solar activity, more information on the dependency that is observed may help differentiate between these mechanisms.

9. Summary, conclusions and further work

9.1 Summary

In chapter 3, an overview of observed long-term trends in temperature, density and winds in the middle and upper atmosphere, and in the ionospheric parameters hmF2 and foF2, was given. In general, the middle and upper atmosphere has cooled, and densities at fixed heights have decreased. Trends in winds vary with location and do not always stay constant, but do exhibit long-term change. Trends in hmF2 and foF2 show large differences with location, season and local time.

Observed trends have usually been attributed to increases in the CO₂ concentration, as has taken place since the industrial revolution. An increase in CO₂ concentration cools the middle and upper atmosphere through an increase in the emission of 15 μm radiation to space, and the resulting contraction of the atmosphere causes a decrease in density at fixed heights and a lowering of ionospheric layers. Though this is in qualitative agreement with observations, modelling studies predicted generally smaller trends than were observed. When also the decrease in ozone concentration was considered, modelling results agreed better with observed trends in temperature and density (Bremer and Berger, 2002; Akmaev et al., 2006).

The two studies mentioned above by Bremer and Berger (2002) and Akmaev et al. (2006) used models that extended up to 150-200 km. They could therefore not address any effects on the upper thermosphere or ionospheric F2 layer. In chapter 5 we used the CMAT2 model (described in chapter 4), which extends up to 300-600 km (depending on geophysical conditions), to study the effects of changes in CO₂ and ozone concentration also on the upper thermosphere-ionosphere system, and confirm the results of previous studies below 150-200 km. Both the effects of changes in CO₂ concentration only, and the combined effects of changes in CO₂ and ozone concentration, as took place from 1965 to 1995, were studied.

It was found that changes in ozone concentration increased the responses in temperature, density and winds by 10-70%, depending on the parameter studied, the day number and the region within the atmosphere, compared to responses to changes in CO₂ concentration only. These results were in reasonable agreement with previous modelling studies.

The additional effect of changes in ozone concentration on the ionospheric F2 layer was studied for the first time, and was found to consist of an extra lowering of hmF2 of 25% at day 80, but a 10% reduced lowering of hmF2 at day

172, while changes in foF2 were generally very small, and probably not significant. We do note that these results must be treated with some caution, as CMAT2 does not always extend to high enough altitudes to capture the night-time peak of the F2 layer, so that we had to ignore such points when calculating a global mean. In future studies, an updated version of CMAT2, including the GIP model, which covers altitudes up to 1000 km, should be used to study effects on the F2 layer more accurately.

The approach to modelling long-term trends used in chapter 5 (which is the standard approach used in long-term trend modelling studies), has some limitations in that only two simulations are used for comparison, set at particular geophysical conditions, and making use of a particular set of other model parameters and parameterizations. In chapter 6 some of those limitations were addressed by studying the sensitivity of the results obtained to the gravity wave parameterization that was used. Also, many more simulations were performed with each of the gravity wave parameterizations available to us within CMAT2 (Rayleigh friction, HLM, and MK95) to show the overall relation between the parameters studied (temperature, density, etc.) and the CO₂ concentration, and obtain more robust trend estimates that did not rely on just two simulations.

The overall [parameter]-CO₂ relations were found to be linear for some parameters, while non-linear for others, but all exhibited some kinks or steps in an otherwise fairly smooth function, in particular in the thermosphere. When only a small change in CO₂ concentration is considered, as is the 40 ppm change that was studied in chapter 5, the results obtained can be inaccurate due to these kinks. In chapter 6 a correction for their effects was made by fitting straight lines to the overall [parameter]-CO₂ relation to approximate the tangent of that relationship at 340 ppm (the centre of the interval studied in chapter 5). This led to improved, more robust trend estimates, which were mostly in better agreement with observed trends than those found in chapter 5 for changes in CO₂ concentration only. The improved trend estimates showed an underlying sensitivity to the gravity wave parameterization that was used, varying from 15-17% in case of the mesospheric and thermospheric temperature response to as much as 55% in case of hmF2 at day 80 and as little as 3-4% in case of the density response at 200 and 300 km at day 80.

In chapter 7 we focused on trends in the ionospheric F2 layer only, and tested the hypothesis whether these could be (partially) caused by changes in the Earth's magnetic field. The Earth's magnetic field varies slowly in strength and orientation over the course of centuries, and plays a role in the transport of ionospheric plasma, as charged particles will follow magnetic field lines as they are dragged along with horizontal neutral winds. This results in a vertical component

to their motion, which we called $v_{n,par,v}$ and is proportional to $\sin(I) \cos(I)$, and therefore changes when the inclination (I) of the magnetic field changes. Changes in declination may also cause changes in plasma transport, and changes in plasma transport itself will cause changes to the neutral wind through ion drag, which will consequently further modify the plasma transport, as was explained in more detail in section 7.1.

Previous studies that investigated the effects of changes in the magnetic field on the ionosphere considered the neutral winds to be fixed (Jarvis et al., 1998; Elias and De Adler, 2006), and could therefore not account for the electro-dynamical feedback mechanisms described above. The NCAR TIE-GCM, which we used in chapter 7, does account for these mechanisms. Model simulations with the IGRF of 1957 and 1997 showed substantial changes in both hmF2 and foF2 over South America and the Atlantic Ocean, which are the regions where changes in the magnetic field (in particular in inclination) have been largest. In other parts of the world changes in hmF2 and foF2 were found to be much smaller and mostly insignificant, compared to changes expected as a result of changes in CO₂ concentration (and possibly changes in ozone concentration as well). Changes in hmF2 and foF2 showed a strong dependency on day number and local time, resulting even in opposite signs for different times of year and/or day. Changes in $v_{n,par,v}$ were found to be an important cause of the changes in hmF2 and foF2 found.

In chapter 8 the role of the solar activity level in the modelling of long-term trends was examined. In chapters 5 and 6 a solar activity level of F10.7 = 80 sfu was prescribed, and in chapter 7 a level of F10.7 = 150 sfu. However, the middle and upper atmosphere depend strongly on solar activity level, and may therefore respond differently to perturbations (such as changes in CO₂ and ozone concentration or magnetic field), depending on the solar activity level, both when prescribed, as in modelling studies, and in reality.

In chapter 7 the CMAT2 simulations of chapter 4 were therefore repeated, considering combined changes in CO₂ and ozone concentration for a range of solar activity levels. It was found that responses decreased with increasing solar activity at day 80, with temperature and density changes at F10.7 = 200 sfu being up to 50% smaller than those at F10.7 = 80 sfu, while at day 172 responses were strongest for intermediate solar activity levels. This could be explained by changes in the relative importance of CO₂ cooling to the total cooling for different solar activity levels.

The influence of the geomagnetic activity level in modelling changes in CO₂ and ozone concentration was also examined, by repeating all model simulations for each solar activity level with two other Kp levels (4o and 6-) in addition to the

standard level of 2+. However, the effects of different geomagnetic activity on the responses were found to be relatively small compared to those of different solar activity.

The TIE-GCM simulations of chapter 7, with the magnetic fields of 1957 and 1997, were repeated with a lower solar activity level of $F_{10.7} = 80$ sfu. This caused responses in hmF2 and foF2 to change up to 25-35%, but they could be stronger or weaker for lower solar activity, depending on location. Differences for hmF2 were found to be partly related to differences in scale height for different solar activity, but an explanation for the differences in the response of foF2 was not found.

9.2 General conclusions and further work

In general, we can conclude that long-term trends are probably not caused by one process only, but rather a combination of processes, including changes in CO₂ concentration, ozone concentration, changes in the magnetic field, and possibly other long-term changes, for instance in solar and geomagnetic activity, which were not considered here. A full understanding of long-term trends may only be achieved by considering all these processes simultaneously, as they may interact and influence each other in unexpected ways. For instance, both changes in CO₂ and ozone concentration and changes in the magnetic field have been shown to cause changes in the neutral winds, which influence the changes modelled in other parameters. It is therefore possible that the effects of simultaneous changes in CO₂ and ozone concentration and magnetic field are not the same as the sum of the separate effects of changes in CO₂ and ozone concentration on one hand and changes in magnetic field on the other. A future study with TIME-GCM, in collaboration with R.G. Roble and A.D. Richmond, is planned to test this possibility.

Another general conclusion is that the middle and upper atmosphere respond differently to the same perturbation, depending on season, local time, solar and geomagnetic activity level, and possibly depending on other, yet unidentified geophysical parameters too. This is not only an important point for modelling studies, which usually need to prescribe a specific set of geophysical conditions, but should be considered more in observational studies as well. It is usually assumed, for instance, that solar cycle effects can be removed from long-term data sets by a linear (or sometimes quadratic) regression analysis as described in section 3.1. However, if the atmosphere indeed responds differently to a perturbation depending on solar activity level, this approach is not entirely

correct, and it would be better to study trends for different solar activity bins separately, as Emmert et al. (2004, 2008) have done. A study in collaboration with Th. Ulich is currently underway to do this for trends in hmF2 and foF2.

In addition to a sensitivity of the results obtained to the geophysical conditions that are prescribed, modelling studies suffer also from inaccuracies related to approximations and parameterizations, such as the gravity wave parameterization that is used. To minimize such inaccuracies, further work must continue to improve models and their parameterizations. With regards to gravity wave parameterizations specifically, more data is needed on the global distribution and characteristics of gravity waves to provide better constraints, on which currently progress is being made (e.g. Alexander et al., 2008).

Modelling studies are also necessarily incomplete because they must have boundaries, and boundary conditions can be important. For instance, in chapter 7 we could not address the effects of changes in magnetic field strength at high latitudes, in relation to changes in particle precipitation, because this would require knowledge about changes in magnetosphere-ionosphere coupling as a result of magnetic field changes. It is hard to say whether this is a serious omission or not, but it would certainly be worth examining in the future with a coupled magnetosphere-ionosphere model.

For long-term trend observations, it is important that measurements are continued into the future to form longer term data sets. This will make it easier to distinguish true long-term trends from cyclical behaviour, and is needed to determine how trends evolve on longer timescales. Also, a better spatial and temporal coverage of long-term data sets, as can now be established with satellites, is needed to assess which trends are regional features and which are global in extent, and how they vary with season and local time. All these efforts are required to gain a better understanding of the long-term behaviour of the atmosphere-ionosphere system.

References

- Akmaev, R.A., Fomichev, V.I., 2000. A model estimate of cooling in the mesosphere and lower thermosphere due to the CO₂ increase over the last 3-4 decades. *Geophys. Res. Lett.* 27 (14), 2113-2116.
- Akmaev, R.A., Fomichev, V.I., 1998. Cooling of the mesosphere and lower thermosphere due to doubling of CO₂. *Ann. Geophys.-Atmos. Hydrosph. Space Sci.* 16 (11), 1501-1512.
- Akmaev, R.A., Fomichev, V.I., Zhu, X., 2006. Impact of middle-atmospheric composition changes on greenhouse cooling in the upper atmosphere. *J. Atmos. Solar-Terr. Phys.* 68 (17), 1879-1889.
- Alexander, M.J., Gille, J., Cavanaugh, C., et al., 2008. Global estimates of gravity wave momentum flux from High Resolution Dynamics Limb Sounder observations. *J. Geophys. Res.* 113 (D15), D15S18.
- Alfonsi, L., De Franceschi, G., De Santis, A., 2008. Geomagnetic and ionospheric data analysis over Antarctica: a contribution to the long term trends investigation. *Ann. Geophys.* 26 (5), 1173-1179.
- Andrews, D.G., 2000. *An introduction to atmospheric physics.* Cambridge University Press. Cambridge.
- Baldwin, M.P., Dunkerton, T.J., 1999. Propagation of the Arctic Oscillation from the stratosphere to the troposphere. *J. Geophys. Res.* 104 (D24), 30937-30946.
- Banks, P.M., Kockarts, G., 1973. *Aeronomy.* Academic Press. New York, USA.
- Beig, G., Keckhut, P., Lowe, R.P., et al., 2003. Review of mesospheric temperature trends. *Rev. Geophys.* 41 (4), 1015.
- Berger, U., Dameris, M., 1993. Cooling of the upper atmosphere due to CO₂ increases - a model study. *Ann. Geophys.-Atmos. Hydrosph. Space Sci.* 11 (9), 809-819.
- Bilitza, D., 2001. International Reference Ionosphere 2000. *Radio Sci.* 36 (2), 261-275.
- Bojkov, R.D., Fioletov, V.E., 1995. Estimating the global ozone characteristics during the last 30 years. *J. Geophys. Res.* 100 (D8), 16537-16551.

- Bremer, J., 2001. Trends in the thermosphere derived from global ionosonde observations. *Adv. Space Res.* 28 (7), 997-1006.
- Bremer, J., 1998. Trends in the ionospheric E and F regions over Europe. *Ann. Geophys.* 16 (8), 986-996.
- Bremer, J., 1992. Ionospheric trends in midlatitudes as a possible indicator of the atmospheric greenhouse effect. *J. Atmos. Solar-Terr. Phys.* 54 (11-12), 1505-1511.
- Bremer, J., Berger, U., 2002. Mesospheric temperature trends derived from ground-based LF phase-height observations at mid-latitudes: comparison with model simulations. *J. Atmos. Solar-Terr. Phys.* 64 (7), 805-816.
- Bremer, J., Schminder, R., Greisiger, K.M., Hoffmann, P., Kürschner, D., Singer, W., 1997. Solar cycle dependence and long-term trends in the wind field of the mesosphere/lower thermosphere. *J. Atmos. Solar-Terr. Phys.* 59 (5), 497-509.
- Charney, J., Drazin, P., 1961. Propagation of planetary-scale disturbances from the lower into the upper atmosphere. *J. Geophys. Res.* 66 (1), 83-109.
- Chiu, Y.T., 1975. An improved phenomenological model of ionospheric density. *J. Atmos. Terr. Phys.* 37 (12), 1563-1570.
- Clilverd, M.A., Clark, T.D.G., Clarke, E., Rishbeth, H., 1998. Increased magnetic storm activity from 1868 to 1995. *J. Atmos. Solar-Terr. Phys.* 60 (10), 1047-1056.
- Clilverd, M.A., Ulich, T., Jarvis, M.J., 2003. Residual solar cycle influence on trends in ionospheric F2-layer peak height. *J. Geophys. Res.* 108 (A12), 1450.
- Cnossen, I., Richmond, A.D., 2008. Modelling the effects of changes in the Earth's magnetic field from 1957 to 1997 on the ionospheric hmF2 and foF2 parameters. *J. Atmos. Solar-Terr. Phys.* 70 (11-12), 1512-1524.
- Cnossen, I., Harris, M.J., Arnold, N.F., Yiğit, E. (2008). Modelled effect of changes in the CO₂ concentration on the middle and upper atmosphere: sensitivity to gravity wave parameterization. *J. Atmos. Solar-Terr. Phys.*, in press.
- Colegrove, F.D., Johnson, F.S., Hanson, W.B., 1966. Atmospheric composition in the lower thermosphere. *J. Geophys. Res.* 71, 2227-2236.
- Danilov, A.D., Mikhailov, A.V., 2001. F2-layer parameters long-term trends at the Argentine Islands and Port Stanley stations. *Ann. Geophys.* 19 (3), 341-349.

- Danilov, A.D., Mikhailov, A.V., 1999. Spatial and seasonal variations of the foF2 long-term trends. *Ann. Geophys.-Atmos. Hydrosph. Space Sci.* 17 (9), 1239-1243.
- Dickinson, R.E., Ridley, E.C., Roble, R.G., 1984. Thermospheric general circulation with coupled dynamics and composition. *J. Atmos. Sci.* 41 (2), 205-219.
- Dobbin, A.L., 2005. Modelling studies of possible coupling mechanisms between the upper and middle atmosphere. Dissertation/Thesis, University of London, London, UK.
- Dobbin, A.L., Aylward, A.D., Harris, M.J., 2006. Three-dimensional GCM modelling of nitric oxide in the lower thermosphere. *J. Geophys. Res.* 111, A07314.
- Dodd, J.A., Lockwood, R.B., Hwang, E.S., Miller, S.M., Lipson, S.J., 1999. Vibrational relaxation of NO($v=1$) by oxygen atoms. *J. Chem. Phys.* 111 (8), 3498-3507.
- Dungey, J.W., 1961. Interplanetary magnetic field and the auroral zones. *Phys. Rev. Lett.* 6 (2), 47-48.
- Elias, A.G., Ortiz de Adler, N., 2006. Earth magnetic field and geomagnetic activity effects on long-term trends in the F2 layer at mid-high latitudes. *J. Atmos. Solar-Terr. Phys.* 68 (17), 1871-1878.
- Emmert, J.T., Picone, J.M., Lean, J.L., Knowles, S.H., 2004. Global change in the thermosphere: compelling evidence of a secular decrease in density. *J. Geophys. Res.* 109 (A2), A02301.
- Emmert, J.T., Picone, J.M., Meier, R.R., 2008. Thermospheric global average density trends, 1967-2007, derived from orbits of 5000 near-Earth objects. *Geophys. Res. Lett.* 35 (5), L05101.
- England, S.L., Dobbin, A., Harris, M.J., Arnold, N.F., Aylward, A.D., 2006. A study into the effects of gravity wave activity on the diurnal tide and airglow emissions in the equatorial mesosphere and lower thermosphere using the Coupled Middle Atmosphere and Thermosphere (CMAT) general circulation model. *J. Atmos. Solar-Terr. Phys.* 68 (3-5), 293-308.
- Fels, S.B., Mahlman, J.D., Schwarzkopf, M.D., Sinclair, R.W., 1980. Stratospheric sensitivity to perturbations in ozone and carbon-dioxide - Radiative and dynamical response. *J. Atmos. Sci.* 37 (10), 2265-2297.

- Fomichev, V.I., Blanchet, J.P., 1995. Development of the new CCC/GCM longwave radiation model for extension into the middle atmosphere. *Atm.-Ocean* 33 (3), 513-529.
- Fomichev, V.I., Blanchet, J.P., Turner, D.S., 1998. Matrix parameterization of the 15 μm CO_2 band cooling in the middle and upper atmosphere for variable CO_2 concentration. *J. Geophys. Res.* 103 (D10), 11505-11528.
- Fomichev, V.I., Kutepov, A.A., Akmaev, R.A., Shved, G.M., 1993. Parameterization of the 15 μm CO_2 band cooling in the middle atmosphere (15–115 km). *J. Atmos. Terr. Phys.* 55 (1), 7-18.
- Foppiano, A.J., Cid, L., Jara, V., 1999. Ionospheric long-term trends for South American mid-latitudes. *J. Atmos. Solar-Terr. Phys.* 61 (9), 717-723.
- Forbes, J.M., 1996. Planetary waves in the thermosphere-ionosphere system. *J. Geomagn. Geoelectr.* 48 (1), 91-98.
- Fritts, D.C., 1984. Gravity wave saturation in the middle atmosphere: a review of theory and observations. *Rev. Geophys.* 22 (3), 275-308.
- Fritts, D.C., Alexander, M.J., 2003. Gravity wave dynamics and effects in the middle atmosphere. *Rev. Geophys.* 41 (1), 1003.
- Fuller, E.N., Schettler, P.D., Giddings, J.C., 1966. A new method for the prediction of gas phase diffusion coefficient. *Ind. Eng. Chem.* 58, 19.
- Fuller-Rowell, T.J., Rees, D., 1980. A 3-dimensional time-dependent global model of the thermosphere. *J. Atmos. Sci.* 37 (11), 2545-2567.
- Garcia, R.R., Solomon, S., 1985. The effect of breaking gravity waves on the dynamics and chemical composition of the mesosphere and lower thermosphere. *J. Geophys. Res.* 90 (D2), 3850-3868.
- Gavrilov, N.M., 1990. Parameterization of accelerations and heat flux divergences produced by internal gravity waves in the middle atmosphere. *J. Atmos. Terr. Phys.* 52 (9), 707-713.
- Givishvili, G.V., Leschenko, L.N., Shmeleva, O.P., Ivanidze, T.G., 1995. Climatic trends of the mid-latitude upper atmosphere and ionosphere. *J. Atmos. Terr. Phys.* 57 (8), 871-874.

- Hagan, M.E., Forbes, J.M., Vial, F., 1995. On modelling migrating solar tides. *Geophys. Res. Lett.* 22 (8), 893-896.
- Hargreaves, J.K., 1992. *The solar-terrestrial environment*. Cambridge University Press. Cambridge, Great Britain. 420 pp.
- Harris, M.J., 2001. *A new coupled middle atmosphere and thermosphere general circulation model: studies of dynamic, energetic and photochemical coupling in the middle and upper atmosphere*. Dissertation/Thesis, University College London, London, UK. 293 pp.
- Harris, M.J., Arnold, N.F., Aylward, A.D., 2002. A study into the effect of the diurnal tide on the structure of the background mesosphere and thermosphere using the new coupled middle atmosphere and thermosphere (CMAT) general circulation model. *Ann. Geophys.* 20 (2), 225-235.
- Hedin, A.E., 1991. Extension of the MSIS thermosphere model into the middle and lower atmosphere. *J. Geophys. Res.* 96 (A2), 1159-1172.
- Hedin, A.E., Fleming, E.L., Manson, A.H., et al., 1996. Empirical wind model for the upper, middle and lower atmosphere. *J. Atmos. Solar-Terr. Phys.* 58 (13), 1421-1447.
- Heelis, R.A., Lowell, J.K., Spiro, R.W., 1982. A model of the high-latitude ionospheric convection pattern. *J. Geophys. Res.* 87 (NA8), 6339-6345.
- Hines, C.O., 1997. Doppler-spread parameterization of gravity-wave momentum deposition in the middle atmosphere. Part 2: Broad and quasi monochromatic spectra, and implementation. *J. Atmos. Solar-Terr. Phys.* 59 (4), 387-400.
- Hines, C.O., 1991. The saturation of gravity waves in the middle atmosphere. Part II: development of Doppler-spread theory. *J. Atmos. Sci.* 48 (11), 1360-1379.
- Holt, J.M., Zhang, S.R., 2008. Long-term temperature trends in the ionosphere above Millstone Hill. *Geophys. Res. Lett.* 35 (5), L05813.
- Holton, J.R., 1983. The influence of gravity wave breaking on the general circulation of the middle atmosphere. *J. Atmos. Sci.* 40 (10), 2497-2507.
- Holton, J.R., 1982. The role of gravity wave induced drag and diffusion in the momentum budget of the mesosphere. *J. Atmos. Sci.* 39 (4), 791-799.

Jacobi, C., Gavrilov, N.M., Kürschner, D., Fröhlich, K., 2006. Gravity wave climatology and trends in the mesosphere/lower thermosphere region deduced from low-frequency drift measurements 1984–2003 (52.1°N, 13.2°E). *J. Atmos. Solar-Terr. Phys.* 68 (17), 1913-1923.

Jacobi, C., Lange, M., Kürschner, D., 2003. Influence of anthropogenic climate gas changes on the summer mesospheric/upper thermospheric meridional wind. *Meteorol. Z.* 12 (1), 86-92.

Jacobi, C., Portnyagin, Y.I., Merzlyakov, E.G., Solovjova, T.V., Makarov, N.A., Kürschner, D., 2005. A long-term comparison of mesopause region wind measurements over Eastern and Central Europe. *J. Atmos. Solar-Terr. Phys.* 67 (3), 229-240.

Jarvis, M.J., Jenkins, B., Rodgers, G.A., 1998. Southern hemisphere observations of a long-term decrease in F region altitude and thermospheric wind providing possible evidence for global thermospheric cooling. *J. Geophys. Res.* 103 (A9), 20774-20787.

Jonsson, A.I., de Grandpre, J., Fomichev, V.I., McConnell, J.C., Beagley, S.R., 2004. Doubled CO₂-induced cooling in the middle atmosphere: Photochemical analysis of the ozone radiative feedback. *J. Geophys. Res.* 109 (D24), D24103.

Kaufmann, M., Gusev, O.A., Grossmann, K.U., et al., 2002. The vertical and horizontal distribution of CO₂ densities in the upper mesosphere and lower thermosphere as measured by CRISTA. *J. Geophys. Res.* 107 (D23), 8182.

Keating, G.M., Tolson, R.H., Bradford, M.S., 2000. Evidence of long term global decline in the Earth's thermospheric densities apparently related to anthropogenic effects. *Geophys. Res. Lett.* 27 (10), 1523-1526.

Keeling, C.D., Whorf, T.P., 2005. Atmospheric CO₂ records from sites in the SIO air sampling network, in: *Trends: a compendium of data on global change*. Carbon Dioxide Information Analysis Center, Oak Ridge National Laboratory, U.S. Department of Energy, Oak Ridge, Tenn., U.S.A.

Keeling, R.F., Piper, S.C., Bollenbacher, A.F., Walker, J.S., 2008. Atmospheric CO₂ records from sites in the SIO air sampling network, in: *Trends: A Compendium of Data on Global Change*. Carbon Dioxide Information Analysis Center, Oak Ridge National Laboratory, U.S. Department of Energy. Oak Ridge, Tenn., U.S.A.

Kivelson, M.G., Russell, C.T., 1995. Introduction to space physics. Cambridge University Press. Cambridge.

Kostsov, V.S., Timofeyev, Y.M., 2003. Mesospheric carbon dioxide content as determined from the CRISTA-1 experimental data. *Izv. Atmos. Ocean. Phys.* 39 (3), 322-332.

Laštovička, J., 2005. On the role of solar and geomagnetic activity in long-term trends in the atmosphere-ionosphere system. *J. Atmos. Solar Terr. Phys.* 67 (1-2), 83-92.

Laštovička, J., Akmaev, R.A., Beig, G., Bremer, J., Emmert, J.T., 2006. Global change in the upper atmosphere. *Science* 314 (5803), 1253-1254.

Laštovička, J., Akmaev, R.A., Beig, G., et al., 2008. Emerging pattern of global change in the upper atmosphere and ionosphere. *Ann. Geophys.* 26 (5), 1255-1268.

Laštovička, J., Mikhailov, A.V., Ulich, T., et al., 2006. Long-term trends in foF2: A comparison of various methods. *J. Atmos. Solar-Terr. Phys.* 68 (17), 1854-1870.

Levin, E., Partridge, H., Stallcop, J.R., 1990. Collision integrals and high temperature transport properties for N-N, O-O and N-O. *J. Thermophys. Heat Transf.* 4, 469-477.

Li, D., Shine, K.P., 1995. A 4-dimensional ozone climatology for UGAMP models. UGAMP Internal Report no. 35.

Lindzen, R.S., 1981. Turbulence and stress owing to gravity wave and tidal breakdown. *J. Geophys. Res.* 86 (NC10), 9707-9714.

Lysenko, E.V., Perov, S.P., Semenov, A.I., et al., 1999. Long-term trends of the yearly mean temperature at heights from 25 to 110 km. *Izv. Akad. Nauk. Fiz. Atmos. Okean.* 35 (4), 435-443.

Marcos, F.A., Wise, J.O., Kendra, M.J., Grossbard, N.J., Bowman, B.R., 2005. Detection of a long-term decrease in thermospheric neutral density. *Geophys. Res. Lett.* 32 (4), L04103.

Marsh, D.R., Solomon, S.C., Reynolds, A.E., 2004. Empirical model of nitric oxide in the lower thermosphere. *J. Geophys. Res.* 109 (A7), A7301.

- Matsuno, T., 1982. A quasi one-dimensional model of the middle atmosphere circulation interacting with internal gravity waves. *J. Meteorol. Soc. Jpn.* 60 (1), 215-226.
- Maus, S., Macmillan, S., Chernova, T., et al., 2005. The 10th-Generation International Geomagnetic Reference Field. *Geophys. J. Int.* 161 (3), 561-565.
- McLandress, C., Shepherd, G.G., Solheim, B.H., Burrage, M.D., Hays, P.B., Skinner, W.R., 1996. Combined mesosphere/thermosphere winds using WINDII and HRDI data from the Upper Atmosphere Research Satellite. *J. Geophys. Res.* 101 (D6), 10441-10453.
- Medvedev, A.S., Klaassen, G.P., 2003. Thermal effects of saturating gravity waves in the atmosphere. *J. Geophys. Res.* 108 (D2), 4040.
- Medvedev, A.S., Klaassen, G.P., 2000. Parameterization of gravity wave momentum deposition based on nonlinear wave interactions: basic formulation and sensitivity tests. *J. Atmos. Solar-Terr. Phys.* 62 (11), 1015-1033.
- Medvedev, A.S., Klaassen, G.P., 1995. Vertical evolution of gravity wave spectra and the parameterization of associated wave drag. *J. Geophys. Res.* 100 (D12), 25841-25853.
- Medvedev, A.S., Klaassen, G.P., Boville, B.A., 1997. The parameterization of gravity wave drag based on the nonlinear diffusion of wave spectra, in: Hamilton, K. (Ed.), *Gravity wave processes: their parameterization in global climate models.* Springer. Berlin, Germany.
- Meyer, C.K., 1999. Gravity wave interactions with mesospheric planetary waves: A mechanism for penetration into the thermosphere-ionosphere system. *J. Geophys. Res.* 104 (A12), 28181-28196.
- Middleton, H.R., Mitchell, N.J., Muller, H.G., 2002. Mean winds of the mesosphere and lower thermosphere at 52 degrees N in the period 1988-2000. *Ann. Geophys.* 20 (1), 81-91.
- Mikhailov, A.V., 2006. Ionospheric long-term trends: can the geomagnetic control and greenhouse hypotheses be reconciled? *Ann. Geophys.* 24 (10), 2533-2541.
- Millward, G.H., Rishbeth, H., Fuller-Rowell, T.J., Aylward, A.D., Quegan, S., Moffett, R.J., 1996. Ionospheric F-2 layer seasonal and semiannual variations. *J. Geophys. Res.* 101 (A3), 5149-5156.

- Poole, A.V.W., Poole, M., 2002. Long-term trends in foF2 over Grahamstown using neural networks. *Annals Geophys.* 45 (1), 155-161.
- Portmann, R.W., 1994. The heat budget and global change in the mesosphere. Dissertation/Thesis, University of Colorado, Boulder, CO, USA. 187 pp.
- Portmann, R.W., Thomas, G.E., Solomon, S., Garcia, R.R., 1995. The importance of dynamical feedbacks on doubled CO₂-induced changes in the thermal structure of the mesosphere. *Geophys. Res. Lett.* 22 (13), 1733-1736.
- Portnyagin, Y.I., Merzlyakov, E.G., Solovjova, T.V., et al., 2006. Long-term trends and year-to-year variability of mid-latitude mesosphere/lower thermosphere winds. *J. Atmos. Solar-Terr. Phys.* 68 (17), 1890-1901.
- Prentice, I.C., Farquhar, G.D., Fasham, M.J.R., et al., 2001. The carbon cycle and atmospheric carbon dioxide, in: Houghton, J.T., Ding, Y., Griggs, D.J., et al., (Ed.), *Climate change 2001: the scientific basis. Contribution of working group I to the Third Assessment Report of the Intergovernmental Panel on Climate Change.* Cambridge University Press. New York, USA.
- Qian, L.Y., Roble, R.G., Solomon, S.C., Kane, T.J., 2006. Calculated and observed climate change in the thermosphere, and a prediction for solar cycle 24. *Geophys. Res. Lett.* 33 (23), L23705.
- Qian, L.Y., Solomon, S.C., Roble, R.G., Kane, T.J., 2008. Model simulations of global change in the ionosphere. *Geophys. Res. Lett.* 35 (7), L07811.
- Ramaswamy, V., Chanin, M.L., Angell, J., et al., 2001. Stratospheric temperature trends: Observations and model simulations. *Rev. Geophys.* 39 (1), 71-122.
- Richmond, A.D., Ridley, E.C., Roble, R.G., 1992. A thermosphere-ionosphere general circulation model with coupled electrodynamics. *Geophys. Res. Lett.* 19 (6), 601-604.
- Rind, D., Suozzo, R., Balachandran, N.K., Prather, M.J., 1990. Climate change and the middle atmosphere 1. The doubled CO₂ climate. *J. Atmos. Sci.* 47 (4), 475-494.
- Rishbeth, H., 1998. How the thermospheric circulation affects the ionospheric F2-layer. *J. Atmos. Solar-Terr. Phys.* 60 (14), 1385-1402.

- Rishbeth, H., 1990. A greenhouse effect in the ionosphere? *Plan. Space Sci.* 38 (7), 945-948.
- Rishbeth, H., Roble, R.G., 1992. Cooling of the upper atmosphere by enhanced greenhouse gases - modelling of thermospheric and ionospheric effects. *Planet. Space Sci.* 40 (7), 1011-1026.
- Roble, R.G., Dickinson, R.E., 1989. How will changes in carbon-dioxide and methane modify the mean structure of the mesosphere and thermosphere? *Geophys. Res. Lett.* 16 (12), 1441-1444.
- Roble, R.G., Ridley, E.C., 1994. A thermosphere-ionosphere-mesosphere-electrodynamics general circulation model (time-GCM): Equinox solar cycle minimum simulations (30-500 km). *Geophys. Res. Lett.* 26 (6), 417-420.
- Roble, R.G., Ridley, E.C., Richmond, A.D., Dickinson, R.E., 1988. A coupled thermosphere ionosphere general circulation model. *Geophys. Res. Lett.* 15 (12), 1325-1328.
- Rosenlof, K.H., Oltmans, S.J., Kley, D., et al., 2001. Stratospheric water vapor increases over the past half-century. *Geophys. Res. Lett.* 28 (7), 1195-1198.
- Semenov, A.I., 1996. Temperature regime of the lower thermosphere from emission measurements during the last decades. *Geomagn. Aeron.* 36 (5), 90-97.
- Sharma, S., Chandra, H., Vyas, G.D., 1999. Long term ionospheric trends over Ahmedabad. *Geophys. Res. Lett.* 26 (3), 433-436.
- Sharma, R.D., Roble, R.G., 2002. Cooling mechanisms of the planetary thermospheres: The key role of O atom vibrational excitation of CO₂ and NO. *ChemPhysChem* 3 (10), 841-843.
- Sharma, R.D., Wintersteiner, P.P., 1990. Role of carbon-dioxide in cooling planetary thermospheres. *Geophys. Res. Lett.* 17 (12), 2201-2204.
- Shved, G.M., Kutepov, A.A., Ogibalov, V.P., 1998. Non-local thermodynamic equilibrium in CO₂ in the middle atmosphere. I. Input data and populations of the v₃ mode manifold states. *J. Atmos. Solar-Terr. Phys.* 60 (3), 289-314.
- Solomon, S., 1999. Stratospheric ozone depletion: a review of concepts and history. *Rev. Geophys.* 37 (3), 275-316.

Solomon, S., Qin, D., Manning, M., et al., 2007. Climate Change 2007: The Physical Science Basis. Contribution of Working Group I to the Fourth Assessment Report of the Intergovernmental Panel on Climate Change. Cambridge University Press. New York, USA. 996 pp.

Sridharan, S., Tsuda, T., Gurubaran, S., 2007. Radar observations of long-term variability of mesosphere and lower thermosphere winds over Tirunelveli (8.7 degrees N, 77.8 degrees E). *J. Geophys. Res.* 112 (D23), D23105.

Thompson, D.W.J., Baldwin, M.P., Wallace, J.M., 2002. Stratospheric connection to Northern Hemisphere wintertime weather: Implications for prediction. *J. Climate* 15 (12), 1421-1428.

Tobiska, W.K., Woods, T., Eparvier, F., et al., 2000. The SOLAR2000 empirical solar irradiance model and forecast tool. *J. Atmos. Solar-Terr. Phys.* 62 (14), 1233-1250.

Ulich, T., Turunen, E., 1997. Evidence for long-term cooling of the upper atmosphere in ionosonde data. *Geophys. Res. Lett.* 24 (9), 1103-1106.

Upadhyay, H.O., Mahajan, K.K., 1998. Atmospheric greenhouse effect and ionospheric trends. *Geophys. Res. Lett.* 25 (17), 3375-3378.

Weinstock, J., 1990. Saturated and unsaturated spectra of gravity waves and scale-dependent diffusion. *J. Atmos. Sci.* 47 (18), 2211-2225.

Weinstock, J., 1982. Nonlinear theory of gravity waves: momentum deposition, generalized Rayleigh friction, and diffusion. *J. Atmos. Sci.* 39 (4), 1698-1710.

Xu, J., Liu, H.L., Yuan, W., et al., 2007. Mesopause structure from Thermosphere, Ionosphere, Mesosphere, Energetics, and Dynamics (TIMED)/Sounding of the Atmosphere Using Broadband Emission Radiometry (SABER) observations. *J. Geophys. Res.* 112 (D9), D09102.

Xu, Z.W., Wu, J., Igarashi, K., Kato, H., Wu, Z.S., 2004. Long-term ionospheric trends based on ground-based ionosonde observations at Kokubunji, Japan. *J. Geophys. Res.* 109 (A9), A09307.

Yue, X.N., Wan, W.X., Liu, L.B., Ning, B.Q., Zhao, B.Q., 2006. Applying artificial neural network to derive long-term foF2 trends in the Asia/Pacific sector from ionosonde observations. *J. Geophys. Res.* 111 (A10), A10303.